MULTI-SENSOR FUSION FOR NONDESTRUCTIVE INSPECTION OF FIBER REINFORCED COMPOSITE STRUCTURES

Thesis for the Degree of M. S.

MICHIGAN STATE UNIVERSITY

MARIE-PIERRE DUBUISSON

1991

DATE DUE	DATE DUE	DATE DUE

MULTI-SENSOR FUSION FOR NONDESTRUCTIVE INSPECTION OF FIBER REINFORCED COMPOSITE STRUCTURES

By

Marie-Pierre Dubuisson

A THESIS

Submitted to
Michigan State University
in partial fulfillment of the requirements
for the degree of

MASTER OF SCIENCE

Department of Computer Science

1991

ABSTRACT

MULTI-SENSOR FUSION FOR NONDESTRUCTIVE INSPECTION OF FIBER REINFORCED COMPOSITE STRUCTURES

By

Marie-Pierre Dubuisson

Composite materials have become increasingly important in the past decade due to their properties of high strength and light weight. Fiber reinforced composite materials are common not only in the aeronautic, military, and automobile industries, but also in the fabrication of increasing numbers of consumer products such as skis, furniture, and toys. For safety purposes as well as for quality control, nondestructive inspection (NDI) of composite structures is required. A variety of inspection techniques are available for detecting defects in composite materials. Only some of the possible defects can be detected by each NDI technique. Multi-sensor fusion techniques combine the results obtained from different NDI sensors to obtain a complete defect map of the observed specimen. In this thesis, three nondestructive inspection techniques have been used, namely X-radiography, ultrasonic C-scan, and acoustic emission. Algorithms to analyze the data obtained from each NDI sensor and to combine the information derived from them have been developed. These algorithms have been tested on several specimens with known inserted defects, and for each of them, an accurate defect map has been obtained.

To Bernard, Francine, Sophie and Séverine Dubuisson

Acknowledgements

I would like to express gratitude to my advisor, Professor Anil Jain, for all his help and advice. He increased my interest in pattern recognition and image processing and encouraged me to continue research in this area of computer science. I would like to thank Dr. Madhu Madhukar for teaching me the fundamentals of composite materials and NDI techniques. I also would like to thank Dr. Madhu Madhukar and Dr. Mihran Tuceryan for serving on my Master's thesis committee.

Thanks also go to all the members of the Pattern Recognition and Image Processing Laboratory for their interest and concern, and especially to Philippe Ballard, Sushil Bhattacharjee, Sally Howden, Greg Lee, Sateesha Nadabar, Tim Newman, Philippe Ohanian, Narayan Raja, Debby Trytten, and David Marks, our lab manager.

I wish to acknowledge Thomas Cooper from the MSU Clinical Center and Mike Thomas from the Veterinary Clinic for taking X-radiography images of the composite specimens; Nai Hsien Wang from the MSU Electrical Engineering Department for doing the C-scan imaging; and finally Michael Rich and Brian Rook from the Composite Material and Structure Center for helping me with the fabrication of composite materials and the use of the United Testing System device.

Financial support in the form of a graduate research assistantship from the Research Excellence Fund of the State of Michigan is gratefully acknowledged.

I am also very thankful to my parents and my two sisters for encouraging me to study in the United States. I also wish to thank all my friends for their moral support, and particularly Catherine Tamareille, Raquel and Evangelina Kuri, Mehdi Semati, and Davide Crippa.

Contents

List of Figures viii

List of Tables xi

1 Introduction 1

2 Composite Materials 4

2.1 Introduction 4

2.2 Composition and fabrication of composites 6

2.3 Defects in composite materials 7

2.4 Summary 8

3 Nondestructive Inspection of Composite Structures 11

3.1 Introduction 11

3.2 Acoustic emission technique 12

3.3 Ultrasonic technique 15

3.4 Radiographic technique 18

3.5 Penetrant technique 21

3.6 Thermographic technique 22

3.7 Holographic technique 23

3.8 Summary 24

4 Experimental Procedure 26

4.1 Introduction 26

4.2 Fabrication of the composite material specimens 26
4.3 The acoustic emission system 28
4.4 The X-radiography system 30
4.5 The ultrasonic C-scan system 30
4.6 Summary 31

5 Image Segmentation Techniques **33**
5.1 Introduction 33
5.2 Background 33
5.2.1 Analysis of the histogram of the image 34
5.2.2 Clustering 34
5.2.3 Edge detection 35
5.2.4 Region extraction 35
5.3 Study of three image segmentation techniques 36
5.3.1 Simple thresholding 36
5.3.2 Adaptive thresholding 39
5.3.3 Iterated Conditional Modes (ICM) 41
5.3.4 Results on test images 43
5.4 A new adaptive thresholding method 48
5.4.1 Yanowitz and Bruckstein's algorithm 48
5.4.2 Mask operators for edge detection 51
5.4.3 Canny edge detector 52
5.4.4 Results on test images 54
5.5 Segmentation algorithm for X-ray and C-scan images 55
5.6 Summary 62

6 Multi-Sensor Fusion **66**
6.1 Introduction 66
6.2 Background 67
6.3 Fusion algorithm 68
6.4 Results of the fusion algorithm 72

6.4.1 Specimen A 73
6.4.2 Specimen B 76
6.4.3 Specimen C 77
6.5 Summary 80

7 Experimental Results **81**
7.1 Introduction 81
7.2 General remarks 81
7.3 Specimen CHS 83
7.4 Specimen CS 85
7.5 Specimen CTHS 85
7.6 Specimen CTS 88
7.7 Specimen THS 88
7.8 Specimen TS 90
7.9 Summary 90

8 Conclusions **94**
8.1 Conclusions and discussion 94
8.2 Future research 96

A Curve fitting **98**
A.1 Introduction 98
A.2 Fitting data to a straight line 99
A.3 Nonlinear models 100
A.4 Levenberg-Marquardt method 101
A.5 Fitting a mixture of Gaussian densities to the image histogram 103

Bibliography **105**

List of Figures

2.1 Different methods for laying the fibers in a ply. 6
2.2 Example of a 3-layer composite structure. 6
2.3 Strength of the composite material is maximum along the direction of the fibers. 7
2.4 Examples of microscopic defects. 9

3.1 Typical display of an acoustic emission signal. 13
3.2 Location distribution histogram of events for a notched specimen at different load levels. 13
3.3 Cumulative number of events as a function of the number of cycles . 14
3.4 Acoustic emission for defect identification. 14
3.5 Reflection and transmission of the ultrasonic signal at a boundary. . . 15
3.6 Typical pulse-echo response from a planar reflector. 16
3.7 Angle-beam inspection of bolt holes. 16
3.8 C-scan inspection. 17
3.9 Angle-beam multiple probe array transducer. 18
3.10 Sequence of C-scan records showing fatigue induced delamination growth. 19
3.11 Layout of radiographic inspection. 19
3.12 Scanning set-up for computer-aided tomography. 20
3.13 Penetrant enhanced X-radiography of specimen. 21
3.14 Experimentation steps for penetrant inspection. 22
3.15 Thermal flow analysis 23
3.16 Line scanning thermographic technique. 24

3.17 Damage shown by interferograms. 25

4.1 Set of test specimens. 27
4.2 Set of non-test specimens. 28
4.3 Position of the sensors on the specimen. 29
4.4 Acoustic emission setup. 29
4.5 Example of an X-ray image. 30
4.6 Setup of the C-scan experiments. 31
4.7 Example of a C-scan image. 31

5.1 Histogram showing objects well-separated from the background. . . . 37
5.2 Threshold determination using mixture decomposition. 39
5.3 Interpolation of the threshold values. 41
5.4 Segmentation results using simple thresholding, adaptive thresholding and ICM on noisy images of type 1. 45
5.5 Segmentation results using simple thresholding, adaptive thresholding and ICM on noisy images of type 2. 46
5.6 Segmentation results using simple thresholding, adaptive thresholding and ICM on nonuniformly illuminated images. 47
5.7 Interpolation of a threshold surface in the Yanowitz and Bruckstein method. 49
5.8 Interpolation of the threshold surface in the case of C-scan or X-ray images. 51
5.9 Segmentation results using the algorithm proposed by Yanowitz and Bruckstein with different masks for edge detection on noisy images of type 1. 56
5.10 Segmentation results using the algorithm proposed by Yanowitz and Bruckstein with Canny edge detector on noisy images of type 1. . . . 57
5.11 Segmentation results using the algorithm proposed by Yanowitz and Bruckstein with different masks for edge detection on noisy images of type 2. 58

5.12 Segmentation results using the algorithm proposed by Yanowitz and Bruckstein with Canny edge detector on noisy images of type 2. . . . 59
5.13 Segmentation results using the algorithm proposed by Yanowitz and Bruckstein with different masks for edge detection on nonuniformly illuminated images. 60
5.14 Segmentation results using the algorithm proposed by Yanowitz and Bruckstein with Canny edge detector on nonuniformly illuminated images. 61
5.15 Segmentation of an X-ray image. 63
5.16 Segmentation of specimen A. 64
5.17 Segmentation of specimen B. 64
5.18 Segmentation of specimen C. 65

6.1 Defect map of specimen A. 74
6.2 Defect map of specimen B. 78
6.3 Defect map of specimen C. 79

7.1 Acoustic emission graph of specimen ND2. 82
7.2 Defect map of specimen CHS. 84
7.3 Defect map of specimen CS. 86
7.4 Defect map of specimen CTHS. 87
7.5 Defect map of specimen CTS. 89
7.6 Defect map of specimen THS. 91
7.7 Defect map of specimen TS. 92

List of Tables

2.1 The actual and anticipated growth of composite material usage in the U.S. overall and by industry. 5

2.2 Applications of composite materials. 5

3.1 Techniques for nondestructive evaluation of composite materials. . . 25

5.1 Definition of a pixel neighborhood for the ICM method. 43

6.1 Feature values for the connected components in the segmented X-ray image of specimen A. 73

6.2 Feature values for the connected components in the segmented C-scan image of specimen A. 73

7.1 Maximum load for the F specimens. 82

Chapter 1

Introduction

During the past decade, fiber reinforced composite materials have found increasing application in primary structural components. Composite materials are expected to enable significant advances to be made in space programs, military systems, commercial aircrafts, and ground transportation [Hul81]. The increasing use of these materials requires that reliable nondestructive inspection methods be available for the detection of defects and damage, or the assessment of quality of these materials. The detection of defects and damage in composite materials is particularly difficult because of the inhomogeneous, anisotropic, layered nature of the materials. In addition, the composites do not appear to degrade through the growth of a single dominant flaw, but rather by the growth of a damage zone that may be a combination of fiber, matrix, and interface failures [Rei80].

A variety of nondestructive inspection (NDI) test methods have been used for detecting both in-process defects (or "birth defects") and in-service damage. The most commonly used nondestructive inspection methods for composite materials are ultrasonic C-scan (to detect delamination voids and porosity), X-radiography (to detect delamination and broken fibers), liquid penetrant (to detect surface connected flaws), infrared techniques (to detect the thermal gradients caused by disbonds and porosity), neutron radiography (to detect bondline voids), and acoustic emission (to detect damage and determine its criticality) [Sen83].

While it is true that many NDI methods are available to detect defects and dam-

age, no single method is currrently capable of characterizing all possible flaws in composite materials. Very often, more than one NDI method is required to inspect a composite structure because different conditions or different types of defects and damage are revealed by different methods. Although some investigators have used several NDI methods to characterize the existing flaws in composite materials, the concept of multi-sensor fusion (as used in artificial intelligence or computer vision literature) has not been applied for detecting defects and damage in composite materials.

Multi-sensor fusion is an active area of research in computer vision [CY90]. One might want to fuse (or register) images of the same object or scene obtained by different sensors or by the same sensor at different times. For example, a mobile robot might be equipped with a camera and an array of ultrasonic sensors and one might want to construct a map of the environment using both pieces of information. The images might have been taken at different times. This is the case when one wants to register two images of the same scene obtained at different times from, say, a Landsat satellite. It is also possible that the multiple images have been acquired by the same type of sensor (e.g. CCD camera), but they are taken from different vantage points. This is typically the situation with binocular or trinocular stereo vision. The two most difficult problems in multi-sensor fusion are the registration or spatial alignment of multiple images, and the integration or fusion of the information extracted from the multiple images.

Our approach to multi-sensor fusion for NDI problems is the following: different NDI methods will be applied in order to locate the defects in composite specimens. The results obtained from individual NDI methods will be fused using computer vision techniques in order to get a defect map of the specimen.

The outline of this thesis is as follows. Chapters 2 and 3 will briefly describe the properties of composite materials, commonly encountered defects in composite materials, and the well known nondestructive inspection techniques for composite materials. Chapter 4 will report our experimental methodology and describe the specimens that have been fabricated along with the nondestructive inspection techniques that have been used. Chapter 5 will study image segmentation techniques

for the extraction of defects in X-ray and C-scan images. Chapter 6 will present the integration technique which has been used to obtain a defect map of the specimens from the information available from the different sensors. Chapter 7 will present the results for the specimens which have been fabricated. Finally, chapter 8 will give our conclusions and present some ideas for future research.

Chapter 2

Composite Materials

2.1 Introduction

Composite materials, the result of a relatively new technology for materials, are made of at least two different materials. A composite structure is stronger and lighter than the same structure made of regular metals. Composite materials have been used for almost two decades in the aerospace industry, but only recently have they been used in the recreational and automotive industries. The automobile industry is now taking advantage of the aerospace industry's discovery of materials lighter and stronger than steel. Even though the 1953 Chevrolet Corvette had the first all-composite car body, it cannot be considered as an everyday product. The major body parts of the 1990 Oldsmobile Silhouette van are completely constructed of glass-reinforced composite material. The Pontiac Trans Sport and the Chevrolet Lumina are built similarly from composite materials. As can be seen in Table 2.1 [Mil89], the recreation industry is actively incorporating composite materials in its products.

Composite materials can be classified into three major types:

- Natural composite materials such as wood, bone, bamboo, and muscles;
- Microcomposite materials like metallic alloys, and toughened or reinforced thermoplastics;

Table 2.1: The actual and anticipated growth of composite material usage in the U.S. overall and by industry. (In thousands of pounds).

Year	1977	1987	1992	2000
Composite materials	2,265	24,045	49,000	120,000
Aircraft/aerospace	1,079	16,879	34,900	85,500
Automotive	29	193	418	1,150
Other transportation	–	72	132	300
Sporting goods	1,003	4,617	9,000	21,000
Industrial and other products	154	2,284	4,550	12,050

Table 2.2: Applications of composite materials.

Industry	Examples
Aircraft	Wings, fuselage, landing gear, helicopter blades
Automobile	Body parts, lamp-housing, front-end panels, bumpers, leaf springs, seat housing, drive shafts
Boat	Hulls, decks, masts
Chemical	Pipes, tanks, pressure vessels
Furniture & equipment	Panels, housing, chairs, tables, ladders
Electrical	Panels, switchgear, insulators
Sport	Fishing rods, golf clubs, swimming pools, skis, canoes

- Macrocomposite materials, generally used in engineering products.

Only the last category will be studied here. Table 2.2 [Hul81] shows some examples of commercial products that are currently manufactured from composite materials.

Composite materials derive their strength from the combination of two or more materials which can be distinguished readily when examined under optical or electron microscopes. On the basis of strength and stiffness alone, fiber reinforced composite materials do not have a clear advantage over metals. The advantages of composite materials appear when the modulus per unit weight is considered. For the same strength, composite materials are much lighter than metals.

2.2 Composition and fabrication of composites

As mentioned before, composite materials consist of two or more physically distinct materials. They are usually made of two structures called the fibers and the matrix. Typical materials for the fibers are carbon, glass and polymers (carbon fibers being the most widely used). The matrix is usually either thermosetting resins (like epoxy and polyester) or thermoplastics (like polypropylene, nylon and polycarbonate).

The fibers are impregnated with resin to form a ply (or laminae). Figure 2.1 shows different methods for arranging the fibers to form the ply. Plies of the same kind are then stuck together tightly by the matrix to form layers. Different kinds of layers can then be assembled to form the composite material. Of course, a layer can be made from only one ply. Figure 2.2 shows an example of a composite material made from 3 layers.

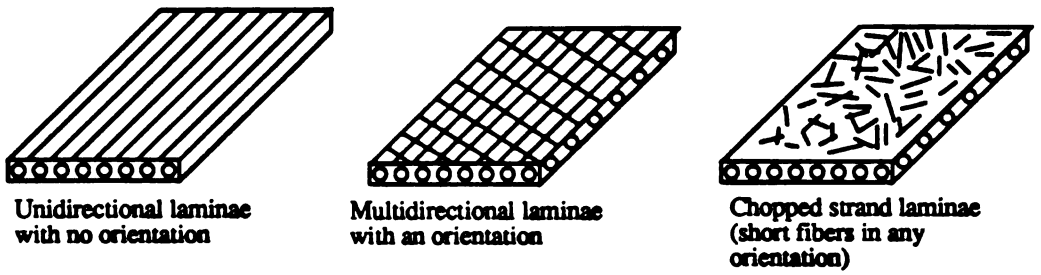

Figure 2.1: Different methods for laying the fibers in a ply.

The orientation of the fibers determines the direction in which the composite material will have the most strength. For example, the specimen of Figure 2.3 is

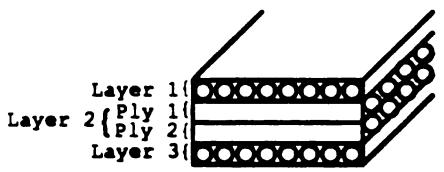

Figure 2.2: Example of a 3-layer composite structure.

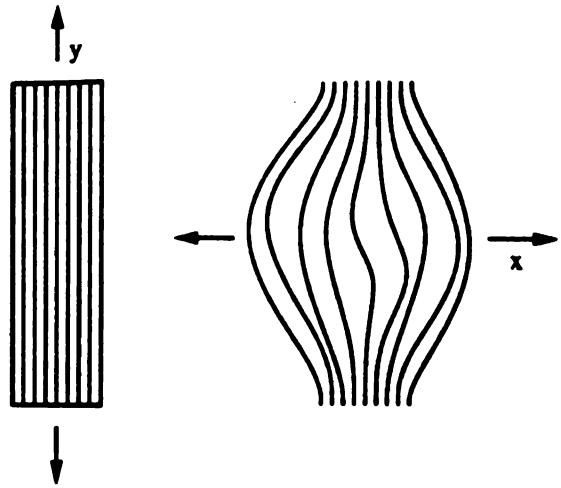

Figure 2.3: Strength of the composite material is maximum along the direction of the fibers.

stronger in the y-direction than in the x-direction.

The fabrication of composite materials is very simple when the layers are available and when the desired object or structure is a plate: one only has to lay the plies on top of one another and very carefully get rid of the air bubbles between the layers by pressing on each ply during the assembly process. The next step is to put the assembly in a vacuum bag and let it consolidate in an autoclave at the required pressure and curing temperature. For example, for a 10-ply specimen made of glass fibers and polyester, the required pressure is 85 psi (pounds per square inch) and the curing temperature is 260° F. The fabrication is more complicated when one wants to produce tubes, for example. Fibers, impregnated with resin, enter a mold continuously in the desired orientation. The whole assembly is heated until it becomes solid.

2.3 Defects in composite materials

The defects in a composite material may be located in the fibers, in the matrix, or in the fiber-to-matrix interface. They may occur during the fabrication process or

in-service. Different kinds of defects will be briefly described here and the nature of their origin will be explained.

Most of the microscopic defects occur during the fabrication process. Figure 2.4 [Pur83] shows examples of these defects. They are usually minor but can be the cause of more important defects if the material is subjected to excessive load. Composite materials can also have porosity inclusions, but the occurrence of this kind of defect can be minimized if one takes precautions to keep the fabrication process very clean.

Among the defects that occur in-service (i.e., during the use of the composite structure), we can find delaminations, debondings, fiber breaks and matrix cracking. Delamination occurs when two plies are separated by air. It often occurs when large stresses are generated in a direction normal to the plane of the plies, but it can also be due to a bad adhesion of two plies during the fabrication (this is why the plies are strongly pressed together). Debonding happens within one laminae when there is a void between a fiber and the matrix.

Some parts of the composite material are very sensitive to defects. Voids often occur at angle sections of the material due to inadequate consolidation in the mould. Notches in the material often produce defects like matrix cracks or delamination.

2.4 Summary

A growing number of industries have started to make use of composite materials for their products. As a result, composite materials are nowadays used for manufacturing a lot of different products (from car bodies to skis and chairs). The fabrication of composites requires a lot of precautions, since the introduction of a minor defect during the fabrication process can cause severe damage if the material is subjected to significant loads. Thus, some means of testing and inspecting composite structures

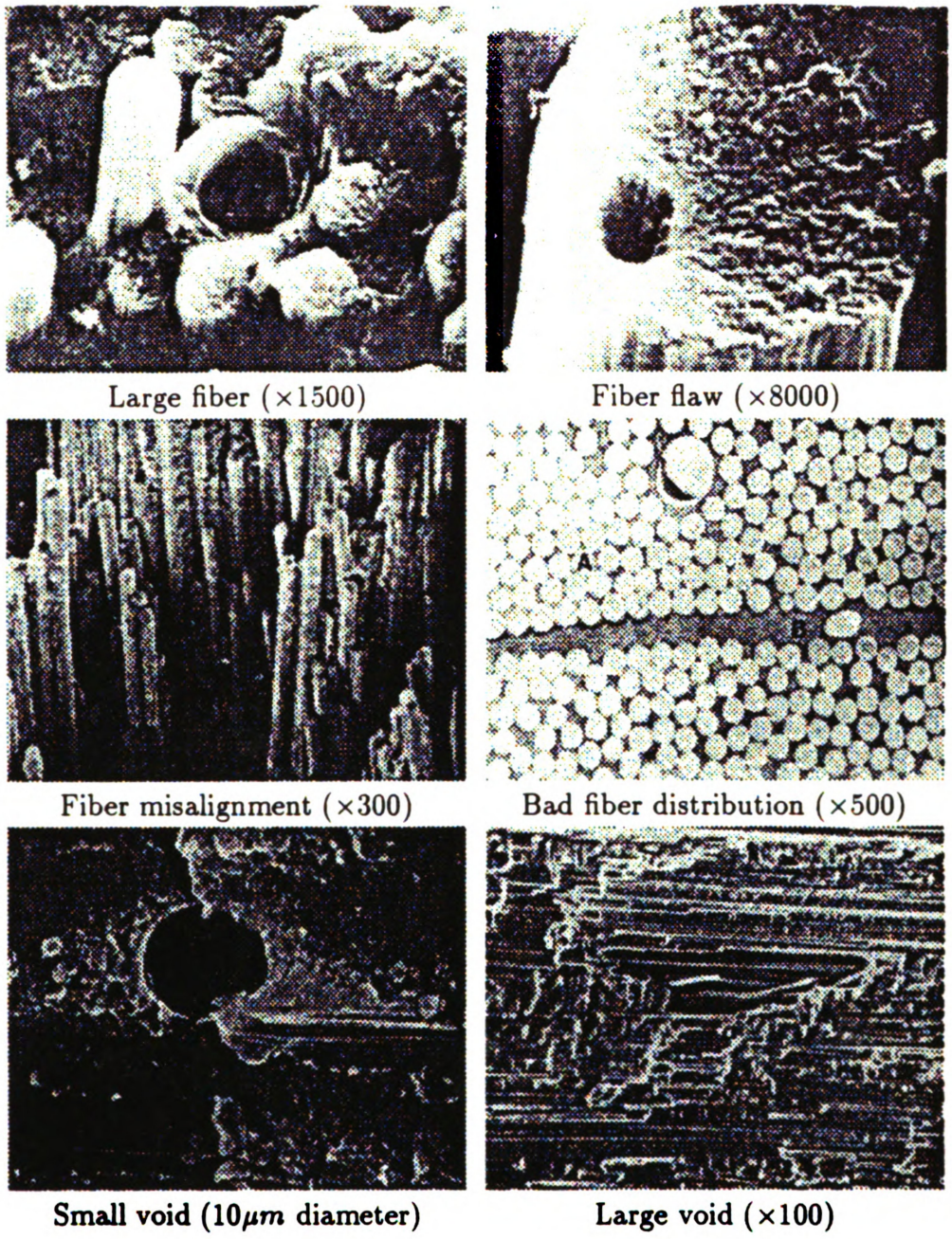

Figure 2.4: Examples of microscopic defects. (Reprinted from [Pur83])

is necessary in order to either detect critical damage or monitor minor defects that might be fatal to the entire structure. Nondestructive testing methods are being increasingly used for composite materials. The most commonly used nondestructive inspection techniques for composite materials will be presented in the next chapter.

Chapter 3

Nondestructive Inspection of Composite Structures

3.1 Introduction

With nondestructive inspection, one wants to avoid breaking the structure and still be able to inspect it for defects or damage before failure occurs. Nondestructive inspection is often applied when the structure to be tested is expensive, and failure catastrophic. For instance, one does not want to break an airplane wing to make sure that it does not have any defects. With the help of NDI, it is possible to test the wing just after fabrication and, regularly, during the use of the airplane.

There are two types of techniques used for nondestructive inspection:

- Active techniques: An electromagnetic wave, a magnetic field or a penetrant is applied to the structure and a certain kind of response is expected if a defect is present. Examples of these techniques are magnetic, ultrasonic, and radiographic techniques.

- Passive techniques: The structure is observed during either a typical load en-

vironment or a proof cycle and the presence of a defect is determined through some response of the specimen. Typical examples of this technique are acoustic emission, vibration analysis and visual examination.

Commonly used NDI techniques for composite materials will be discussed in the following sections.

3.2 Acoustic emission technique

In recent years, emphasis has been placed on the potential of the acoustic emission technique as an easy nondestructive tool to detect damage initiation and accumulation in real time. The principle of the acoustic emission technique is as follows. Two sensors are placed at the extremities of the specimen, while it is subjected either to fatigue loading or loading-unloading cycles. The maximum load depends on the material, but is generally around 10 to 20 kN (kiloNewton). The frequency range of the emitted signals is below 20 kHz. Figure 3.1 shows a typical signal (called event) which is a damped sine wave. We can measure the amplitude, the number of counts, and the duration of the event. After having recorded these parameters of the events, we can display different graphs such as the location distribution histogram of events, which counts the number of events received from a particular location in the specimen, or the amplitude distribution histogram of events, which counts the number of events which had a certain amplitude. The whole specimen emits signals which can be seen on an oscilloscope, but the defects or cracks emit more events than the rest of the specimen, so that they can be detected.

Figure 3.2 [AGM85] shows the number of events as a function of the location in the specimen. Each one of the five graphs shows the results at different load levels. It can be easily seen in the lower graph, which shows the number of events at a

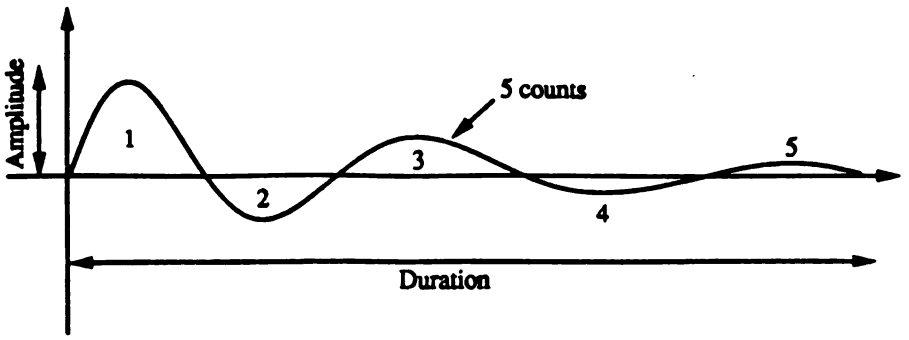

Figure 3.1: Typical display of an acoustic emission signal.

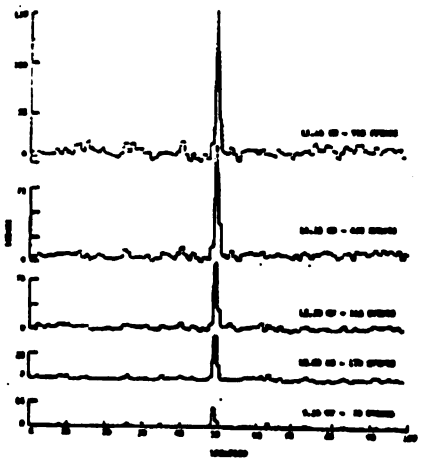

Figure 3.2: Location distribution histogram of events for a notched specimen at different load levels. (Reprinted from [AGM85])

small load level, that the specimen emits more events at a crack location but that at a critical load level, in the upper graph, emission occurs throughout the specimen because of fatigue.

When one wants to monitor damage accumulation, the specimen has to be subjected to loading-unloading cycles, and different parameters of the signal are measured and analyzed. As an example, Figure 3.3(a) [AMG84] shows the cumulative number of events as a function of the number of cycles for an unnotched specimen, while Figure 3.3(b) shows an increase in the number of events at the corresponding cycle number where the damage occurs. Most of the damage occurs because of the notch in the specimen.

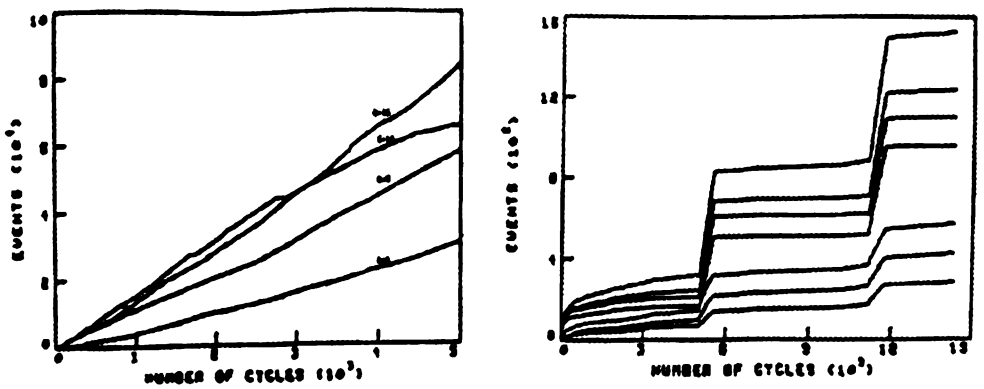

(a) (b)

Figure 3.3: Cumulative number of events as a function of the number of cycles (a) for unnotched specimens (b) for notched specimens. (Reprinted from [AMG84])

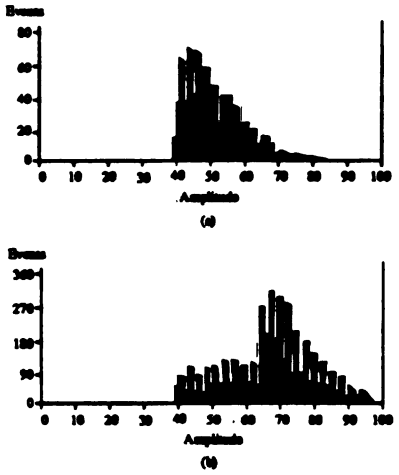

Figure 3.4: Acoustic emission for defect identification.

Some authors claim that there is a relation between the amplitude (or the energy) of the signal and the nature of the defect. One can see in Figure 3.4 [Lee90] a shift of the amplitude peak from 40–50 dB in Figure 3.4(a) to 65–75 dB in Figure 3.4(b) as static loading advances. This indicates that the damage mode changes. C-scan records would show that matrix cracking occurs in the first case, while delamination occurs in the second one.

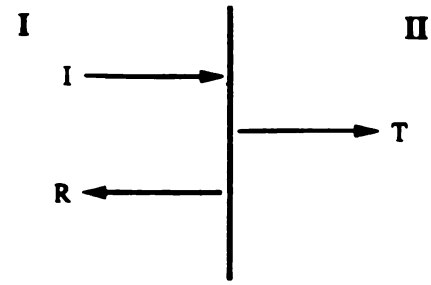

Figure 3.5: Reflection and transmission of the ultrasonic signal at a boundary. (I: Incident wave, R: Reflected wave, T: Transmitted wave).

3.3 Ultrasonic technique

The ultrasonic inspection technique is based on the fact that an impulsive shock at one side of a specimen creates an elastic deformation due to wave propagation in the object. The reflection and refraction behavior of the front wave at an interface plays an important role in ultrasonic inspection. We know that if an incident wave strikes the boundary between two different materials, part of its energy is transmitted and creates the refracted wave, while the other part is reflected back. The portion of energy transmitted and reflected is a function of the properties of the two materials (Figure 3.5 [BS89]).

This wave property can be used for flaw determination in materials. If we plot the energy received by the transducer as a function of time, we obtain what is called an A-scan. Figure 3.6 [BS89] shows the echoes received by the transducer placed on one extremity of a bar which contains a defect. The flaw echo can be easily seen in Figure 3.6(b). By knowing the sound velocity, we can determine the location of the defect in the specimen.

A similar display is created by angle-beam ultrasonic inspection when the wave penetrates the material inclined at a particular angle as shown in Figure 3.7 [BS89]. This technique of angle-beam inspection can be useful in detecting cracks which have a unique orientation that cannot be detected by non-oriented inspection.

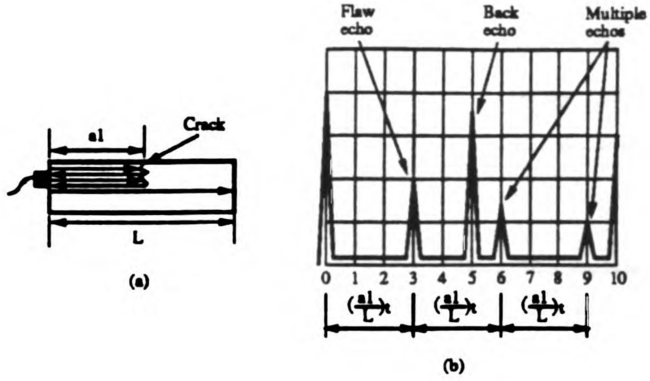

Figure 3.6: Typical pulse-echo response from a planar reflector. (a) Bar containing a crack. (b) Plot of energy received by the transducer as a function of time.

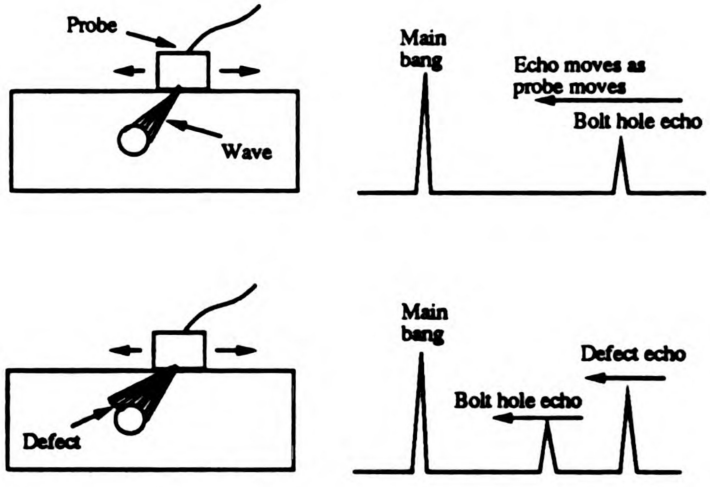

Figure 3.7: Angle-beam inspection of bolt holes.

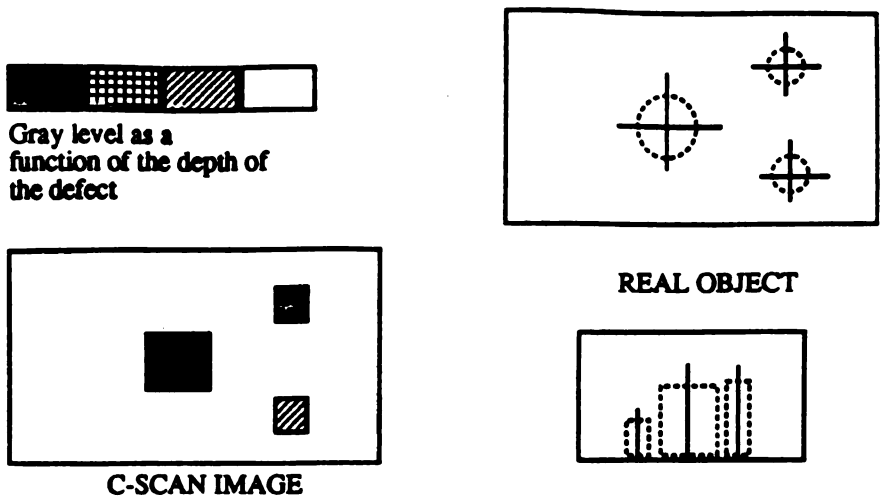

Figure 3.8: C-scan inspection.

The information which is available in the A-scan is basically one-dimensional, since only echo depth is indicated. Interpretation is required to characterize the flaw. A C-scan is obtained when the transducer is moved along the surface of the specimen. If the echo received by the transducer is nearer than the one usually received from the bottom of the specimen, a dot is plotted at the particular location. We can thus get the horizontal and vertical positions of the flaws. Additionally, flaw depth may be indicated with different grey levels as shown in Figure 3.8 [BS89].

Typical ultrasonic transducers are piezoelectric transducers. One property of this type of tranducers is that it can convert an electrical pulse into mechanical or stress waves and vice versa, so that they can be used either as emitters or as receivers. Array transducers can also be used to increase the speed of the scanning, since we scan the whole surface with only one pulse from each transducer. In addition, pulsing the probes in phased sequences (waiting for a small time between pulses of each transducer) can create an angle-beam configuration as shown in Figure 3.9 [BS89].

As an example of the use of ultrasonic C-scan for defect detection in composite materials, Figure 3.10 [Sen83] shows a sequence of C-scan records showing the growth of a delamination (white area around the circle) surrounding a hole in the specimen

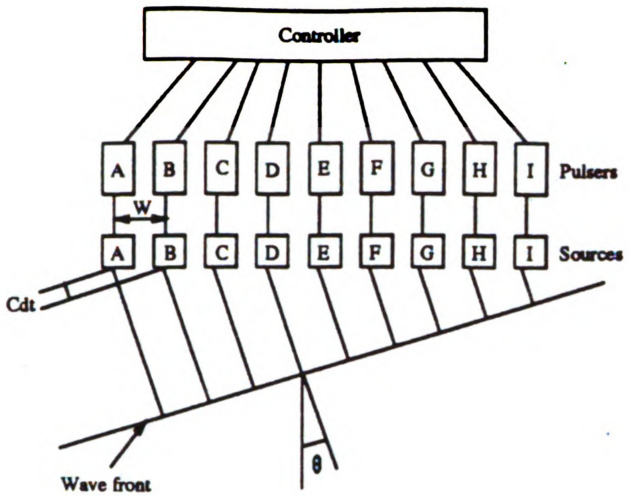

Figure 3.9: Angle-beam multiple probe array transducer.

as the number of loading cycles increases.

3.4 Radiographic technique

Radiographic techniques are based on the propagation of energy from a source to an object and the evaluation of the energy pattern received by that object. The most familiar form of radiographic energy is electromagnetic, consisting of small packets of energy called photons. The receivers can be films or fluorescent screens. Figure 3.11 [BS89] shows a typical experimental setup for X-radiography. Particles are emitted by a source, transmitted through the specimen and their energy is received by a recording plane.

Photons can be in the form of protons, neutrons, α particles or β-, γ- or X-rays. The α particles and the β- and γ-rays are emitted by a particular element from an isotope group in which some of the atoms (like ^{14}C or ^{238}U) have an unstable nucleus whose disintegration causes the release of electromagnetic radiation. X-rays are emitted when high-speed electrons strike a suitable target causing an unstable

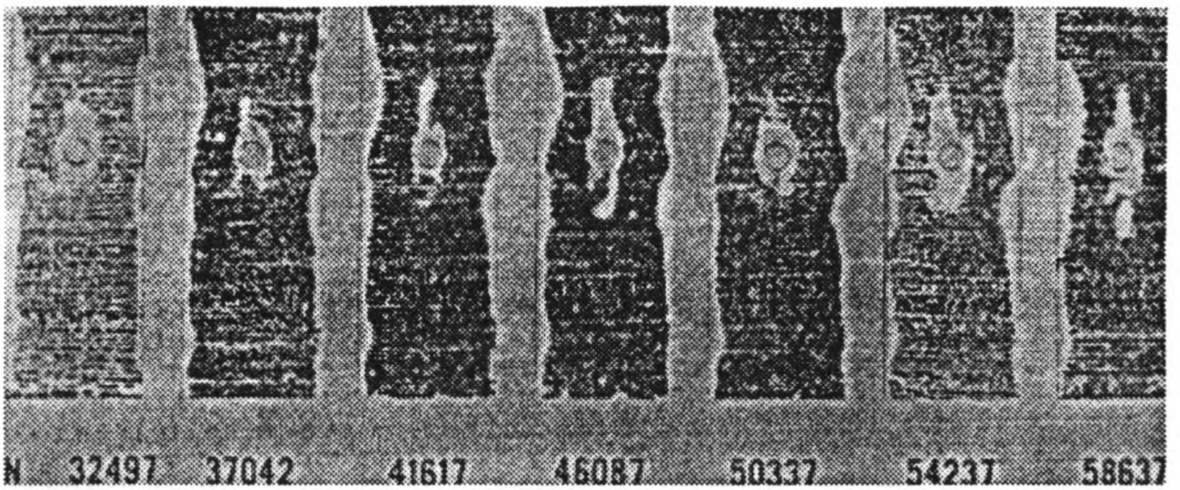

Figure 3.10: Sequence of C-scan records showing fatigue induced delamination growth in a specimen with a circular hole. (Reprinted from [Sen83])

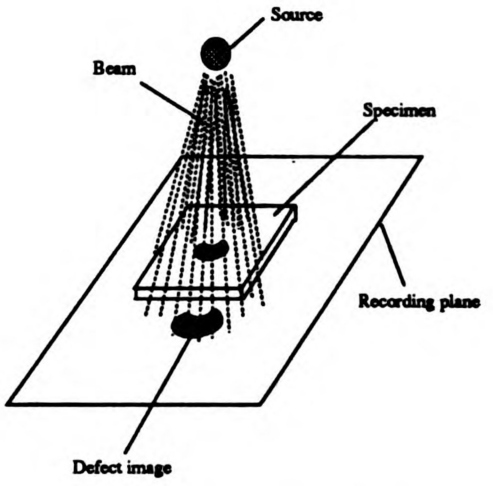

Figure 3.11: Layout of radiographic inspection.

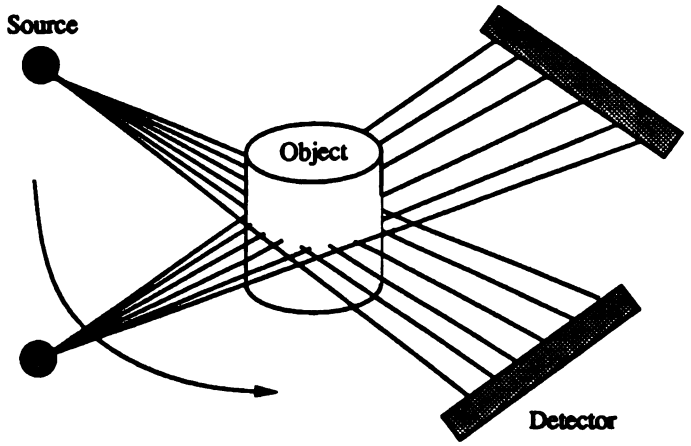

Figure 3.12: Scanning set-up for computer-aided tomography.

condition at the target area that results in the release of photons.

Each material is characterized by its attenuation coefficient. The photoelectric effect, the Compton scattering effect and the Rayleigh scattering effect (which define the manner in which the energy is transmitted from the photon to the electron which has been hit by that photon) contribute to this attenuation which permit detection of different types of materials in the specimen.

The intensity of each object recorded on the film is proportional to the received energy which is also proportional to the attenuation coefficient of the object material. This enables discrimination between the flaws and rest of the material. The flaws will appear either darker or lighter in the image. Tomography is obtained when radiographic scans are made at a large number of orientations of sources, objects and receivers as shown in Figure 3.12 [BS89].

To make X-ray imaging of defects in composite materials, an X-ray opaque penetrant is used to bring out details of the damage. The penetrant is necessary to provide sufficient contrast between the damaged area and the undamaged area. The bigger the amount of penetrant the defect can contain, the darker it will appear in the image. Figure 3.13 [Sen83] shows X-radiography of the growth of defect in a specimen

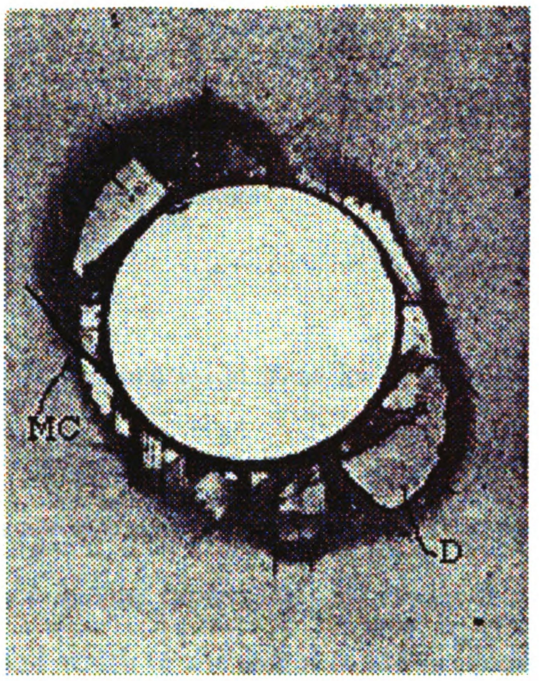

Figure 3.13: Penetrant enhanced X-radiography of specimen. (Reproduced from [Sen83])

containing a hole. Two kinds of defect have been induced during the machining of the hole. Matrix cracks are very deep and can contain a great amount of penetrant. Thus, they can be seen as long narrow dark lines (MC). The capillary forces acting on the penetrant are not high enough to retain the penetrant inside the delamination when the delamination thickness is large. As a result, the penetrant escapes from the regions of large delamination opening. Only the meniscus formed by the penetrant can be seen as dark area. Thus, delaminations appear in the photographs as broad bands of continuously varying grayness surrounding lighter gray regions. The interior regions of the delaminations may be lighter in color than the background (D).

3.5 Penetrant technique

Penetrant inspection utilizes the natural accumulation of a fluid around a discontinuity to create a recognizable indication of a crack or other surface opening. The

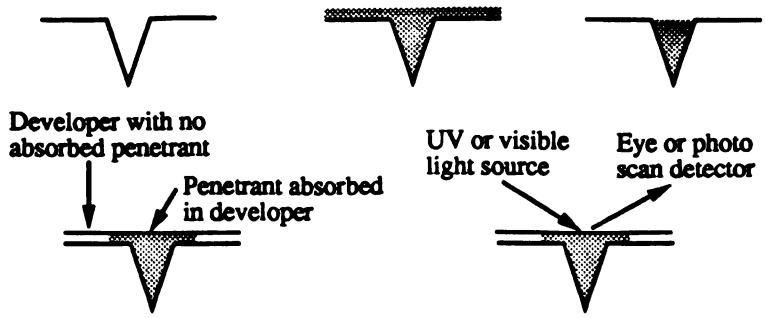

Figure 3.14: Experimentation steps for penetrant inspection.

different steps of this technique are described below and can be seen in Figure 3.14. First, the surface cracks are cleaned. The penetrant is then applied and subsequently removed from the surface leaving penetrant only inside the cracks. The developer increases the visibility and width of the defect to aid in identification.

It is important to notice that this method detects only surface flaws. The penetrant and the developer must contrast so that we can detect the defect. One solution is to use black or red penetrant with white developer. The other solution is to use ultraviolet lighting (black light) or monochromatic laser scanners with a fluorescent penetrant.

3.6 Thermographic technique

This method is based on the thermal properties of the defective regions in the material being inspected. If a short pulse of heat is applied to the surface of the specimen, its thermal equilibrium is unbalanced. After a certain amount of time, nonuniformities in temperature reveal the subsurface structures having different thermal resistivity to the heat flow. Figure 3.15 [MKCP87] shows the configuration of the experiment as well as the temperature distribution across the specimen surface at different times during the heating process. As can be seen, the temperature distribution is initially uniform over both the front and the back surfaces, but the position of the epoxy insert

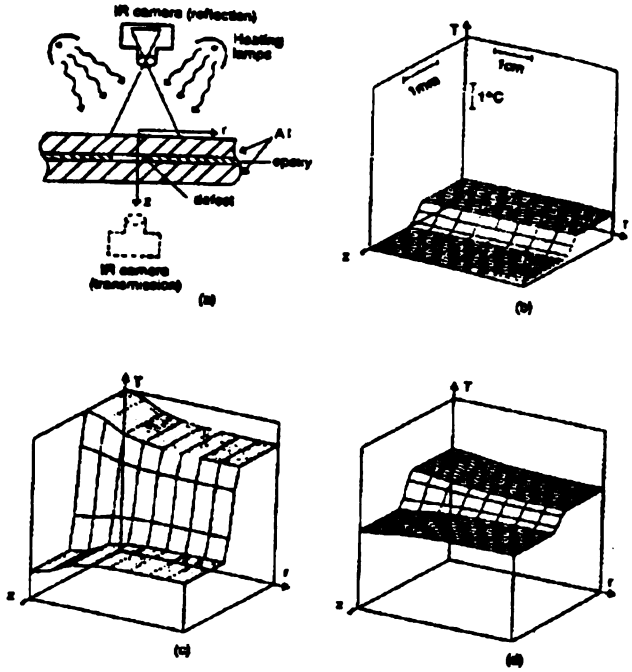

Figure 3.15: Thermal flow analysis (a) geometry, (b) to (d) computed thermal distribution after 0.1 s, 1.6 s and 4 s, respectively, of heating. (Reprinted from [MKCP87])

can be seen. Later, the temperature varies differently in the front surface and in the back surface, enabling the defect visualization.

Similar results can be obtained with line scanning heating as shown in Figure 3.16 [MKCP87] where the position of the defect can be identified on the curve of the temperature distribution. Infrared cameras are able to obtain images of the temperature distribution, where the isotherms can be separated using different grey levels.

3.7 Holographic technique

Holographic techniques can also be used in nondestructive inspection of composite materials. The method consists of recording a reference image of the specimen in such a way that the reconstructed hologram is located in space precisely where the object is located. If the specimen is then illuminated simultaneously with the holo-

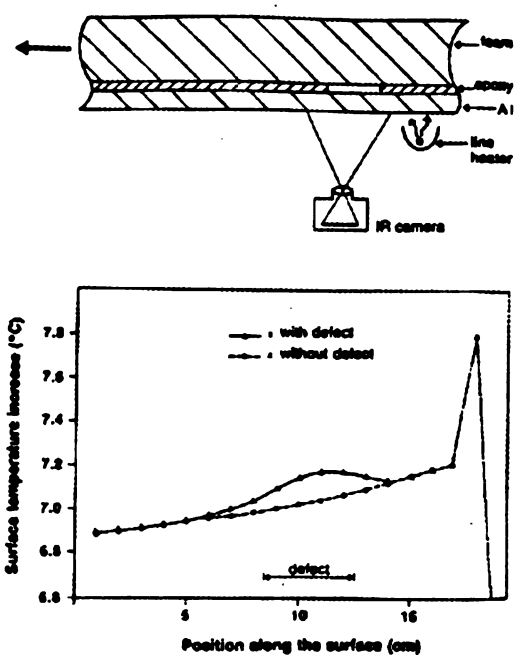

Figure 3.16: Line scanning thermographic technique. (Reprinted from [MKCP87])

gram, a pair of exactly superimposed images is seen. By applying a slight distortion (few micrometers), the two images form an interference pattern, commonly called holographic fringes and seen as light and dark lines. Damage can be seen from the interferogram in Figure 3.17 [Sen83]. In Figure 3.17(a), the fringes around the hole are quite difficult to locate and identify. After 50,000 loading-unloading cycles which resulted in an improtant delamination, the fringes are much more distinguishable in Figure 3.17(b).

3.8 Summary

We have seen that a number of nondestructive inspection techniques are available for testing composite materials. One of the major problems is that these techniques cannot detect all possible kinds of defects. Table 3.1 [SC83] gives the best techniques to employ when one wants to detect certain kinds of damage. This suggests the use of

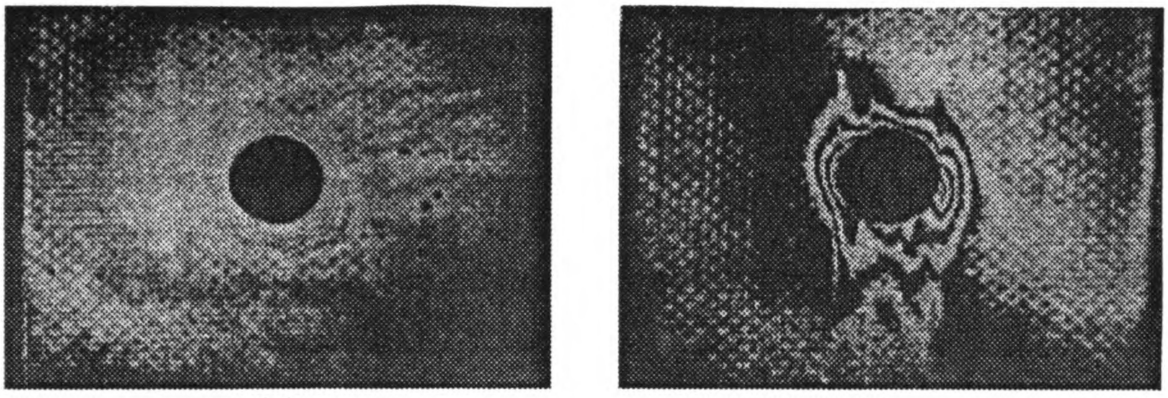

(a) (b)

Figure 3.17: Damage shown by interferograms.

more than one technique for defect and damage detection and location. The following chapter will present the techniques that we have decided to use in this thesis.

Table 3.1: Techniques for nondestructive evaluation of composite materials.

Defect	C-scan	Thermography	X-rays	Holography
Surface cracks	Yes	No	Yes	?
Delamination	Yes	Yes	Yes	Yes
Fiber breaks	?	No	Yes	?
Matrix cracks	No	No	Yes	?
Bond defects	Yes	Yes	Yes	?

Chapter 4

Experimental Procedure

4.1 Introduction

We have seen in Chapter 3 that a number of nondestructive inspection techniques are available for the testing of composite materials, and that more than one technique is needed if all possible types of defects have to be detected. In this chapter, we will describe the techniques that have been used in this thesis and how the experiments have been performed. We will also look at the specimens that have been fabricated with defects artificially inserted during the fabrication process.

4.2 Fabrication of the composite material specimens

The specimens were fabricated from prepreg tape (ref: IFRR 7781-50" from Ferro Corporation/Composite Division), which consists of glass fibers oriented in both 0° and 90° directions impregnated with polyester resin. Ten layers of prepreg were strongly pressed together and put in an autoclave under a pressure of 85 psi and at

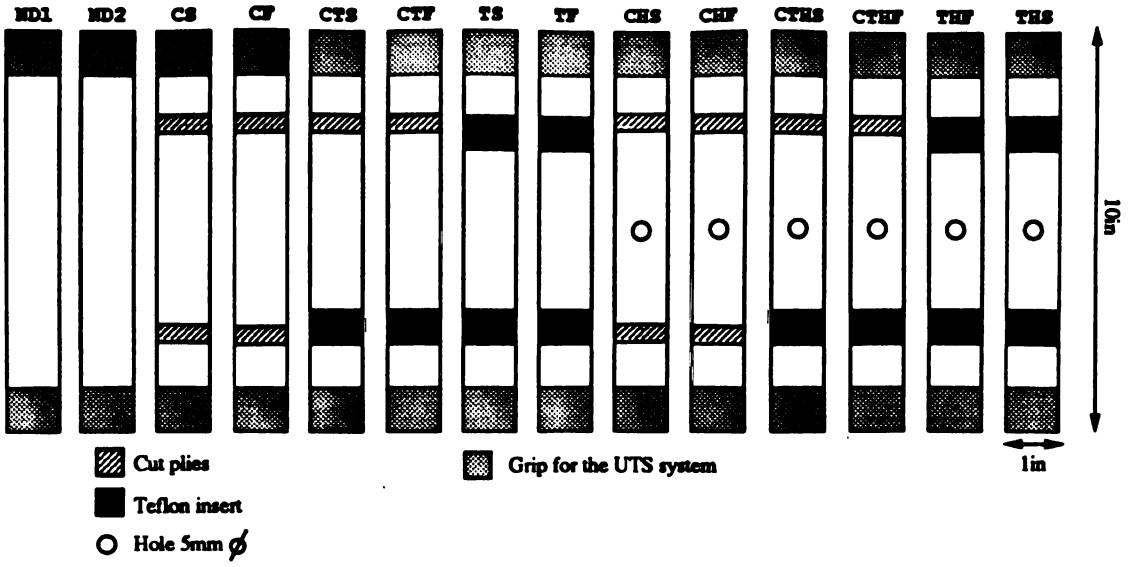

Figure 4.1: Set of test specimens.

a curing temperature of 260°F. Once the panels were solidified, after about 7 hours in the autoclave, they were cut into 10"×1" specimens.

Figure 4.1 is a description of the 14 test specimens that were fabricated for NDI inspection. Three kinds of defect were inserted:

- Cut plies: plies 4, 5, 6, and 7 were cut and an 1/8" wide section was removed;
- Teflon insert: a 1/4" wide teflon sheet was inserted between plies 5 and 6;
- Hole : a 5mm diameter hole was drilled in the middle of the specimen.

Three other specimens were fabricated for the purpose of testing the image processing algorithms (i.e. the image segmentation technique and the multi-sensor fusion procedure), and getting familiar with the equipment (i.e. the X-ray, C-scan, and acoustic emission systems). The three specimens were fabricated as shown in Figure 4.2.

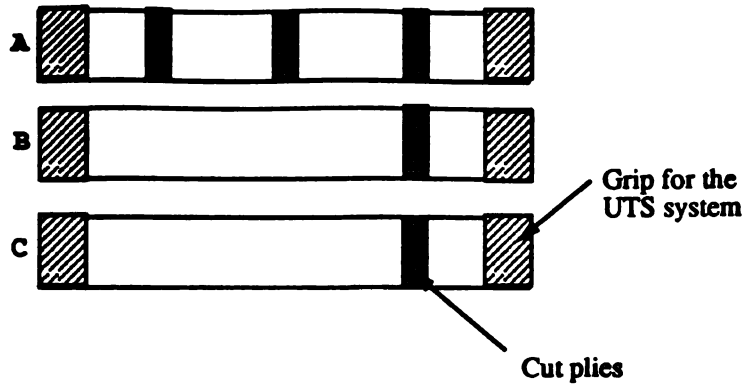

Figure 4.2: Set of non-test specimens.

4.3 The acoustic emission system

The acoustic emission experiments were performed using the Locan AT acoustic emission system from Physical Acoustic Corporation. This system is based on a PC-AT with MS-DOS operating system. It allows up to 4 channels for data acquisition (4 sensors can be connected). Data acquisition and real-time display are performed in parallel by two different processors. The software takes care of data acquisition and, in real time, displays the different acoustic emission graphs that the user has chosen to study. All the data are stored on disk and the test can be rerun at the user's convenience.

In order to obtain an acoustic emission signal, the specimen is subjected to a load. This was done using the United SFM Test System manufactured by United Calibration Corporation. This system consists of two parts: the loadframe, where the testing takes place, and the console, which controls the loadframe and processes and stores the data. A PC-AT with MS-DOS operating system controls the testing speed (i.e. the speed at which the specimen is pulled) by a feedback loop. A DC tachometer provides instant feedback of motor speed to stabilize the servo loop and provide coarse control. Various measurements can be displayed on the computer.

The experiments were performed as follows. The sensors were attached onto the

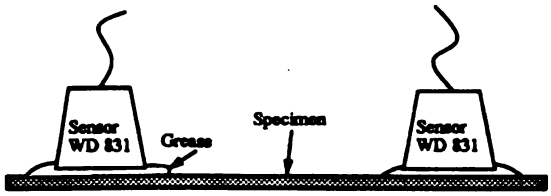

Figure 4.3: Position of the sensors on the specimen.

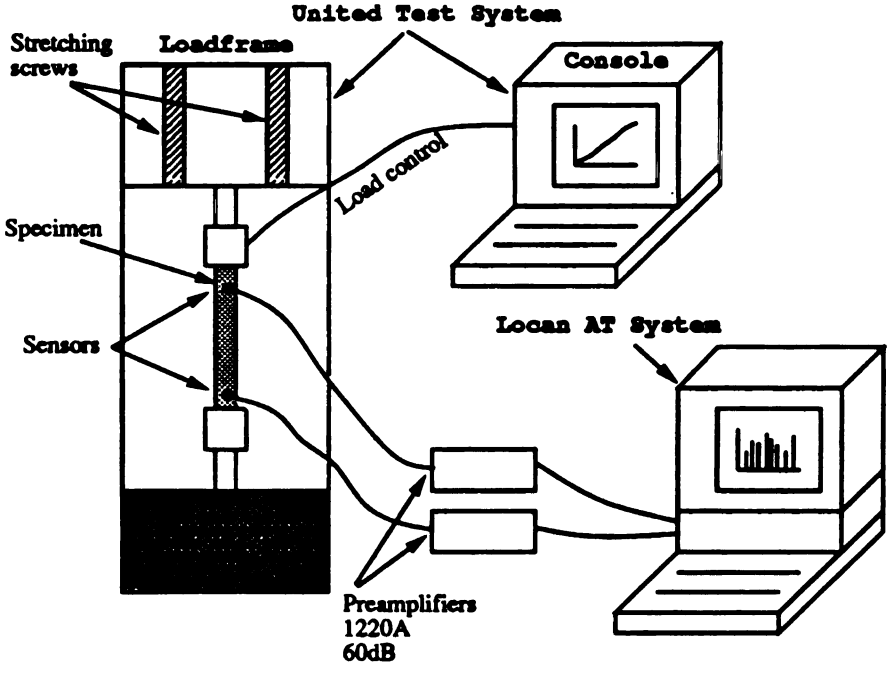

Figure 4.4: Acoustic emission setup.

specimen with grease in between as shown in Figure 4.3. The specimen was placed between the grips of the loadframe. The maximum reachable load was 20,000 lbs and the test was performed at a loading speed of 0.01 in/min (this means that the specimen was stretched 0.01" every minute). Acoustic emission was recorded and stored during the entire loading process. Figure 4.4 shows the setup of the experiment.

The specimens ND1, ND2, CF, CHF, CTF, TF, and THF were pulled until failure, so that the maximum strength which can be applied is determined. The maximum load to which the specimens without defects, ND1 and ND2, were subjected can be compared to the load which was applied to the specimens with defects. The other

Figure 4.5: Example of an X-ray image.

specimens were pulled to 1/2 of the maximum load, and a study of the new defect created by stretching was performed.

4.4 The X-radiography system

The X-ray images were obtained using the penetrant enhanced X-radiography technique as follows. The specimens were swabbed on the edges with diodobutane 1,4 (DIB) solution to penetrate the cracks. They were wiped off to remove the excess DIB after 30 seconds. They were then placed into a Hewlett Packard Faxitron 43805 point source X-radiography chamber atop a Kodak film (type NBB-8x10) cassette and exposed to X-rays for 2.5 minutes at 30 kV. The films were then developed and digitized using back illumination and a CCD camera. An example of such an image is shown in Figure 4.5. The size of the digitized X-ray images is 80×640.

4.5 The ultrasonic C-scan system

Ultrasonic C-scan was done on a noncommercial system (built by Prof. Bong Ho's research group in the department of Electrical Engineering at Michigan State University) which is described in Figure 4.6. A pulse is sent by the transducer at a frequency of 2.25 MHz. The transducer is moved over the specimen using stepping motors which accept a minimum step of 0.3 mm. The echos are then received by the same transducer and transferred to a computer using an analog-digital converter having a frequency of 40 MHz. A program running on a PC-XT determines the

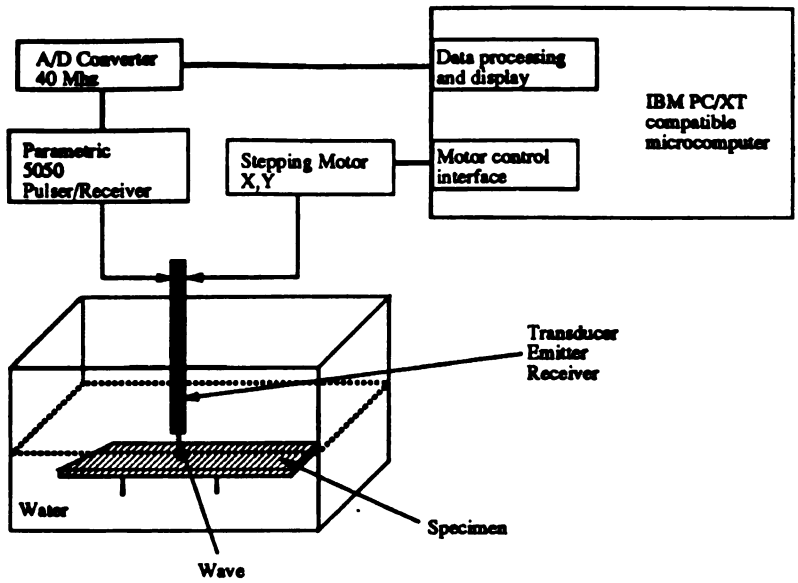

Figure 4.6: Setup of the C-scan experiments.

Figure 4.7: Example of a C-scan image.

location of the first echo and assigns a depth value at each step. If the depth value is converted to an integer between 0 and 255, a gray level image of the scan can be displayed as in Figure 4.7. The size of the C-scan images is 60×360.

4.6 Summary

Three nondestructive inspection techniques were used, namely acoustic emission, X-radiography and ultrasonic C-scan. The strategy used in practise would be to pull the specimen and record acoustic emission signals until defects are located, but before the specimen breaks. The parts where defects have been located would be X-rayed and C-scanned, and the X-ray and C-scan images would be analyzed in order to identify the defect.

In this project, we wanted to evaluate the performance of this strategy, so the

methodology is slightly different. The entire specimen is first X-rayed and C-scanned in order to see the defects beforehand. Then the specimens are subjected to a load and the positions of the defects are confirmed. The specimens are X-rayed and C-scanned again, since pulling the specimens might create new defects. The defect images (C-scan and X-ray) are then fused to obtain a map of the defects before and after pulling. This map is compared to the position of the defects which is known since they have been inserted during fabrication.

It can be seen in Figures 4.5 and 4.7 that the defects are visually distinguishable in the X-ray and C-scan images, but the detection of these defects needs to be automated. The topic of the next chapter is the automatic extraction of the defects from the X-ray and C-scan images.

Chapter 5

Image Segmentation Techniques

5.1 Introduction

Once the images have been obtained, it is necessary to extract the defective regions from the background. This can be done by image segmentation techniques. Segmentation techniques assign a label to each pixel of the image specifying whether the pixel belongs to an object (a defect) or the background (the part of the specimen without defect). Many different techniques for image segmentation have been reported in the literature. Four different techniques will be presented and analyzed in this chapter.

5.2 Background

A number of surveys on both thresholding techniques and segmentation techniques have been published in the literature [FM81, HS85, SSW88]. It is generally agreed that there is no single segmentation algorithm which will work for all images. One of the reasons for this lack of a universal algorithm for image segmentation is that a two-dimensional image can represent a potentially infinite number of possibilities for

object-background separation. At the present time, each image processing application requires a different segmentation algorithm. We categorize segmentation techniques into four different classes: analysis of the histogram of the image, clustering, edge detection, and region extraction.

5.2.1 Analysis of the histogram of the image

The histogram of an image is computed by counting the number of pixels in the image at each possible gray level value. Different techniques can be used to find the threshold to segment the image. If the object is darker than the background and the threshold chosen is t, then a pixel with gray level value x is assigned to the object region if $x < t$. The p-tile method consists of mapping p% of the lowest gray levels into the object regions and (100-p)% of the highest gray levels into the background.

If the image is not uniform, but contains objects and background, then the histogram contains peaks and valleys. The mode method finds these peaks and defines the threshold value as the gray level corresponding to the valley between the peaks. Weszka [WNR78] proposed a method to sharpen the valley between the modes by including only those pixels which low Laplacian or gradient value in constructing the histogram. Rosenfeld [Ros78] proposed an iterative histogram modification technique to sharpen the peaks for image enhancement and threshold selection. Different adaptive thresholding techniques have also been published and two of them will be studied later in this chapter.

5.2.2 Clustering

A label is assigned to each pixel based on a certain number of features observed or computed at each pixel. Each distinct region in the image is assumed to form

a compact cluster in the space of these characteristic features. For example, the features can be the three color components (red, green, and blue) of the image. They can also be texture features, such as the average of the neighborhood of the pixel or the outputs of different spatial frequency and orientation filters. Panda [PR78] suggested a clustering method in 2-dimensional space: the gray level of the pixel and the edge value of the pixel.

5.2.3 Edge detection

Another common technique for image segmentation is edge detection. Once the edge points have been detected and the contours extracted, the regions consist of the pixels inside the contours. [RK82] surveyed a number of edge detection algorithms. A comonly encountered difficulty with this method is that the contours are often not closed.

5.2.4 Region extraction

There are three different approaches to region extraction. One can start with very small regions (i.e., one pixel) and use a region growing algorithm to extract bigger regions. On the other hand, one can start with the entire image and use a region splitting algorithm to obtain smaller homogeneous regions. Horowitz and Pavlidis [HP74] approached the segmentation problem by using a "split and merge" principle. They merge adjacent regions having similar properties and split those regions that have large differences in their properties.

In the following sections of this chapter, we will present four methods for segmentation of images, along with the results they produce on artificial images as well as real images. Three of these methods are well known in the image processing literature

and the fourth method is based on modification of a recently published segmentation algorithm.

5.3 Study of three image segmentation techniques

Image segmentation is a simple problem when the gray levels of the pixels in the background do not overlap the gray levels of the pixels in the object. The images obtained by C-scan and X-radiography are far from being ideal in this respect. Not only do these images contain sensor noise, which is typically present in any kind of image acquisition, but they are also corrupted by nonuniform illumination. This is due to the image acquisition apparatus. For example, the specimen might not be perfectly horizontal when the ultrasonic transducer scans it, or the back illumination used for digitizing X-ray films might not be uniformly distributed over the light table. In this section, three different techniques will be presented along with the results they produce on test images which have about the same noise properties as the real X-ray and C-scan images.

5.3.1 Simple thresholding

Ideally, one would like to have a bimodal histogram of the gray levels present in the image. A bimodal histogram is shown in Figure 5.1, where one mode of the histogram corresponds to the gray levels of the object pixels, while the other mode captures the gray levels of the background pixels. The threshold level is then chosen to be the gray level between the two modes.

The simplest segmentation method is based on Bayes' decision theory in pattern recognition. The gray level histogram of the image is computed and smoothed using a 1×5 window with the following weights $\left[\frac{1}{9}, \frac{2}{9}, \frac{3}{9}, \frac{2}{9}, \frac{1}{9}\right]$. Then, two component

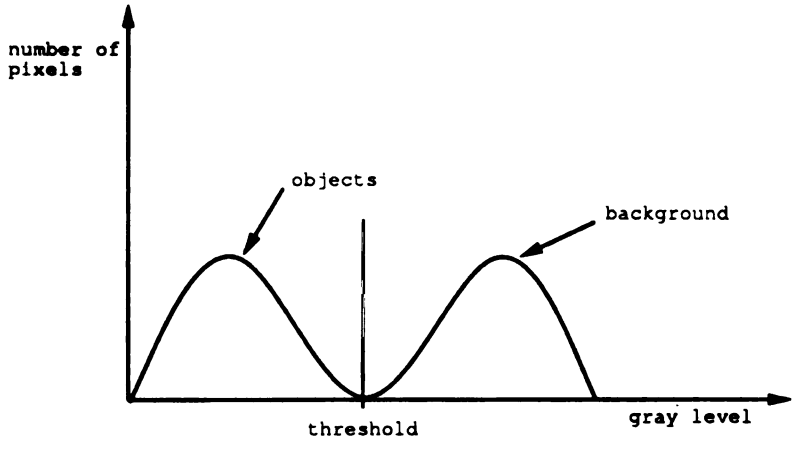

Figure 5.1: Histogram showing objects well-separated from the background.

densities are extracted (corresponding to the objects and the background) from the mixture density associated with the histogram. It is commonly assumed that both the background and the object densities are Gaussian. Thus, the mixture density is approximated by:

$$h(x) = A_o \exp\left\{-\frac{(x-\mu_o)^2}{2\sigma_o^2}\right\} + A_b \exp\left\{-\frac{(x-\mu_b)^2}{2\sigma_b^2}\right\}, \tag{5.1}$$

where x is the gray level value, $h(x)$ is the probability of a pixel having gray level x, A_o and A_b are the mixing parameters ($A_o\sqrt{2\pi}\sigma_o + A_b\sqrt{2\pi}\sigma_b = 1$), μ_o and σ_o^2 denote the mean and variance of the object distribution, and μ_b and σ_b^2 are the mean and variance of the background distribution. The six parameters $(A_o, \mu_o, \sigma_o, A_b, \mu_b, \sigma_b)$ are approximated using a least squares method for non-linear models (see Appendix A).

After the parameters of the mixture density have been estimated, the threshold value is computed using the Bayes' decision rule with a 0-1 loss function and assuming different prior probabilities for the objects and the background. Thus, a pixel with a

gray level x is assigned to the object if:

$$A_o \exp\left\{-\frac{(x-\mu_o)^2}{2\sigma_o^2}\right\} > A_b \exp\left\{-\frac{(x-\mu_b)^2}{2\sigma_b^2}\right\}. \tag{5.2}$$

The threshold value t is then defined by:

$$A_o \exp\left\{-\frac{(t-\mu_o)^2}{2\sigma_o^2}\right\} = A_b \exp\left\{-\frac{(t-\mu_b)^2}{2\sigma_b^2}\right\}. \tag{5.3}$$

This results in the following quadratic equation:

$$(\frac{1}{2\sigma_o^2} - \frac{1}{2\sigma_b^2})t^2 - (\frac{\mu_o}{\sigma_o^2} - \frac{\mu_b}{\sigma_b^2})t + \frac{\mu_o^2}{2\sigma_o^2} - \frac{\mu_b^2}{2\sigma_b^2} + \ln\frac{A_b}{A_o} = 0. \tag{5.4}$$

This equation can easily be solved and produces two values for t. The positive value is used as the threshold value t. The image is then thresholded using this threshold value as follows:

$$f_t(p,q) = \begin{cases} 1 & \text{if } f(p,q) > t \\ 0 & \text{otherwise,} \end{cases} \tag{5.5}$$

where $f(p,q)$ is the gray level of pixel (p,q) in the original image. Figure 5.2 illustrates that the threshold is chosen at the gray value where the two component densities intersect, or where the probability of a gray level belonging to the object is equal to the probability of it belonging to the background. Figure 5.2 shows the histogram of the image in Figure 5.4(c), along with the computed Gaussian densities, mixture density and threshold value. The estimated parameters for this image are: $A_o = 1.4 \cdot 10^{-3}$; $\mu_o = 51$; $\sigma_o = 34$; $A_b = 7.9 \cdot 10^{-3}$; $\mu_b = 202$; $\sigma_b = 47$. The threshold for this image is $t = 98$.

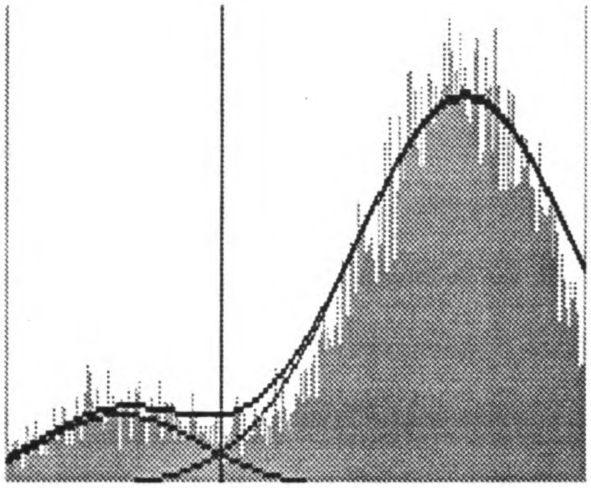

Figure 5.2: Threshold determination using mixture decomposition. The test image is a 40×40 square of gray level 50 on a background of gray level 200 with additive gaussian noise with standard deviation 40. The figure shows the mixture density, the two estimated component densities, and the threshold.

5.3.2 Adaptive thresholding

When there is a large range of variation in gray values from one part of the image to the other, a single fixed threshold cannot be used for the entire image. A method was developed by Chow and Kaneko [CK72], and studied by Nakagawa and Rosenfeld [NR79], that attempts to solve this problem. This method assigns a different threshold value to each pixel, as follows. The image is divided into several subimages. For each subimage, the gray level histogram is smoothed. The least squares method described in Appendix A is applied to fit a mixture of Gaussian densities to each subhistogram. The resultant best fitting histogram is tested for bimodality based on the criteria (assuming without loss of generality that $\mu_1 \leq \mu_2$ and $\sigma_1 \leq \sigma_2$):

$$\mu_2 - \mu_1 > 4 \tag{5.6}$$

$$0.1 < \frac{\sigma_1}{\sigma_2} < 1.0 \tag{5.7}$$

$$\delta = \frac{\text{Minimum value of } f \text{ in } [\mu_1, \mu_2]}{\text{Min}[f(\mu_1), f(\mu_2)]} < 1. \tag{5.8}$$

When the test for bimodality succeeds, a threshold is computed as described in the previous section. Thresholds need to be defined for the windows which did pass in the bimodality test. If we call $T(p,q)$ the threshold for window centered at pixel (p,q), then a threshold is computed for a window where no threshold has yet been assigned, provided that at least one of its neighboring windows other than a diagonal neighbor has had a threshold assigned, using the following formula:

$$\begin{aligned} T(p,q) \;=\; & T(p+1,q) + T(p-1,q) + T(p,q+1) + T(p,q-1) + \\ & \frac{1}{\sqrt{2}}(T(p+1,q+1) + T(p+1,q-1) + \\ & T(p-1,q+1) + T(p-1,q-1)). \end{aligned} \tag{5.9}$$

The thresholds are then smoothed among the neighboring subimages by applying the following mask:

$$\begin{bmatrix} 1/\sqrt{2} & 1 & 1/\sqrt{2} \\ 1 & 2 & 1 \\ 1/\sqrt{2} & 1 & 1/\sqrt{2} \end{bmatrix} \tag{5.10}$$

A threshold value is then computed by bilinear interpolation for every pixel in each subimage as follows. Let the pixel P be surrounded by four subimages with centers A, B, C, and D and associated thresholds T_A, T_B, T_C, and T_D; a, b, c, and d are the distances from P to the subimage centers as shown in Figure 5.3. The threshold for pixel P is taken to be:

$$T_P = \frac{1}{(a+b)(c+d)}(bdT_A + bcT_B + daT_C + caT_D). \tag{5.11}$$

This formula takes into account the distances between P and each of the window

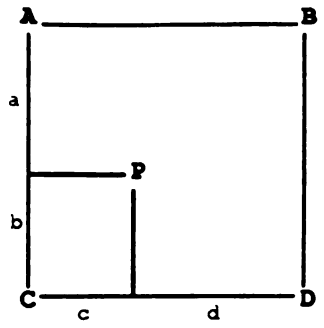

Figure 5.3: Interpolation of the threshold values.

centers, in addition to the values of the thresholds at the window centers. The closer P is to a window center, the higher the coefficient assigned to the threshold of that window center. For example, if P is in the middle of the square $ABCD$, then $T_P = (T_A + T_B + T_C + T_D)/4$. The image is then thresholded using the threshold values assigned to each pixel, and becomes:

$$f_t(p,q) = \begin{cases} 1 & \text{if } f(p,q) > T(p,q) \\ 0 & \text{otherwise.} \end{cases} \tag{5.12}$$

5.3.3 Iterated Conditional Modes (ICM)

This method was developed by Besag [Bes86] to incorporate spatial context in computing the threshold. Consider an $M \times N$ image containing MN pixels. Let y_t be the observed gray level at pixel t and x_t be the true (unobserved) label at pixel t, $x_t \in [0,1]$. The image segmentation problem can be defined as follows: given the set of gray levels $Y = \{y_t\}$, $(t \in [1, MN])$, estimate the set of labels $X = \{x_t\}$, $(t \in [1, MN])$. The gray values are assumed to be conditionally independent and normally distributed. So, the joint gray level density of the MN pixels can be written as:

$$f(Y = y | X = x) = \prod_{t=1}^{MN} f_t(y_t | x_t). \tag{5.13}$$

The conditional density $f_t(y_t|x_t)$ has a Gaussian distribution:

$$f_t(y_t|x_t) = \frac{1}{\sqrt{2\pi\sigma_{x_t}^2}} \exp\left\{-\frac{(y_t - \mu_{x_t}^2)^2}{2\sigma_{x_t}^2}\right\}. \tag{5.14}$$

The Markov property states that pixels spatially close together tend to have similar labels. Therefore, contextual information is incorporated in image segmentation through a Markov Random Field. The joint density of all the MN true labels is equivalent to a Gibbs process:

$$P(X = x|Y = y) = \frac{\exp\{-U(x|y)\}}{Z_y}, \tag{5.15}$$

where Z_y is a normalizing constant and $U(x|y)$ is the energy function that has to be minimized. As we want to include contextual information, $U(x|y)$ has to depend on the gray values of the neighboring pixels. So, it can be stated that:

$$P(X_t = x_t|X_{\partial t} = x_{\partial t}, Y = y) = \frac{\exp\{-U_t(x_t|x_{\partial t}, y_t)\}}{Z_t}, \tag{5.16}$$

where $X_{\partial t}$ is the neighborhood of pixel t. We have assumed a pairwise interaction model, so that:

$$U_t(x_t|x_{\partial t}, y_t) = \frac{1}{2}\ln(\sigma_{x_t}^2) + \frac{(y_t - \mu_{x_t})^2}{2\sigma_{x_t}^2} + \sum_{r=1}^{c} \theta_r[J(x_t, x_{t:+r}) + J(x_t, x_{t:-r})], \tag{5.17}$$

where c is the number of neighbors that are considered, $x_{t:+r}$ is defined according to the grid in Table 5.1, and $J(a, b) = -1$ if a and b are equal and is null, otherwise.

Besag suggested using a simple model where $\theta_r = \beta$, $\forall r$ and using a second-order neighborhood, that is $c = 4$.

The ICM algorithm contains the following three main steps:

Table 5.1: Definition of a pixel neighborhood for the ICM method.

t:-11	t:-7	t:-6	t:+8	t:+12
t:-9	t:-3	t:-2	t:+4	t:+10
t:-5	t:-1	t	t:+1	t:+5
t:-10	t:-4	t:+2	t:+3	t:+9
t:-12	t:-8	t:+6	t:+7	t:+11

1. Initialize $\hat{X}$ by maximizing $f_t(x_t|y_t)$ at pixel t. In other words, initial labels are assigned to pixels based on the maximum-likelihood rule (non-contextual).

2. For all pixels, update $\hat{x}_t$ to the value of x_t that minimizes the energy function in Equation(5.17).

3. Repeat (2) a given number of times.

Several MRF-model based segmentation algorithms have been studied by Dubes et al. [DJNC90] and they claim that the ICM method gives the best results. It seems that 7 iterations are enough to produce good segmentation results with the optimum value of 1.5 for β.

5.3.4 Results on test images

The results of these three segmentation methods (simple thresholding, adaptive thresholding and ICM) are given in Figures 5.4, 5.5 and 5.6 for eight noisy test images and three nonuniformly illuminated test images. Type 1 images (Figure 5.4) contain a 40×40 pixel square of gray level 50 on a background of gray level 200 with different levels of additive gaussian noise having a standard deviation varying from 20 to 50. Type 2 images (Figure 5.5) contain a square with gray level 100 on a background with a gray level of 150 with the same levels of additive gaussian noise as in type 1 images. Since the difference between the square gray level and the background gray level is

smaller in this second set of images than in the first one, the signal to noise ratio is also smaller for type 2 images. Type 1 and type 2 images each are 100×100 pixels in size. The third set of images (Figure 5.6) were captured by a CCD camera by putting dark objects on a table and directing a light source to one corner of the table to simulate nonuniformly illuminated scenes. These real images are of size 150×150 pixels.

Unless the variance of the additive Gaussian noise is very small, both the simple thresholding and the adaptive thresholding methods give poor segmentation results. The correct segmentation could be found by applying a median filter to smooth the thresholded images only for images in Figures 5.4(a), 5.4(b), 5.4(c), and 5.5(a) which are images with relatively high signal to noise ratio.

The window size for the adaptive thresholding method is 20×20 for Figures 5.4 and 5.5 and 25×25 for Figure 5.6. The window size must be small enough, so that a small object does not get lost in the background. At the same time, the window must be large enough, so that the local histogram is meaningful. For our images, 400 to 625 pixels are distributed among 256 histogram bins. Such a small number of pixels might not properly define the histogram, but a bigger window size would not find the segments given the size of the objects. ICM gives very good segmentation results in the case of additive Gaussian noise but cannot properly segment a nonuniformly illuminated scene. This is probably due to the fact that, for nonuniformly illuminated scenes, the conditional independence assumption is not satisfied. Since in X-ray and C-scan images nonuniform illumination is more important than additive noise, another method has to be found to segment the images better.

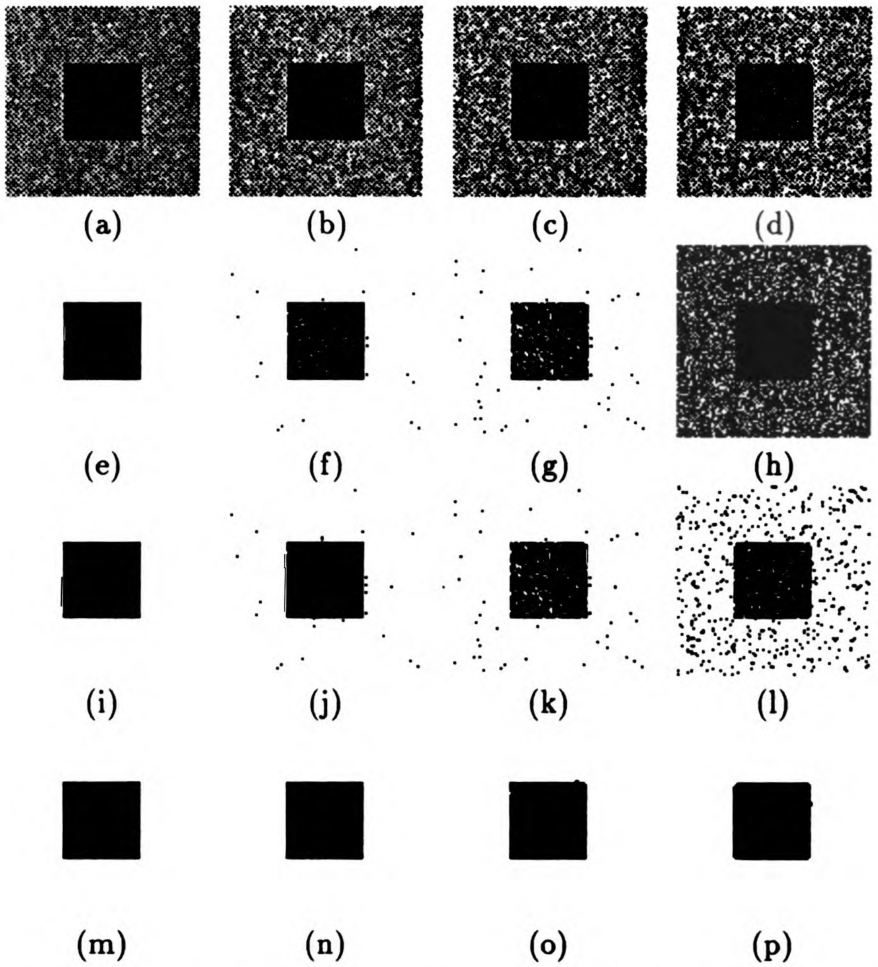

Figure 5.4: Segmentation results using simple thresholding, adaptive thresholding and ICM on noisy images of type 1. (a-d) input images, the standard deviation of the Gaussian noise process is 20 for (a), 30 for (b), 40 for (c) and 50 for (d). (e-h) segmentation using simple thresholding. (i-l) segmentation using adaptive thresholding. (m-p) segmentation using ICM.

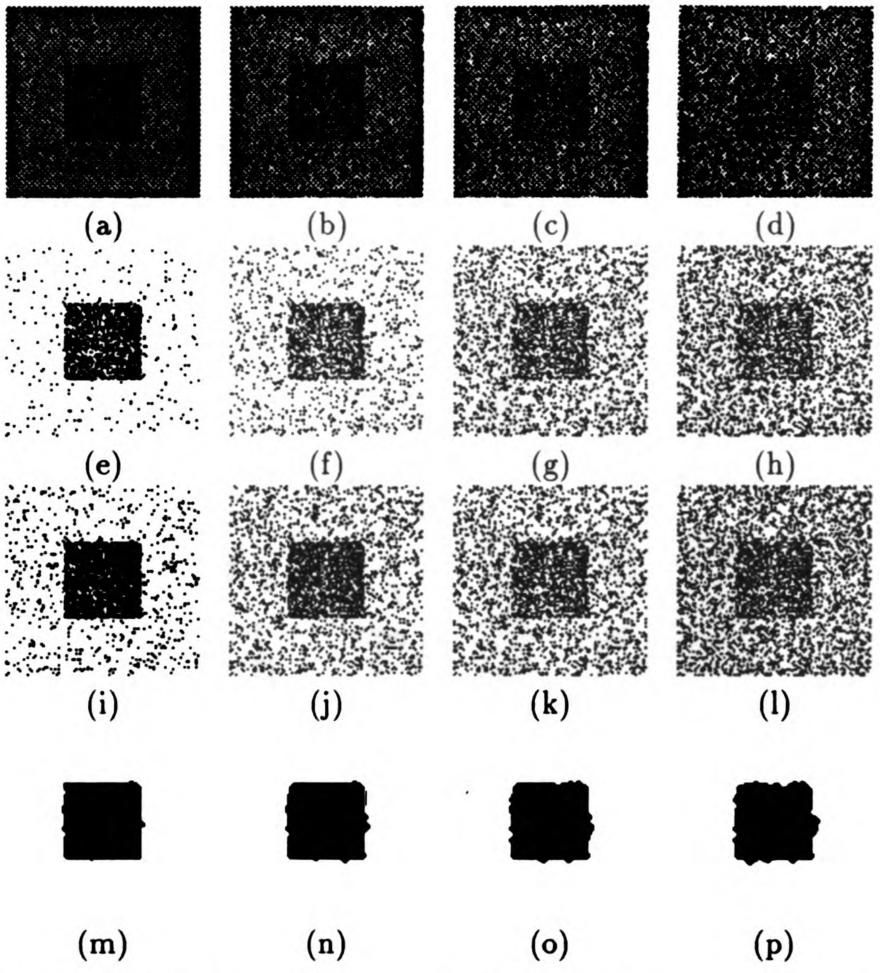

Figure 5.5: Segmentation results using simple thresholding, adaptive thresholding and ICM on noisy images of type 2. (a-d) input images, the standard deviation of the Gaussian noise process is 20 for (a), 30 for (b), 40 for (c) and 50 for (d). (e-h) segmentation using simple thresholding. (i-l) segmentation using adaptive thresholding. (m-p) segmentation using ICM.

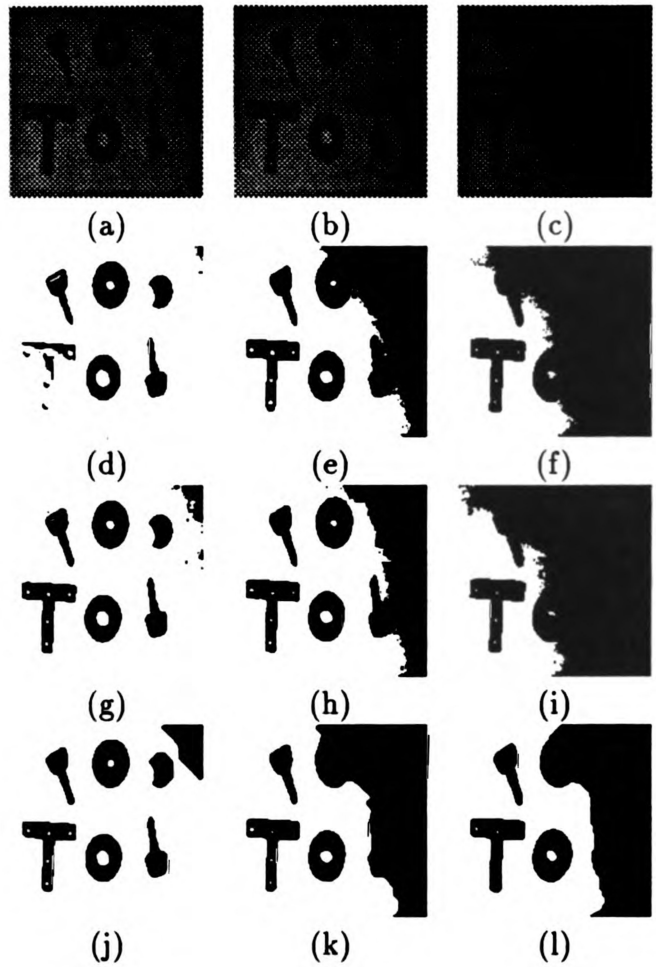

Figure 5.6: Segmentation results using simple thresholding, adaptive thresholding and ICM on nonuniformly illuminated images. (a-c) input images. (d-f) segmentation using simple thresholding. (g-i) segmentation using adaptive thresholding. (j-l) segmentation using ICM.

5.4 A new adaptive thresholding method

This section introduces a new adaptive thresholding method which has better performance on images with nonuniform illumination and gaussian noise.

5.4.1 Yanowitz and Bruckstein's algorithm

The Yanowitz and Bruckstein [YB89] algorithm constructs a thresholding surface by interpolating the image gray levels at points where the gradient is high, indicating probable object edges. The method is illustrated in Figure 5.7. Figure 5.7(a) shows the gray levels along one scan line of the image where two peaks or objects can be seen. We want to compute a surface such that the gray levels of the objects of interest in the image will be above the surface while the gray level of the background will be below the surface, or vice versa. It can be seen in this figure that the edge points of the objects are good candidates for the interpolation of this surface. Figure 5.7(b) shows that pixels with high gradient magnitude are identified as edge pixels. The gray level values of these edge points are to be interpolated over the entire image.

The first step of the algorithm consists of edge point detection. This can be done by computing the gradient of the image or applying a mask at each pixel in the image. Then, applying a threshold to the gradient image will keep only those pixels with high gradient magnitude. The thresholded image is then thinned to keep only one pixel-wide edges. The threshold surface is interpolated from the so-determined edge pixels called P_i.

There are different ways of interpolating a surface given a set of fixed points. Yanowitz and Bruckstein suggest setting the Laplacian of the surface to zero so that the surface is continuous and smooth in the first and second derivatives. The Laplacian of a surface $S(x, y)$ is defined as the sum of the second derivative of the surface

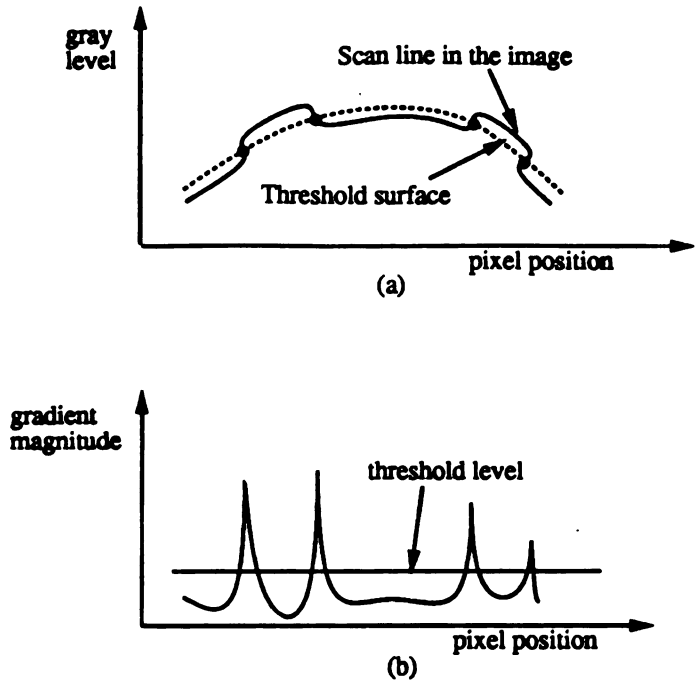

Figure 5.7: Interpolation of a threshold surface in Yanowitz and Bruckstein method. (a) Gray level distribution along one scan line, (b) Gradient magnitude along the scan line.

in the x and y directions, $L(S) = \frac{\partial^2 S}{\partial x^2} + \frac{\partial^2 S}{\partial y^2}$. At first, the surface is set to gray level 0 everywhere except at the points P_i, which are set to their initial gray level values. We then have:

$$S(x,y) = \begin{cases} f(x,y) & \text{if } \exists i \text{ such that } (x,y) = P_i \\ 0 & \text{otherwise,} \end{cases} \tag{5.18}$$

where $f(x,y)$ is the gray level value at point (x,y). The discrete Laplacian is computed for each pixel at position (x,y) by:

$$R(x,y) \leftarrow S(x-1,y) + S(x+1,y) + S(x,y-1) + S(x,y+1) - 4S(x,y). \tag{5.19}$$

The goal is to have the residual R approach zero as the number of iterations increases. R is called the residual by Yanowitz and Bruckstein since it is never null

but tends to approach zero as the surface discontinuities tend to disappear. Then, the value of the surface at every pixel different from the P_i's is updated by:

$$S(x,y) \leftarrow S(x,y) + \frac{\beta R(x,y)}{4}, \tag{5.20}$$

where $1 < \beta < 2$. This iterative process is stopped when the maximum residual R is smaller than a given small quantity (0.01, for example). Yanowitz and Bruckstein suggest that $\beta = 1.5$ gives the best results. Once the thresholding surface has been found, the image is thresholded as follows:

$$f_t(x,y) = \begin{cases} 1 & \text{if } f(x,y) > S(x,y) \\ 0 & \text{otherwise.} \end{cases} \tag{5.21}$$

Using this interpolation scheme, it can be seen that there are some problems in computing the threshold values at the boundary of the image. We cannot assume that the image wraps around, since it is not uniformly illuminated; the right side of the image might be much darker than the left side. In C-scan and X-ray images, the objects that we are looking for are darker than the background. Thus, it has been decided to fix the value of the border of the surface to gray level 0 during the whole process, so the obtained surface will be as shown in Figure 5.8. Since the object is the only part of the image that is below the surface, it can be extracted using this method. This makes it impossible to detect objects at the boundaries of the image, but this is not a problem, since the surface that will be C-scanned or X-rayed will always be larger than the defect itself.

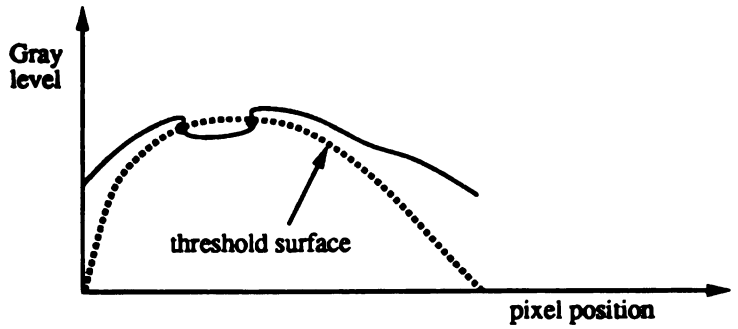

Figure 5.8: Interpolation of the threshold surface in the case of C-scan or X-ray images.

5.4.2 Mask operators for edge detection

Yanowitz and Bruckstein do not clearly specify which edge detector should be used. Therefore, this method has been tried on the same set of images as before, namely noisy (type 1 and type 2) images and nonuniformly illuminated images, using different edge detectors. Three different edge detectors from the HIPS Package mask library, see [LCS84], were tried as shown below.

(i) 3-level (3×3) masks

$$\begin{bmatrix} 1 & 0 & -1 \\ 1 & 0 & -1 \\ 1 & 0 & -1 \end{bmatrix} \quad \begin{bmatrix} 1 & 1 & 0 \\ 1 & 0 & -1 \\ 0 & -1 & -1 \end{bmatrix} \quad \begin{bmatrix} 1 & 1 & 1 \\ 0 & 0 & 0 \\ -1 & -1 & -1 \end{bmatrix} \quad \begin{bmatrix} 0 & 1 & 1 \\ -1 & 0 & 1 \\ -1 & -1 & 0 \end{bmatrix}$$

The four masks are applied independently to each pixel in the image and the output value is defined as the maximum of the absolute values of the outputs of the four masks.

(ii) Roberts (2×2) operator

$$\begin{bmatrix} 0 & -1 \\ 1 & 0 \end{bmatrix} \quad \begin{bmatrix} -1 & 0 \\ 0 & 1 \end{bmatrix}$$

The two masks are applied independently to each pixel in the image and the output value is the square root of the sum of the squared output values of the two masks.

(iii) two channel Laplacian (5×5) operator

$$\begin{bmatrix} 1 & 1 & 0 & 1 & 1 \\ 1 & 0 & -2 & 0 & 1 \\ 0 & -2 & -4 & -2 & 0 \\ 1 & 0 & -2 & 0 & 1 \\ 1 & 1 & 0 & 1 & 1 \end{bmatrix} \qquad \begin{bmatrix} 0 & 0 & 0 & 0 & 0 \\ 0 & 0 & -1 & 0 & 0 \\ 0 & -1 & -4 & -1 & 0 \\ 0 & 0 & -1 & 0 & 0 \\ 0 & 0 & 0 & 0 & 0 \end{bmatrix}$$

The two masks are applied independently to each pixel in the image and the output value is the product of the output values of the two masks.

5.4.3 Canny edge detector

In addition to the masks described in the previous section, a filter has also been tried. The Canny edge detector [Can86] was developed to satisfy the following three criteria:

1) Good detection;

2) Good localization;

3) Only one response to a single edge.

Canny found that the first derivative of a Gaussian was the best approximation to the optimum filter which does not have any simple mathematical form. This filter satisfies the detection and localization criteria. Since it is smooth, it gives only one

response to a single edge. The window Gaussian function is defined as:

$$G = \begin{cases} \exp\left\{-\frac{x^2+y^2}{2\sigma^2}\right\} & \text{if} -\frac{W}{2} \leq x, y \leq \frac{W}{2} \\ 0 & \text{otherwise,} \end{cases} \tag{5.22}$$

where the window size is $W \times W$ and σ^2 is the variance of the Gaussian function.

The optimum filter in a given direction $\mathbf{n}$ is then defined as:

$$G_{\mathbf{n}} = \frac{\partial G}{\partial \mathbf{n}}. \tag{5.23}$$

To detect the edge perfectly, $\mathbf{n}$ should be oriented normal to the direction of the edge. Although this direction is not known *a priori*, an edge point is defined to be a local maximum (in the direction $\mathbf{n}$) of the operator $G_{\mathbf{n}}$ applied to the image f. So, we have:

$$\frac{\partial G_{\mathbf{n}}}{\partial \mathbf{n}} * f = 0, \tag{5.24}$$

where $*$ denotes the convolution operator. That is:

$$\frac{\partial^2 G}{\partial \mathbf{n}^2} * f = 0, \tag{5.25}$$

which is equivalent to:

$$\frac{\partial^2}{\partial \mathbf{n}^2}(G * f) = 0, \tag{5.26}$$

due to convolution operator properties. This means that the convolution can be done first and then the zeros of the second directional derivative can be computed to locate edges.

Two parameters have to be defined for this edge detector: the width W of the filter and the variance σ^2 of the Gaussian window. Large values of σ will tend to find

edges that are more widely spaced. The ratio σ/W should be at least 1/8 so that the high frequency characteristics of the filter do not take over, and W must be an odd number to consider a symmetric neighborhood around the pixel.

Once the edges have been found, the resulting image must be thresholded to keep only the significant edges. Typically, a single threshold is applied to the gradient image. Canny objected that if the response to the edge operator oscillates around the single threshold value, some edge points will be accepted while some others from the same contour will be rejected, and broken edge contours will be obtained. To solve this problem, Canny suggested the use of two thresholds. If any part of a contour is above a high threshold, these points are immediately output, as is the entire connected segment of contour which contains the points and which lies above a low threshold. Consequently, for a contour to be broken, it must fluctuate above the high threshold and below the low threshold.

Once all the edge points have been identified, the edge image is thinned using an 8-connected edge thinning algorithm. This last image and the original image can then be fed directly into the surface interpolation algorithm developed by Yanowitz and Bruckstein.

5.4.4 Results on test images

The Yanowitz and Bruckstein method was applied to the same set of test images as used in Section 5.3 using different edge detectors. Figures 5.9, 5.11 and 5.13 show the segmentation results using mask operators, while Figures 5.10, 5.12 and 5.14 show the results using the Canny edge detector with different values for the parameters W and σ^2. It can be seen that the best results are obtained with the Canny edge detector. By best results, we mean that the objects are well extracted from the backgound. It should be noticed that the larger the variance of the Gaussian filter, the better are

the results on images containing additive Gaussian noise. These results suggest that we should apply the Yanowitz and Bruckstein method with a Canny edge detector to segment the X-ray and C-scan images of the composite materials. The execution times of the studied image segmentation methods for an X-ray image of size 80×640 are: 20s for the simple thresholding method, 3mn15s for the ICM method, 50s for the adaptive thresholding method suggested by Chow and Kaneko, and 6mn20s for the Yanowitz and Bruckstein method.

5.5 Segmentation algorithm for X-ray and C-scan images

The segmentation algorithm applied to our X-ray and C-scan images is summarized as follows:

1. Scale the image by stretching the histogram to cover the entire range of gray levels between 0 and 255;

2. Apply the Canny edge detector with $\sigma = 2$ and $W = 17$; the two threshold values are 50% and 90% of the largest magnitude value of the edge map; obtain a thinned image of edge points;

3. Apply the Yanowitz and Bruckstein algorithm for surface fitting with $\beta = 1.5$; threshold the image to obtain a binary segmented image;

4. Apply a median filter to the binary image to smooth it;

5. Find the connected components in the image by looking at the 3×3 neighborhood of each pixel [BB82]; and

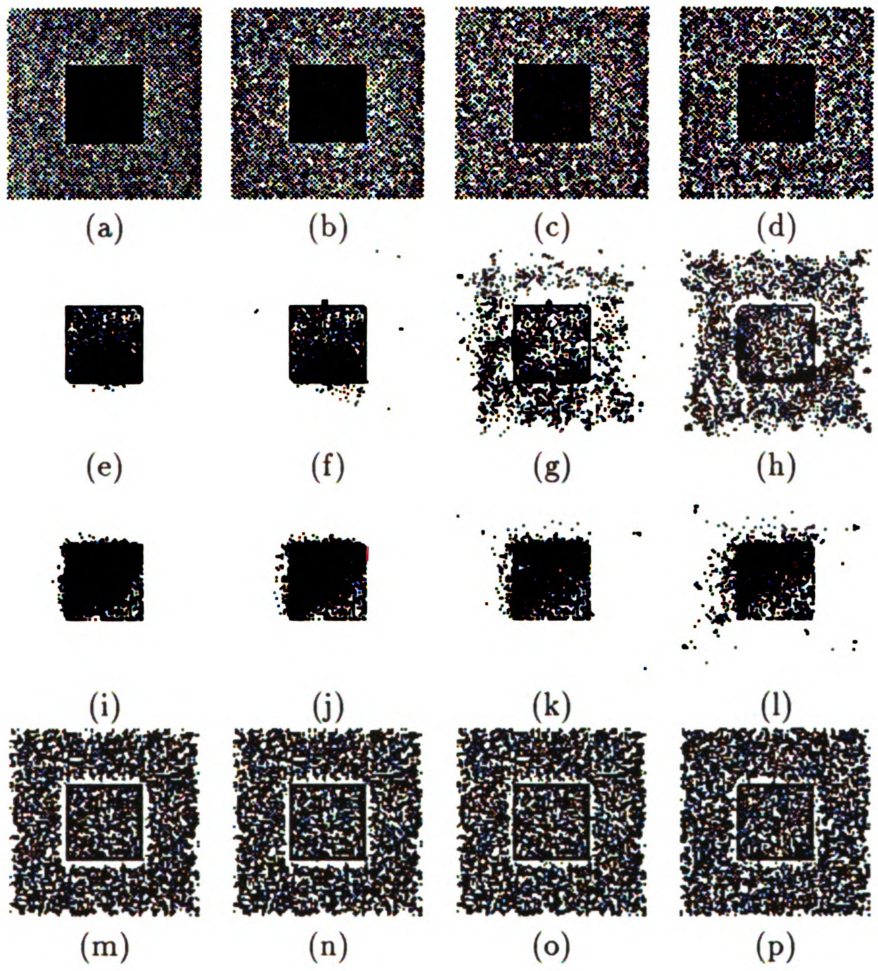

Figure 5.9: Segmentation results using the algorithm proposed by Yanowitz and Bruckstein with different masks for edge detection on noisy images of type 1. (a-d) input images, the standard deviation of the Gaussian noise process is 20 for (a), 30 for (b), 40 for (c) and 50 for (d). (e-h) Segmentation using the 3-level mask for edge detection. (i-l) Segmentation using the Roberts' mask for edge detection. (m-p) Segmentation using the two-channel Laplacian mask for edge detection.

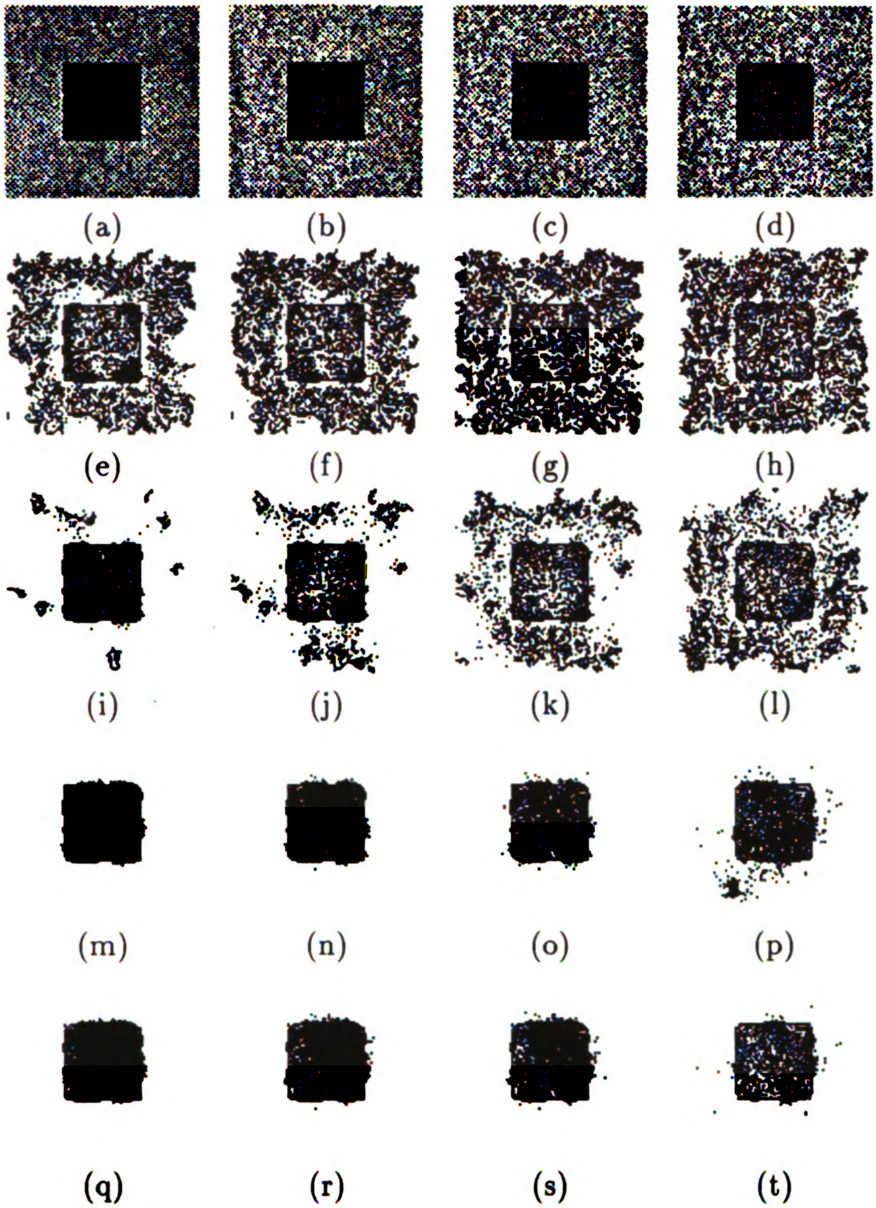

Figure 5.10: Segmentation results using the algorithm proposed by Yanowitz and Bruckstein with Canny edge detector on noisy images of type 1. (a-d) input images, the standard deviation of the Gaussian noise process is 20 for (a), 30 for (b), 40 for (c) and 50 for (d). (e-h) Segmentation with Canny's parameters $\sigma = 1.0$, $W = 9$. (i-l) Segmentation with Canny's parameters $\sigma = 1.5$, $W = 13$. (m-p) Segmentation with Canny's parameters $\sigma = 2.0$, $W = 17$. (q-t) Segmentation with Canny's parameters $\sigma = 3.0$, $W = 25$.

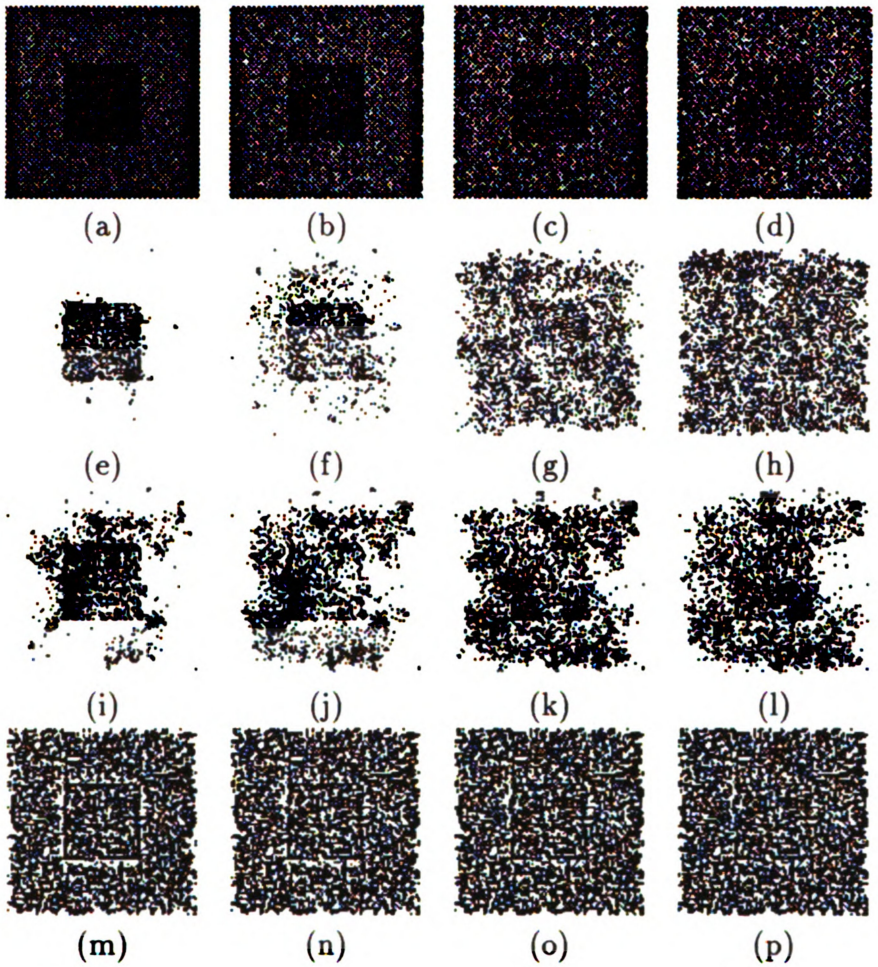

Figure 5.11: Segmentation results using the algorithm proposed by Yanowitz and Bruckstein with different masks for edge detection on noisy images of type 2. (a-d) input images, the standard deviation of the Gaussian noise process is 20 for (a), 30 for (b), 40 for (c) and 50 for (d). (e-h) Segmentation using the 3-level mask for edge detection. (i-l) Segmentation using the Roberts' mask for edge detection. (m-p) Segmentation using the two-channel Laplacian mask for edge detection.

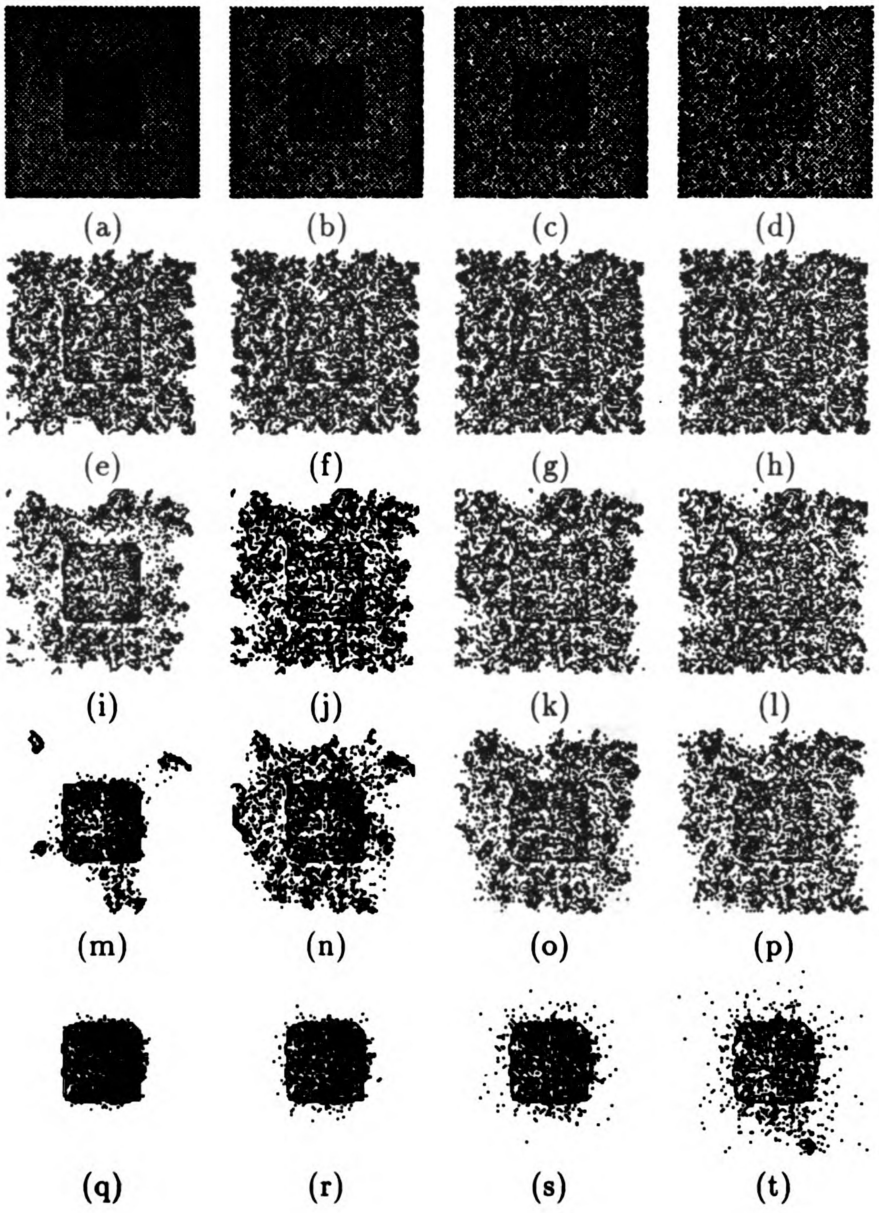

Figure 5.12: Segmentation results using the algorithm proposed by Yanowitz and Bruckstein with Canny edge detector on noisy images of type 2. (a-d) input images, the standard deviation of the Gaussian noise process is 20 for (a), 30 for (b), 40 for (c) and 50 for (d). (e-h) Segmentation with Canny's parameters $\sigma = 1.0$, $W = 9$. (i-l) Segmentation with Canny's parameters $\sigma = 1.5$, $W = 13$. (m-p) Segmentation with Canny's parameters $\sigma = 2.0$, $W = 17$. (q-t) Segmentation with Canny's parameters $\sigma = 3.0$, $W = 25$.

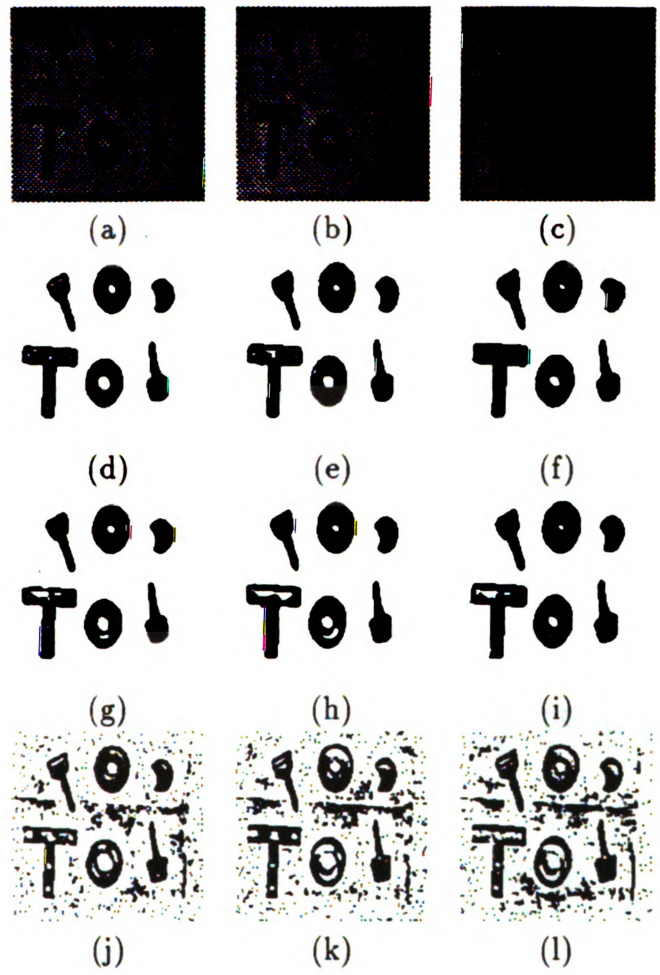

Figure 5.13: Segmentation results using the algorithm proposed by Yanowitz and Bruckstein with different masks for edge detection on nonuniformly illuminated images. (a-c) input images. (d-f) Segmentation using the 3-level mask for edge detection. (g-i) Segmentation using the Roberts mask for edge detection. (j-l) Segmentation using the two-channel Laplacian mask for edge detection.

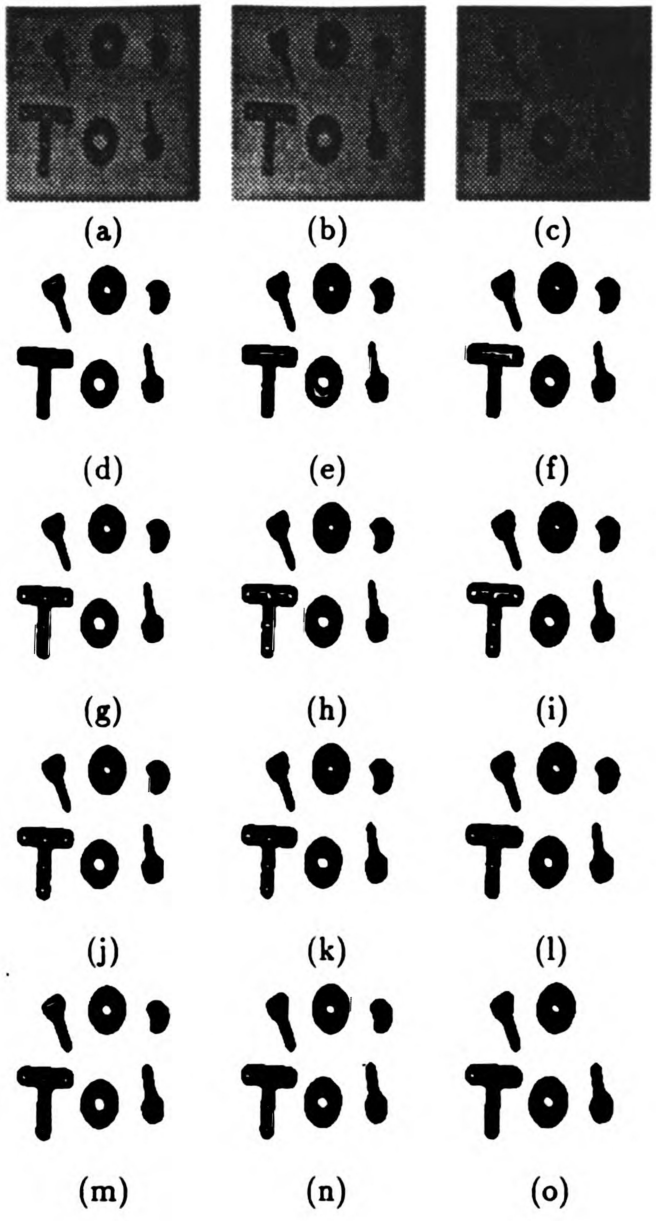

Figure 5.14: Segmentation results using the algorithm proposed by Yanowitz and Bruckstein with Canny edge detector on nonuniformly illuminated images. (a-c) input images. (d-f) Segmentation with Canny's parameters $\sigma = 1.0$, $W = 9$. (g-i) Segmentation with Canny's parameters $\sigma = 1.5$, $W = 13$. (j-l) Segmentation with Canny's parameters $\sigma = 2.0$, $W = 17$. (m-o) Segmentation with Canny's parameters $\sigma = 3.0$, $W = 25$.

6. Eliminate the small connected components in the image (less than 0.5% of the entire image).

Figure 5.15 shows the intermediate results and the final segmentation using the algorithm on a 40 × 360 X-ray image of specimen A, described in Figure 4.2, with three vertical defects. Figures 5.16, 5.17 and 5.18 show the input X-ray and C-scan images along with the segmentation results for specimens A, B, and C of Figure 4.2. In all cases, the defects are properly extracted from the background. Some spurious components which do not correspond to any defects are also extracted, but these will be discarded during the sensor fusion phase described in Chapter 6.

5.6 Summary

It was very important to find a segmentation method capable of producing an adaptative thresholding surface given the poor quality of the images obtained using either X-radiography or ultrasonic C-scan. The method proposed by Yanowitz and Bruckstein solves this kind of problem fairly well. The difficult part was finding an adequate edge detector. The Canny edge detector is becoming more and more popular and performs well enough for the given images. These two recent methods, in combination, produce a good algorithm for segmenting X-ray and C-scan images. The next chapter will present the fusion algorithm used to combine the segmented X-ray and C-scan images and the results produced by the acoustic emission experiments.

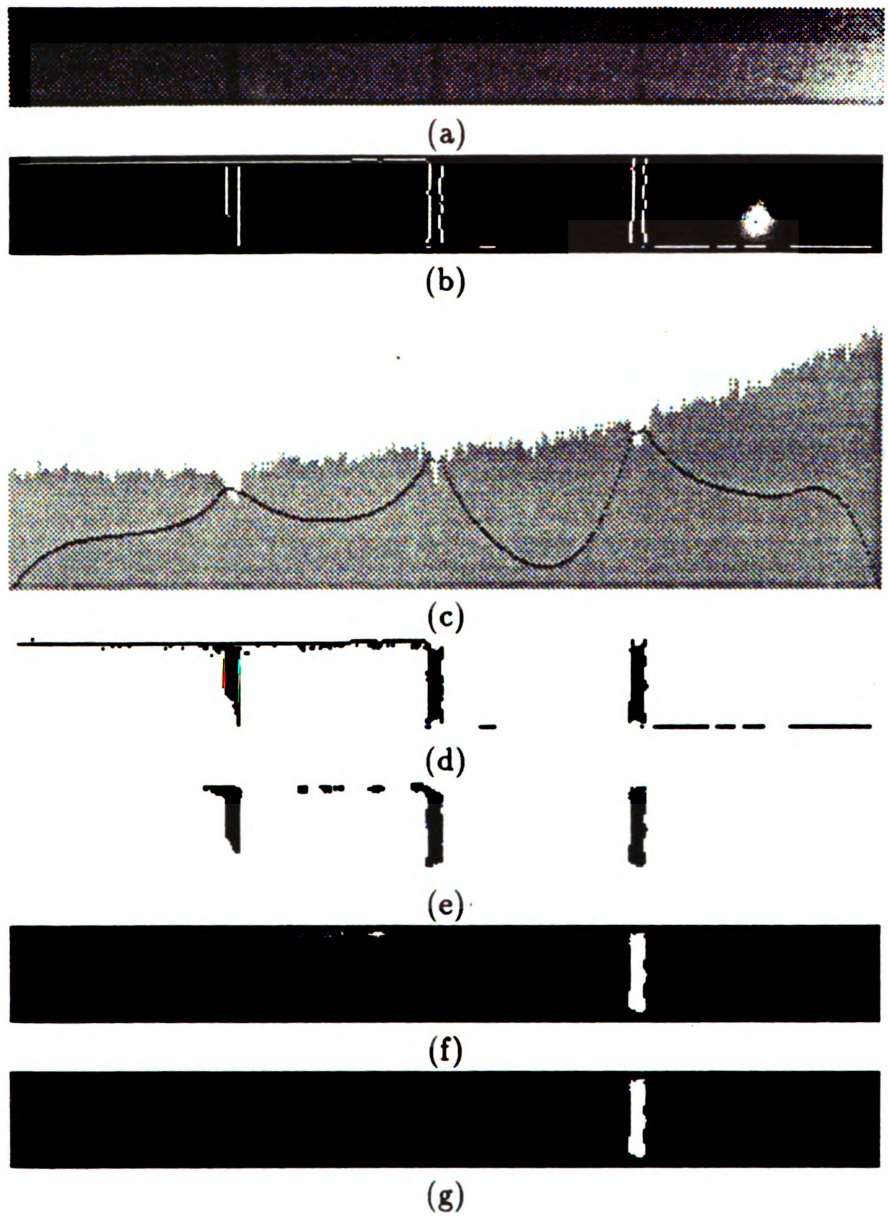

Figure 5.15: Segmentation of an X-ray image. (a) Original image. (b) Edge detection. (c) Scan line of the image along with the thresholding surface for that line. (d) Thresholding using the interpolated surface. (e) Cleared image after median filtering. (f) Connected components. (g) Final segmentation.

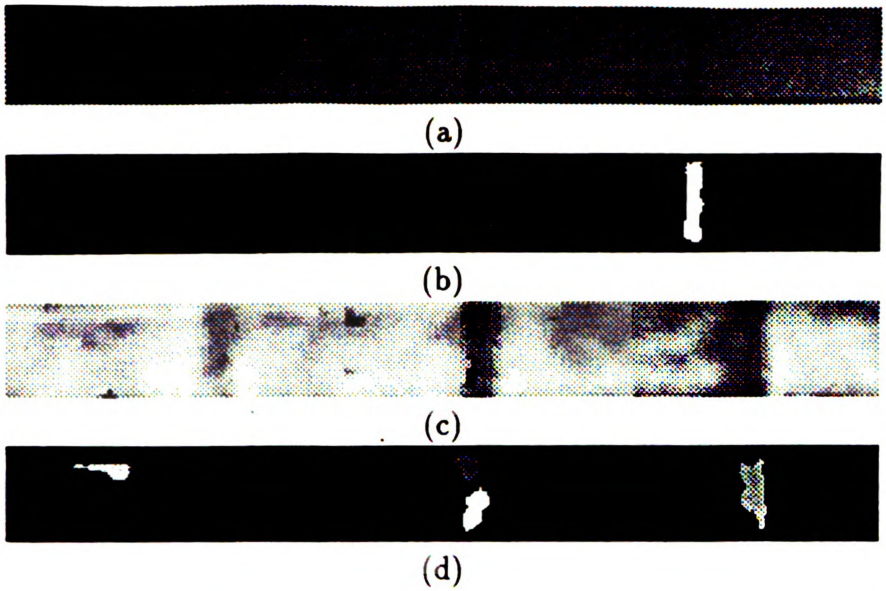

Figure 5.16: Segmentation of specimen A. (a) X-ray image. (b) Segmentation of the X-ray image. (c) C-scan image. (d) Segmentation of the C-scan image.

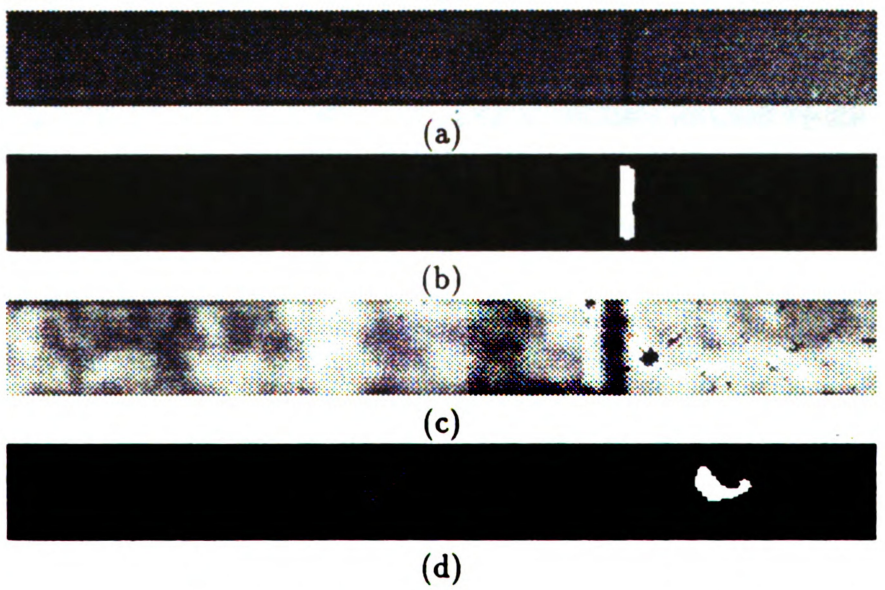

Figure 5.17: Segmentation of specimen B. (a) X-ray image. (b) Segmentation of the X-ray image. (c) C-scan image. (d) Segmentation of the C-scan image.

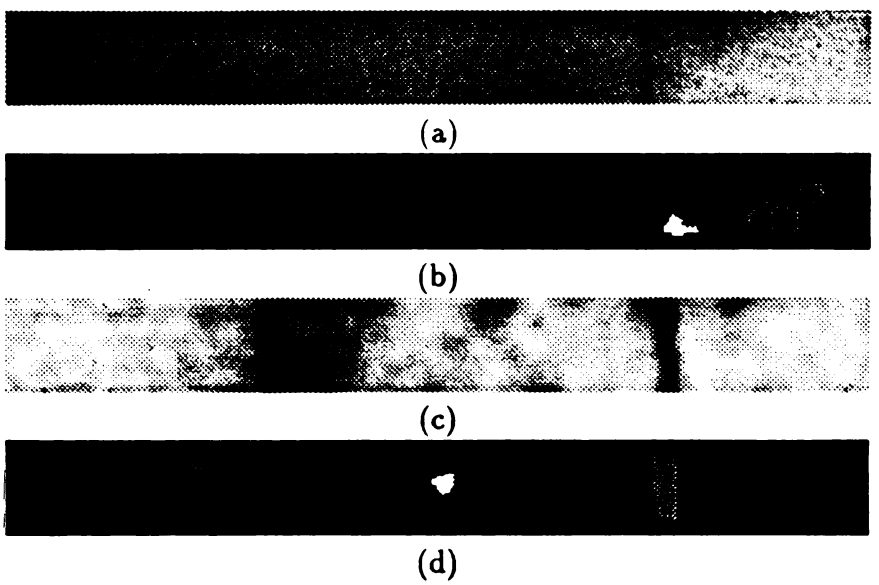

Figure 5.18: Segmentation of specimen C. (a) X-ray image. (b) Segmentation of the X-ray image. (c) C-scan image. (d) Segmentation of the C-scan image.

Chapter 6

Multi-Sensor Fusion

6.1 Introduction

As we have seen in the previous chapter, the segmentation results are good, but not perfect. In fact, some defects might not be detected by one of the techniques and some spurious components which do not correspond to any defect might appear during the segmentation process. In order to produce an accurate defect map of the specimen, we need to combine the segmented X-ray and C-scan images, and the acoustic emission location distribution histogram of events which contains peaks at the defect locations.

An algorithm was developed to fuse the information obtained from the three different sources and produce a defect map of the specimen. Before describing the algorithm used in this thesis, a review of the current techniques available in the literature will be presented.

6.2 Background

The sensor fusion problem is commonly encountered when multiple images are available for scene interpretation. Listed below are some examples of situation where fusion techniques have been used.

- Multiple images of the same object taken at different times by the same sensor. This is typically the problem in registering Landsat images to see the evolution of water areas, field areas, or urban areas;

- Multiple images of the same object taken at the same time by different sensors. This occurs, for example, when a mobile robot is equipped with a TV camera and an array of ultrasonic sensors and one wants to use both types of information to construct a map of the environment. Our sensor fusion problem is similar to this scenario.

- Multiple images of the same scene taken from two or more different vantage points. This is the situation in binocular or trinocular stereo vision.

The most difficult problem in fusion—the registration or spatial alignment of the multiple images—is present in all these instance categories. In the following, we briefly mention a few of the approaches taken by different authors to solve the registration problem.

One important application of image registration is to compute the translation, scaling and rotation transformation which will map one image to the other. Once the objects of interest have been extracted from the images, a linear transformation is derived for all possible pairs of objects in the two images. Clustering in the space of all possible transformations reveals a global transformation which matches many objects in the first image to many objects in the second image; see [BB82, SKB82].

Another important application of image registration is change detection. Here control points are extracted in the two images. Two types of attributes are used in control point matching: feature properties associated with each point, and relative distances between points. A matrix whose row elements are objects (control points) from the first image and whose column elements are objects from the second image contains information on how similar (or dissimilar) the two objects from the two images are. Usually, a relaxation method is used to reduce to zero the entries corresponding to the pairs of objects that are different and to increase to 1 the entries corresponding to similar object pairs. Ranade and Rosenfeld [RR80] only used the relative distance between control points. Wang et al. [WSYR83] extented Ranade and Rosenfeld method to use feature information associated with each control point. Ton and Jain [TJ89] used the centers of the interesting objects as the control points and the size of the object as the feature. In the following, we will describe the sensor fusion method that has been used in this research.

6.3 Fusion algorithm

Our purpose was to find a simple algorithm which would combine information from the segmented X-ray image, C-scan image and the location distribution histogram of events. The segmentation of the first two images gives us a list of connected components in an image, while the last one provides information about the location of the defect along the length of the specimen. Usually, connected components are associated with defective regions, but as pointed out earlier, a few noisy connected components also appear in the segmentation results. Further, a defective region is often split up into several connected components. Our purpose in the fusion of X-ray and C-scan imges is to remove some of these noisy connected components.

Shape properties of connected components are useful in distinguishing them. Many different shape properties can be computed as suggested in [BB82]: area, eccentricity, compactness, etc. We have chosen to use 5 features to characterize each of the connected components by their location and shape:

f_1: the x position of the center of the connected component;

f_2: the y position of the center of the connected component;

f_3: the ratio of the smallest eigenvalue to the largest eigenvalue;

f_4: the orientation of the eigenvector corresponding to the largest eigenvalue;

f_5: the size of the connected component in pixels compared to the size of the image.

The eigenvalues and eigenvectors provide a good description of the shape of an object. They are computed as follows. Each point P_i in the connected component has two coordinates x_i and y_i. We can compute the means, variances and covariance of those coordinates in the following manner:

$$m_x = \frac{\sum_{i=1}^{N} x_i}{N}, \qquad m_y = \frac{\sum_{i=1}^{N} y_i}{N}, \tag{6.1}$$

$$\sigma_x^2 = \frac{\sum_{i=1}^{N}(x_i - m_x)^2}{N}, \quad \sigma_y^2 = \frac{\sum_{i=1}^{N}(y_i - m_y)^2}{N}, \quad \sigma_{xy} = \frac{\sum_{i=1}^{N}(x_i - m_x)(y_i - m_y)}{N}. \tag{6.2}$$

where N is the number of pixels in the connected component. Note that m_x and m_y are the first two features associated with a connected component. The eigenvalues of the covariance matrix are obtained by solving:

$$|C - \lambda I| = 0 \quad \text{where} \quad C = \begin{bmatrix} \sigma_x^2 & \sigma_{xy} \\ \sigma_{xy} & \sigma_y^2 \end{bmatrix} \tag{6.3}$$

$$\text{or} \quad \lambda^2 - (\sigma_x^2 + \sigma_y^2)\lambda - \sigma_{xy}^2 + \sigma_x^2\sigma_y^2 = 0. \tag{6.4}$$

This equation has 2 eigenvalue solutions λ_1 and λ_2, $\lambda_1 \leq \lambda_2$. The ratio λ_1/λ_2 defines the third feature. The eigenvectors are defined as: $CV_1 = \lambda_1 V_1$ and $CV_2 = \lambda_2 V_2$. The orientation of V_2 is the fourth feature. If the object is approximately circular, the ratio of the two eigenvalues is close to 1 and the orientation of the main eigenvector is not meaningful. So, the fourth feature is set to 0. All the features are scaled to fall between 0 and 100. A dissimilarity index is computed for each pair of connected components (C_i, C_j), where C_i is from the X-ray image and C_j is from the C-scan image as follows:

$$d_{ij} = 2(f_1^i - f_1^j)^2 + 2(f_2^i - f_2^j)^2 + (f_3^i - f_3^j)^2 + 2(f_4^i - f_4^j)^2 + (f_5^i - f_1^5)^2. \tag{6.5}$$

Note that more importance is given to the position and orientation of the connected component. The small entries in the dissimilarity matrix $[d_{ij}]$ correspond to connected components which are similar in both the images. Of course, it is impossible to obtain these features from the acoustic emission graph. Thus, we only consider the x position of the peaks in the graph (these peaks correspond to defects in the specimen).

Since it is not possible with the software available on the acoustic emission system to access the raw data of the histogram, we cannot simply run an algorithm for maxima detection. Thus, the peaks are determined by looking at the graph and the x position of the defect, scaled between 0 and 100, is manually entered into the fusion program as a vector M_i. The fusion algorithm has three main steps.

- Step 1: Look for small entries in the dissimilarity matrix.

  - Find the smallest entry d_{min} at position (k, l) in the matrix;

- Compute the acceptance criterion α:

$$\alpha = \frac{4(1 - \frac{d_{min}}{d_{max}}) + \frac{\sum_{i \neq k}(1 - \frac{d_{min}}{d_{il}})}{r-1} + \frac{\sum_{j \neq l}(1 - \frac{d_{min}}{d_{kj}})}{c-1} + 4\frac{(1-a)+(1-b)}{2}}{10}, \tag{6.6}$$

where r and c are the number of rows and columns in the matrix, and d_{max} is the biggest entry in the matrix; a and b are defined as:

$$a = \left| \frac{f_1^k - M_i}{M_i} \right| \quad \text{and} \quad b = \left| \frac{f_1^l - M_i}{M_i} \right|, \tag{6.7}$$

and the product ab is minimum among all the M_i's.

Note that for the connected components to be considered as defects, the smallest entry in the matrix must be much smaller than the biggest entry, and smaller than the other entries on the same row and same column. Also, this must be confirmed by a peak in the acoustic emission graph.

- If $\alpha \leq 0.85$, then accept the two connected components and the associated peak as a defect, delete them from further consideration, and reduce the size of the dissimilarity matrix by suppressing row k and column l. Go back to step 1;

- Else, go to step 2.

• Step 2:

- Compute

$$\beta = \min_{i,j} \left| \frac{f_1^i - M_j}{M_j} \right|, \tag{6.8}$$

for all the connected components C_i in the X-ray image and all the peaks M_j in the acoustic emission graph that have not been considered yet.

- If $\beta < 0.2$, then accept the connected component and the associated peak as a defect and delete them from further consideration; go back to step 2.

- Else, go to step 3.

• Step 3:

- Compute

$$\gamma = \min_{i,j} \left| \frac{f_1^i - M_j}{M_j} \right|, \tag{6.9}$$

for all the connected components C_i in the C-scan image and all the peaks M_j in the acoustic emission graph that have not been considered yet.

- If $\gamma < 0.2$, then accept the connected component and the associated peak as a defect and delete them from further consideration; go back to step 3.

- Else, terminate the algorithm.

Once the defects have been found, a defect map of the specimen is constructed by drawing an ellipse around each defect. The center of the ellipse is the average of the positions of the two connected components and of the peak in the acoustic emission graph corresponding to the defect. The axes of the ellipse are determined by the eigenvalues and eigenvectors of the connected components. Results of this method on specimens A, B, and C are given in the following section.

6.4 Results of the fusion algorithm

This method has been tested on the segmented X-ray and C-scan images and acoustic emission graphs obtained for specimens A, B, and C of Figure 4.2. The results are presented in this section.

Table 6.1: Feature values for the connected components in the segmented X-ray image of specimen A.

object#	f_1	f_2	f_3	f_4	f_5
1	52.87	44.05	5.87	96.55	1.60
2	27.46	31.70	10.74	93.59	1.37
3	78.55	47.55	3.42	99.60	1.46

Table 6.2: Feature values for the connected components in the segmented C-scan image of specimen A.

object#	f_1	f_2	f_3	f_4	f_5
1	24.08	41.82	21.68	96.40	2.61
2	52.89	21.12	41.77	84.61	0.52
3	85.64	45.60	12.24	96.32	1.46
4	11.59	22.79	8.48	55.09	0.65
5	53.66	64.71	11.77	10.28	0.85

6.4.1 Specimen A

Figure 6.1 presents the results obtained for specimen A which contains three vertical defects. It can be seen in Figure 6.1(a) that the acoustic emission graph presents three peaks corresponding to the three defects, and the positions of the peaks are at 25%, 50%, and 75% of the length of the specimen. The X-ray image has been segmented and contains 3 connected components, while the segmented C-scan image contains 5 connected components as can be seen in Figures 6.1(b) and (c). Tables 6.1 and 6.2 show the feature values associated with each connected component for the X-ray image and the C-scan image, respectively. The connected components are numbered in the order in which the connected component algorithm finds them.

Once the features have been computed and the positions of the peaks have been determined, the matching algorithm can start looking for possible defects that are

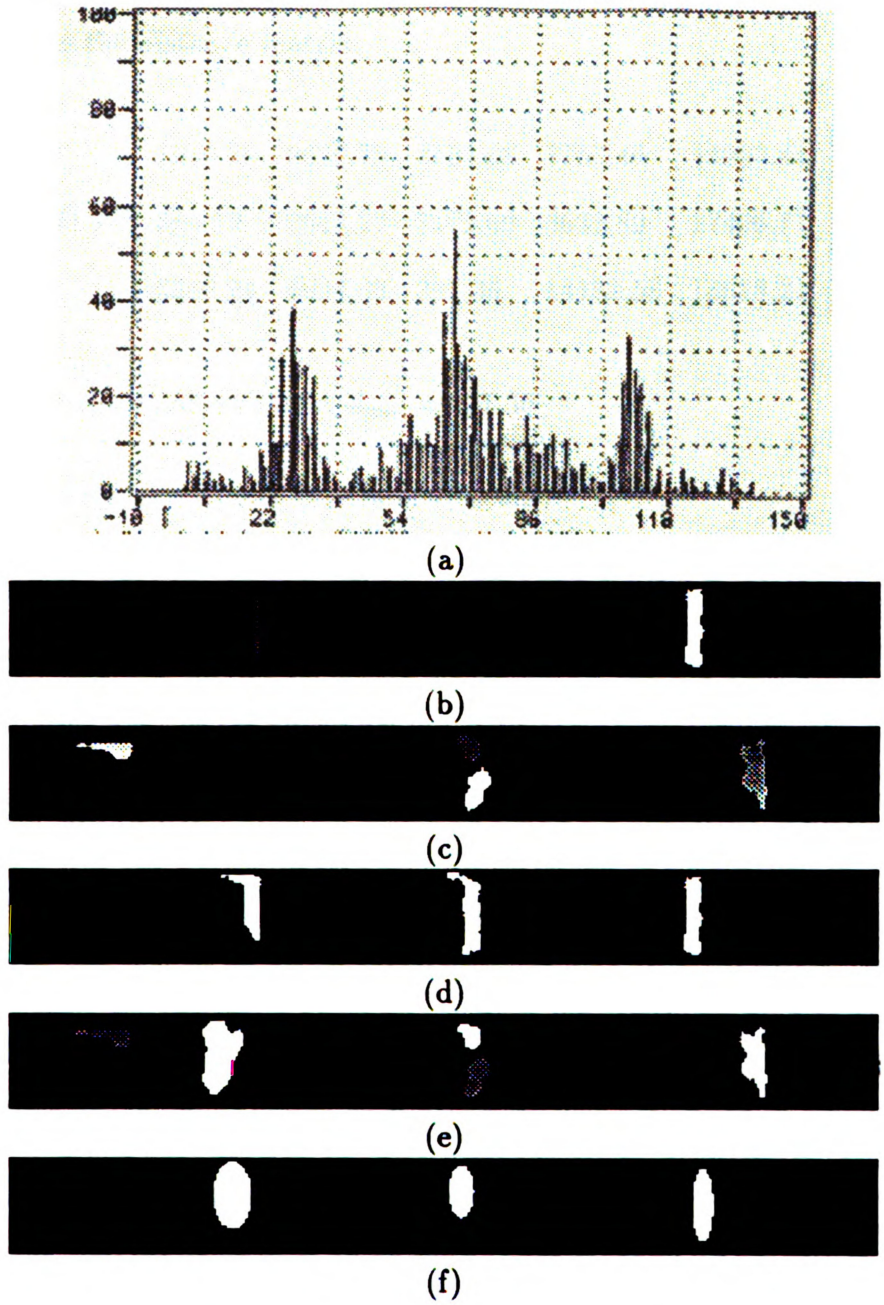

Figure 6.1: Defect map of specimen A. (a) Acoustic emission graph. (b) Segmented X-ray image. (c) Segmented C-scan image. (d) Extraction of the defects in the X-ray image. (e) Extraction of the defects in the C-scan image. (f) Defect map.

revealed by at least two of the three methods. The successive steps of the algorithm in this case are:

- Compute the distance matrix:

$$D = \begin{bmatrix} 1919.38 & 2626.70 & 2192.68 & 7757.46 & 15903.44 \\ 364.52 & 2642.77 & 7172.69 & 3632.89 & 17496.71 \\ 6356.24 & 4634.65 & 207.36 & 14182.58 & 18018.21 \end{bmatrix} \tag{6.10}$$

- Consider the smallest entry: $d_{min} = 207.36$

- Compute the acceptance criterion: $\alpha = 0.95$

- Accept the defect corresponding to object#3 in the X-ray image, object#3 in the C-scan image and peak#3 in the acoustic emission graph. This is the rightmost defect in the specimen.

- Reduce the matrix:

$$D = \begin{bmatrix} 1919.38 & 2626.70 & 7757.46 & 15903.44 \\ 364.52 & 2642.77 & 3632.89 & 17496.71 \end{bmatrix} \tag{6.11}$$

- Consider the smallest entry: $d_{min} = 364.52$

- Compute the acceptance criterion: $\alpha = 0.94$

- Accept the defect corresponding to object#2 in the X-ray image, object#1 in the C-scan image and peak#1 in the acoustic emission graph. This is the leftmost defect in the specimen.

- Reduce the matrix:

$$D = \begin{bmatrix} 2626.70 & 7757.46 & 15903.44 \end{bmatrix} \tag{6.12}$$

- Consider the smallest entry: $d_{min} = 2626.70$

- Compute the acceptance criterion: $\alpha = 0.87$

- Accept the defect corresponding to object#1 in the X-ray image, object#2 in the C-scan image and peak#2 in the acoustic emission graph. This is the middle defect in the specimen. The object number depends on the position of d_{min} in the original dissimilarity matrix.

- Stop the algorithm here, since no more peaks in the acoustic emission graph and no more objects in the X-ray image remain to be considered.

Thus, three defects have been found in this specimen, and they have been extracted from each of the segmented images. Figures 6.1(d) and (e) show in white the objects that have been extracted as defects in the X-ray and C-scan images, respectively. The other objects, which are spurious components due to imperfect segmentation, are shown in gray. The final defect map of the specimen is shown in Figure 6.1(f) which corresponds to the knowledge we had of the specimen. Even when the segmentation results are not perfect, the fusion algorithm is able to extract the defects from all the objects and compute an accurate map of the specimen.

6.4.2 Specimen B

The results for specimen B are presented in Figure 6.2. In this case, the acoustic emission graph presents one peak. The large number of events on the far right of

the image is due to vibration from the pulling side of the UTS system. This second peak cannot be counted as a peak coming from a defect. The segmented X-ray image contains one object and the segmented C-scan image contains three objects. When the matching algorithm runs, the distance matrix is:

$$D = \begin{bmatrix} 70.47 & 12221.84 & 4216.93 \end{bmatrix} \tag{6.13}$$

The acceptance coefficient α for $d_{min} = 70.47$ is 0.97, and the defect is recognized as being the object in the X-ray image, the middle object in the C-scan image and the only peak in the acoustic emission graph. The defect map constructed by the algorithm is accurate, as can be seen in Figure 6.2.

6.4.3 Specimen C

The results for the fusion of the two images and the acoustic emission graph of specimen C are presented in Figure 6.3. The acoustic emission graph presents one peak at 75%, the segmented X-ray image contains 3 objects, and the segmented C-scan image contains five objects.

The distance matrix is:

$$D = \begin{bmatrix} 14237.08 & 15126.60 & 13190.50 & 58.98 & 25575.96 \\ 14504.90 & 17866.51 & 11910.04 & 7748.03 & 9435.68 \\ 15049.63 & 16895.81 & 13176.86 & 5259.31 & 12247.21 \end{bmatrix} \tag{6.14}$$

The smallest entry $d_{min} = 58.98$ is considered and accepted as a defect with $\alpha = 0.99$. This defect corresponds to the only peak in the acoustic emission graph, the leftmost object in the X-ray image and the rightmost object in the C-scan image. Then the dissimilarity matrix is reduced and the next smallest entry $d_{min} = 9435.68$

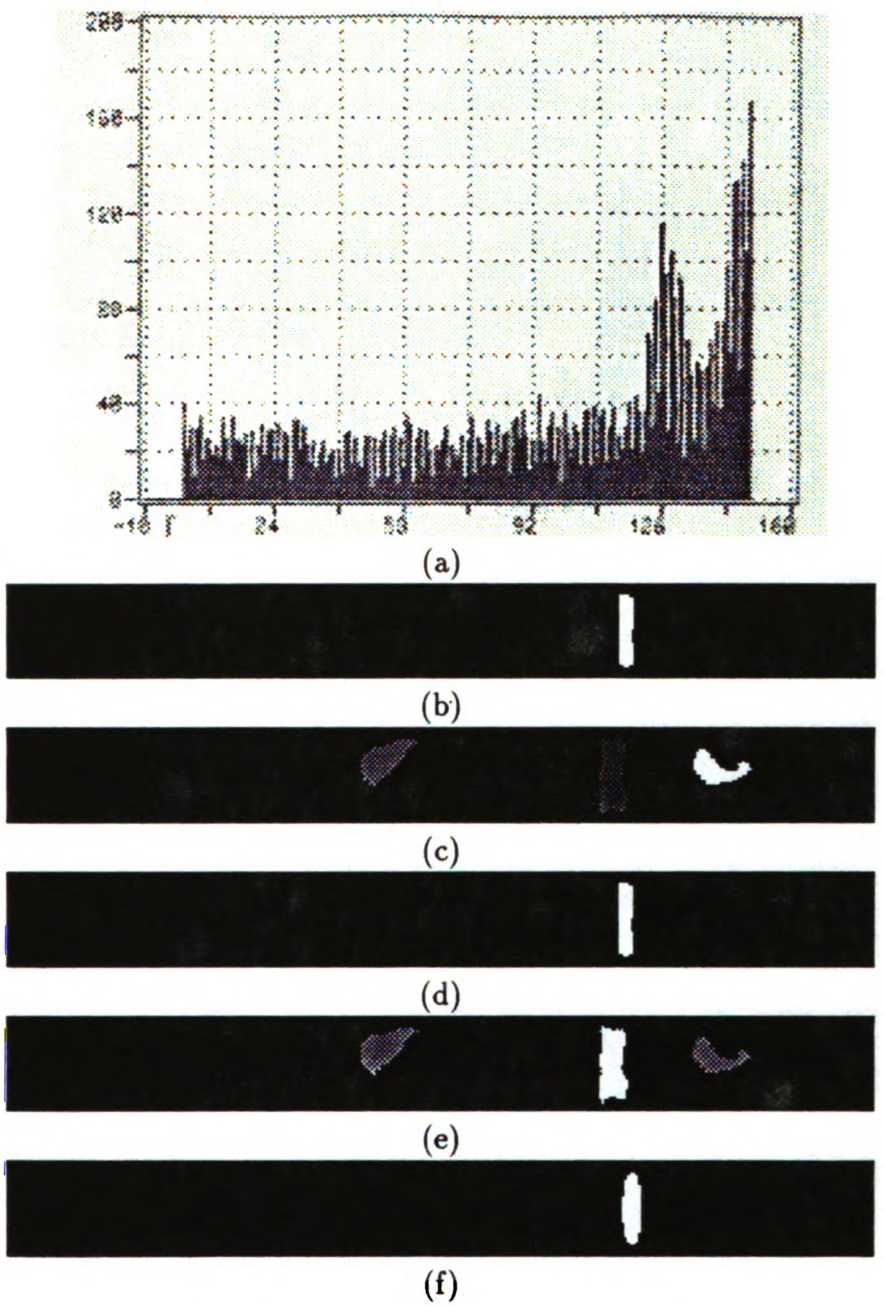

Figure 6.2: Defect map of specimen B. (a) Acoustic emission graph. (b) Segmented X-ray image. (c) Segmented C-scan image. (d) Extraction of the defects in the X-ray image. (e) Extraction of the defects in the C-scan image. (f) Defect map.

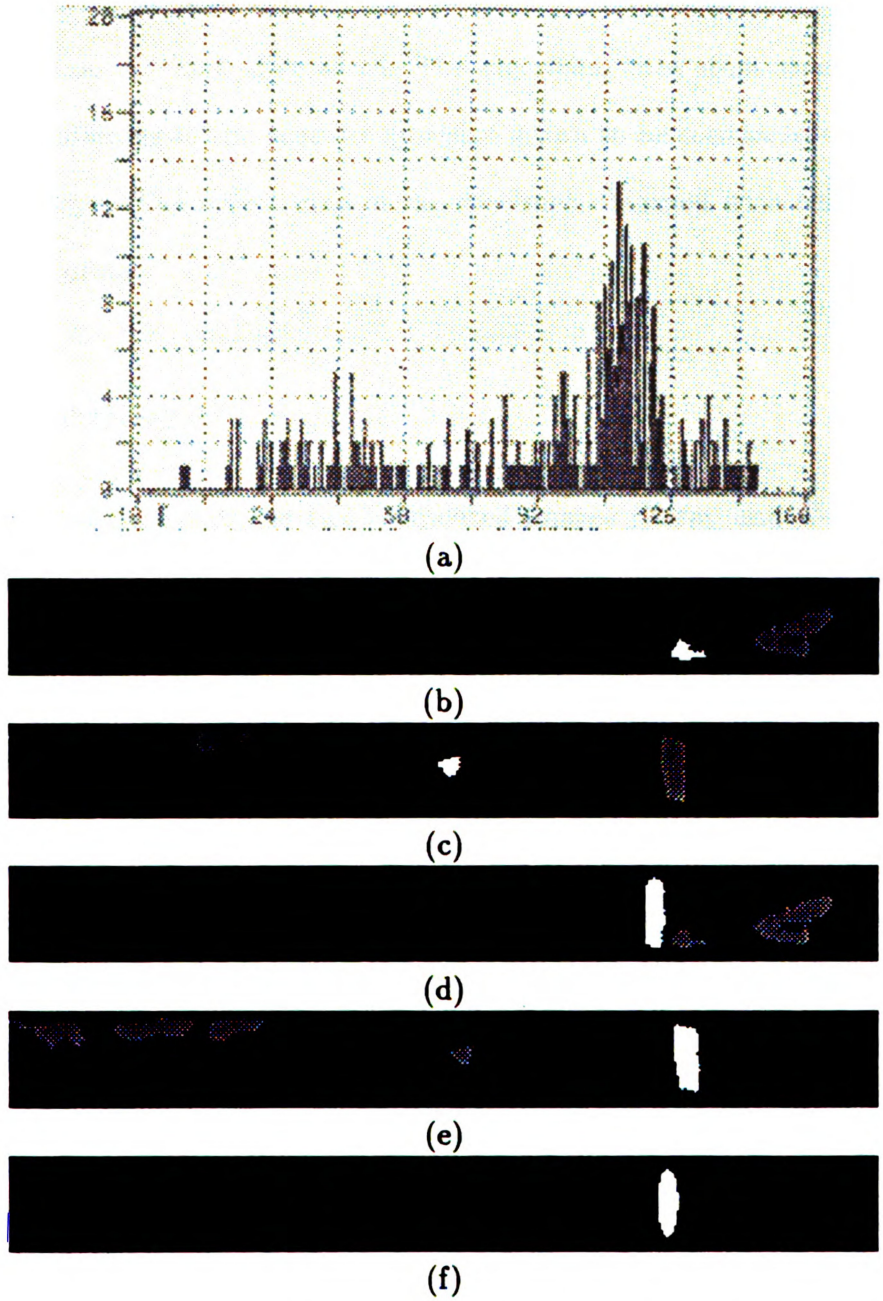

Figure 6.3: Defect map of specimen C. (a) Acoustic emission graph. (b) Segmented X-ray image. (c) Segmented C-scan image. (d) Extraction of the defects in the X-ray image. (e) Extraction of the defects in the C-scan image. (f) Defect map.

gives an $\alpha = 0.41$ and is not accepted as corresponding to a defect. This is mainly due to the fact that the entry is not small enough compared to the other entries, the two objects (the rightmost object in the X-ray image and the middle object in the C-scan image) do not look alike at all. The algorithm then stops since there are no more peaks remaining in the acoustic emission graph to be compared to an object in one of the images. The defect map of the specimen obtained with this algorithm is once again accurate.

6.5 Summary

A method for fusion of the two segmented images (X-ray and C-scan) and the location distribution histogram of events graph in acoustic emission has been developed. This fusion scheme generates an accurate defect map of the specimen from imperfectly segmented images. We have seen that this scheme works very well on the three specimens A, B, and C. In all the three cases, the results are perfect and the defect map is accurate. The main advantage of the method is its simplicity. It does not use any relaxation or iterative processes, it simply compares objects based on five easily computed features. The next chapter will present the acoustic emission, segmentation, and fusion results on the set of test specimens

Chapter 7

Experimental Results

7.1 Introduction

We have presented two algorithms in the previous chapters: a segmentation algorithm to extract objects from the X-ray and C-scan images of the specimen, and a fusion algorithm to distinguish real defects from spurious components in the two segmented images and to construct an accurate defect map of the specimen.

In this chapter we will present the results obtained for the set of test specimens of Figure 4.1, which contains different types of defects, namely, teflon inserts, cut plies and holes. We will see how the segmentation and the fusion algorithms perform on these specimens. We will also draw conclusions about the ability of each method to find particular defects.

7.2 General remarks

As described in Chapter 4, 14 test specimens have been fabricated. Eight of them, the F specimens (ND1, ND2, CF, CHF, CTF, CTHF, TF, and THF) have been pulled until failure in order to determine the maximum load that they can handle. Table 7.1

Table 7.1: Maximum load for the F specimens.

Specimen	Failure stress (psi)	Time (min:sec)	Extension (in)
ND1	356	35:37	0.3562
ND2	370	38:51	0.3885
CF	311	21:53	0.3049
CHF	194	12:06	0.2010
CTF	290	22:30	0.3107
CTHF	199	13:21	0.2038
TF	347	33:35	0.3367
THF	170	12:35	0.1911

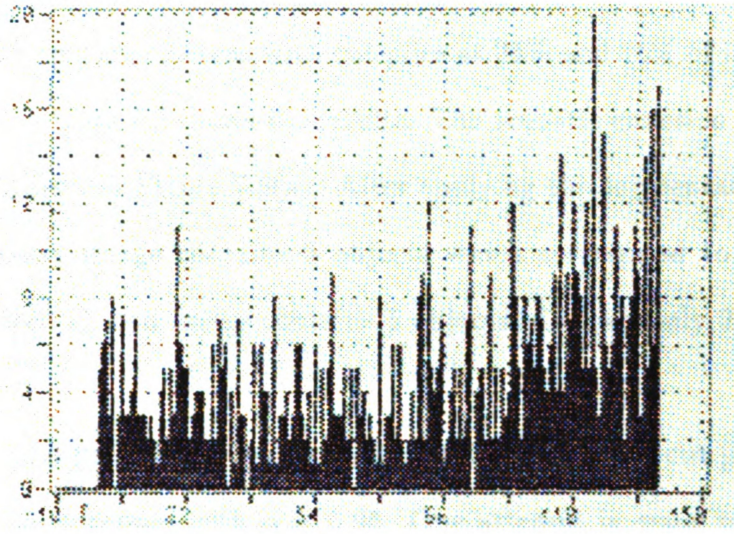

Figure 7.1: Acoustic emission graph of specimen ND2.

presents the load, time and extension at which each of these specimens failed.

From this table, we can see that a hole weakens the specimen substantially, about 40% of its strength (CHF,CTHF,THF). The cut plies weaken it by 15% of its strength (CF,CTF), while the teflon inserts barely affect the strength of the specimen (TF). Figure 7.1 shows the location distribution histogram of events obtained for specimen ND2. We can see that emission occurs everywhere along the specimen, so that no defect can be detected.

The six other specimens, the S specimens (CHS, CS, CTHS, CTS, THS, and TS)

have been X-rayed and C-scanned, pulled to 1/2 of the maximum load that they could handle, and X-rayed and C-scanned again. Results for these six specimens will be presented in the following sections. The second X-radiograph and C-scan of the specimens were not different from the first ones. This shows that pulling the specimen to 1/2 of its maximum load did not affect it, but still allows good detection of the defects as will be seen later in this chapter.

7.3 Specimen CHS

Specimen CHS contains 2 areas with cut plies at 25% and 75% of its length and a hole in its middle. Figure 7.2 shows the results. The acoustic emission graph contains 3 peaks as can be seen in Figure 7.2(a). After applying the segmentation algorithm, the segmented X-ray image contains 3 objects which correspond to the 3 defects, while the segmented C-scan image contains 5 objects of which only 2 correspond to real defects.

The hole is found first and accepted with $\alpha = 0.93$, then the cut plies on the left of the specimen are accepted with $\alpha = 0.95$. One attempt is made to associate the second object from the right in the C-scan image with the rightmost object in the X-ray image and the rightmost peak in the acoustic emission graph, but this hypothesis is rejected with $\alpha = 0.69$. Then, the rightmost object in the X-ray image and the rightmost peak in the acoustic emission graph is accepted as a defect with $\gamma = 0.05$. An accurate defect map of this specimen is obtained after finding 3 defects. In this case, the segmented X-ray image was perfect and the segmented C-scan image did not really add anything.

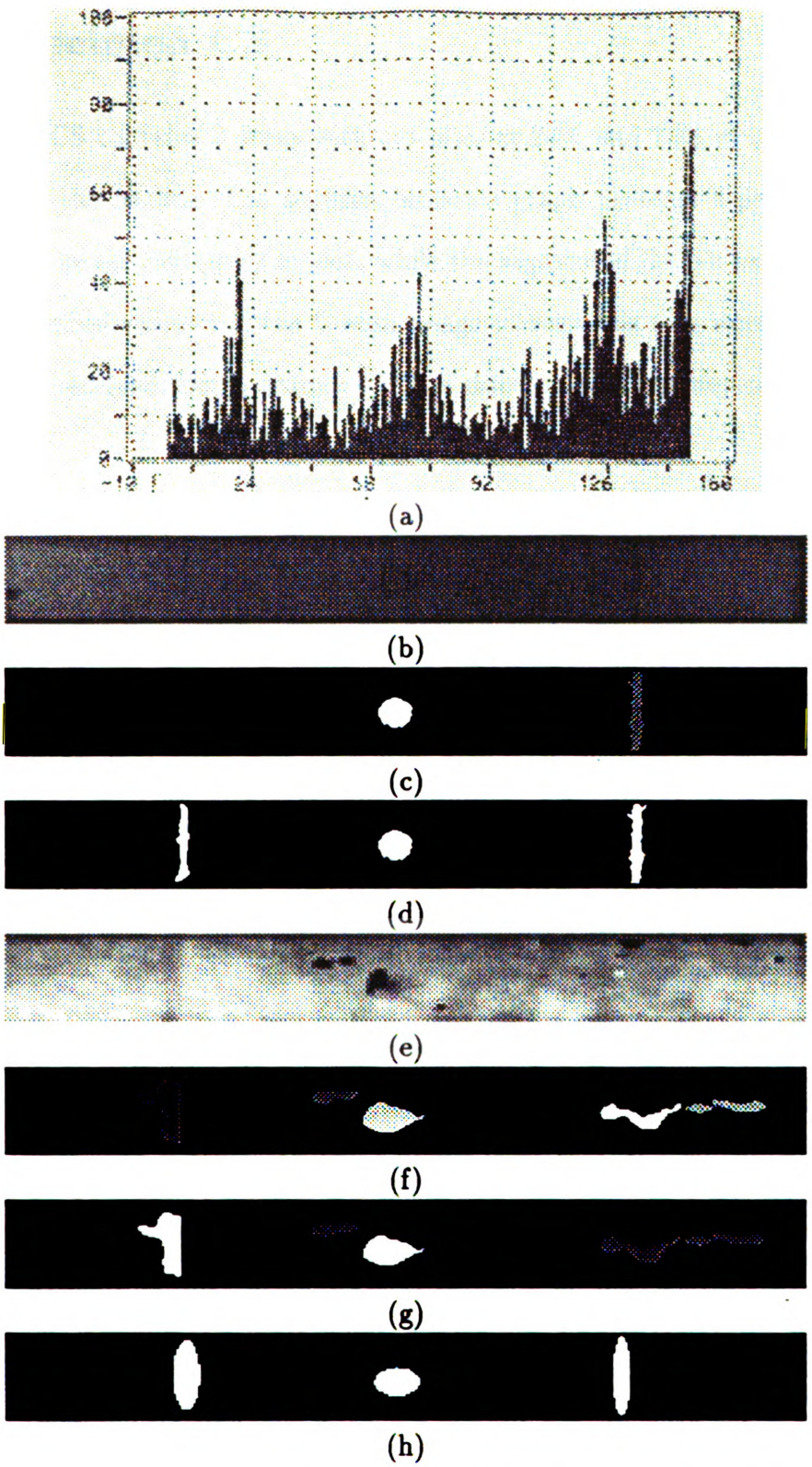

Figure 7.2: Defect map of specimen CHS. (a) Acoustic emission graph. (b) X-ray image. (c) Segmented X-ray image. (d) Extracted defects in the X-ray image. (e) C-scan image. (f) Segmented C-scan image. (g) Extracted defects in the C-scan image. (g) Defect map of the specimen.

7.4 Specimen CS

Specimen CS contains 2 areas with cut plies at 25% and 75% of its length. Figure 7.3 shows the results. The acoustic emission graph presents 2 peaks. The segmented X-ray image contains 2 objects while the segmented C-scan image contains 3 objects. The middle object in the C-scan image corresponds to a sensor error where no signal was received during scanning. This third object does not correspond to a defect at all.

Here, the X-ray image is perfect and the two defects are obtained by just looking at both segmented images. The defects are confirmed by the two peaks in the acoustic emission graph. Here, again, the C-scan image does not add anything but a confirmation of the perfectly segmented X-ray image.

7.5 Specimen CTHS

Specimen CTHS contains an area of cut plies at 25% of its length, a hole at 50% of its length and a teflon insert at 75% of its length. Figure 7.4 shows the results. The acoustic emission graph presents three peaks. The segmented X-ray image contains 2 objects which correspond to the cut plies and the hole, while the segmented C-scan image contains 6 objects.

First, the hole is found and accepted with $\alpha = 0.98$; then, the cut plies are found and accepted with $\alpha = 0.97$. All the objects in the X-ray image have been considered, so only the C-scan image and the acoustic emission graph are considered further. The teflon insert is found and accepted with $\beta = 0.02$. The algorithm stops since all the peaks in the acoustic emission graph have now been considered. Once again, an accurate map of the specimen is obtained. In this case, we see that the C-scan image was very useful since the teflon insert was not revealed by the X-radiography, but only

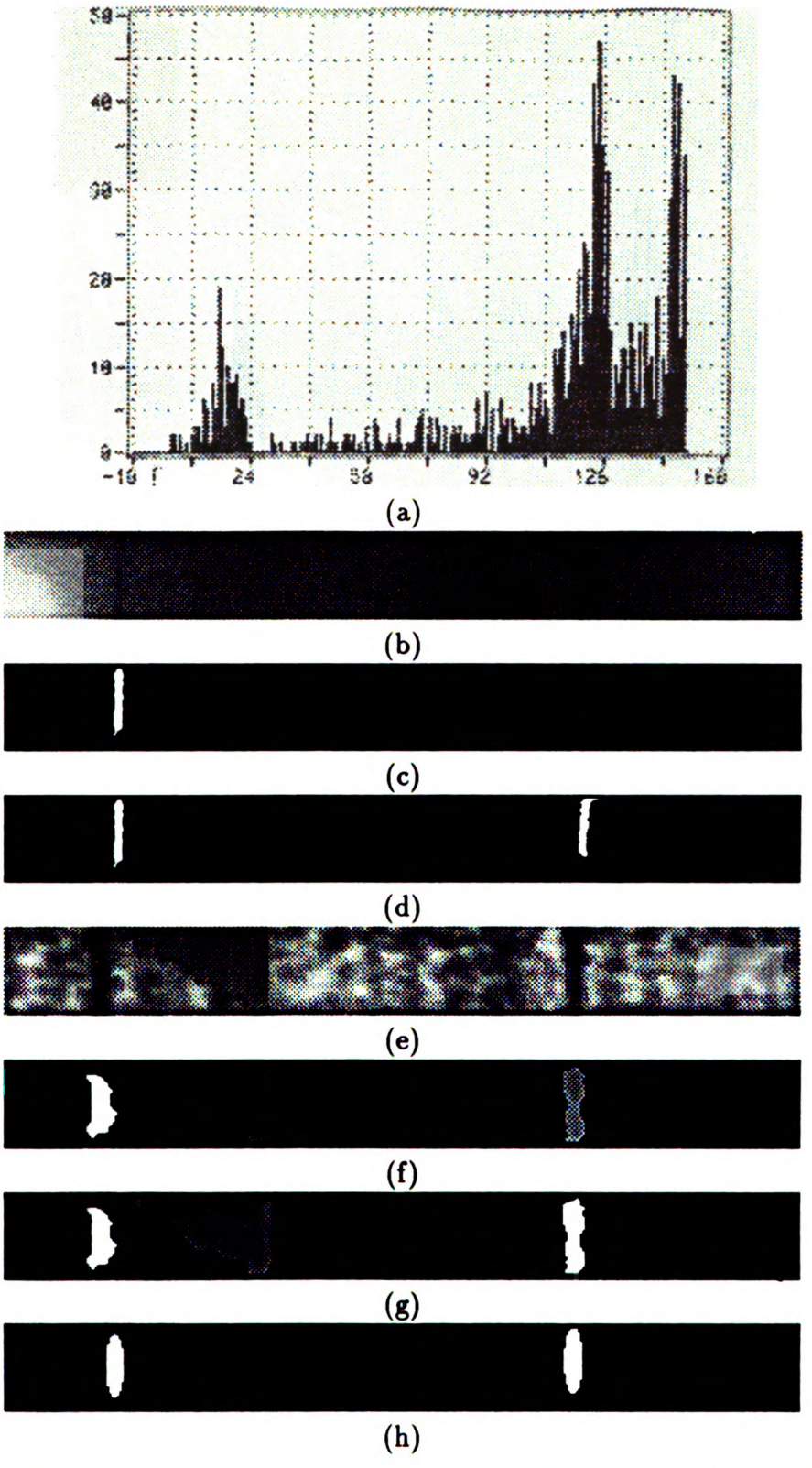

Figure 7.3: Defect map of specimen CS. (a) Acoustic emission graph. (b) X-ray image. (c) Segmented X-ray image. (d) Extracted defects in the X-ray image. (e) C-scan image. (f) Segmented C-scan image. (g) Extracted defects in the C-scan image. (g) Defect map of the specimen.

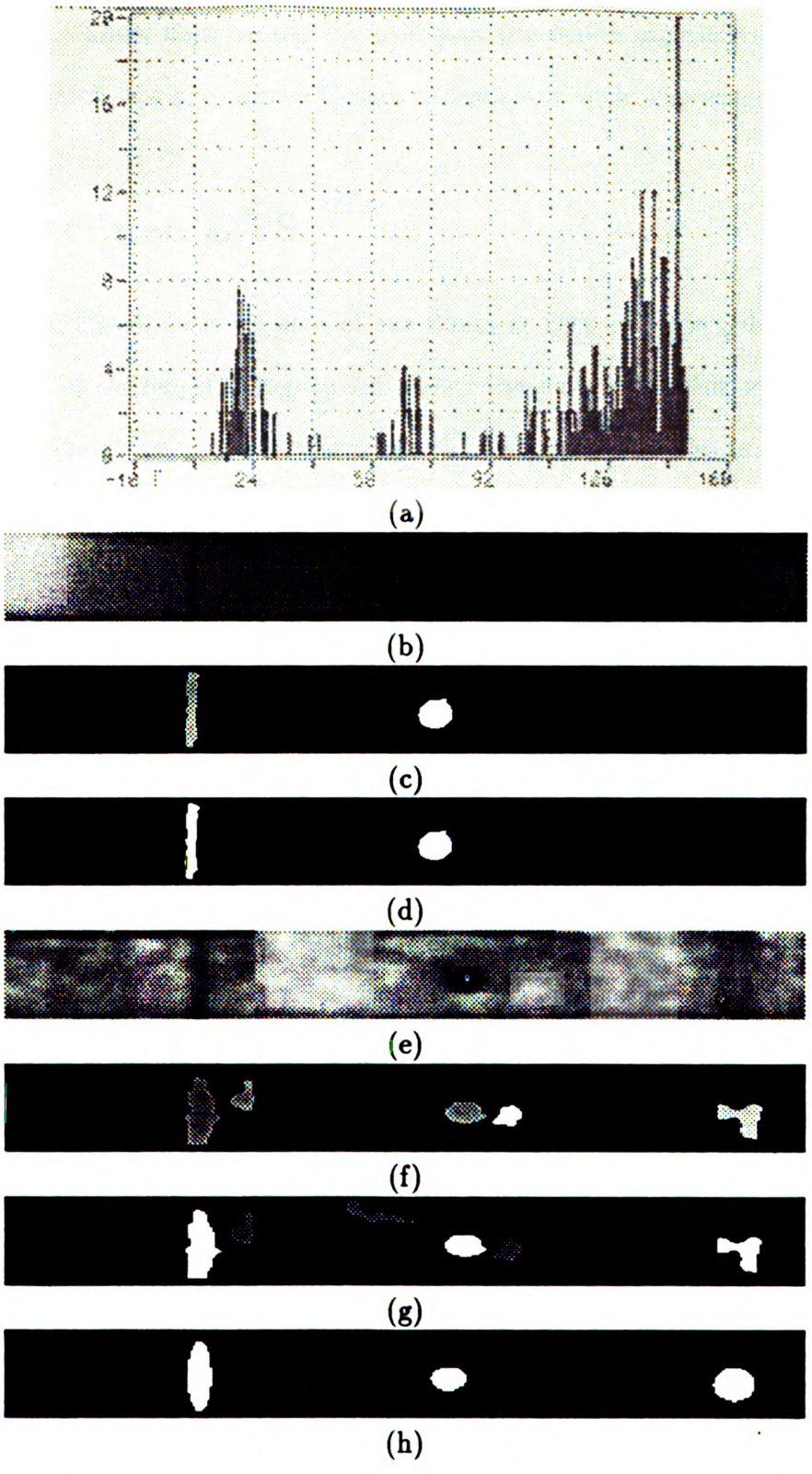

Figure 7.4: Defect map of specimen CTHS. (a) Acoustic emission graph. (b) X-ray image. (c) Segmented X-ray image. (d) Extracted defects in the X-ray image. (e) C-scan image. (f) Segmented C-scan image. (g) Extracted defects in the C-scan image. (g) Defect map of the specimen.

by the C-scan. Thus, here we see the utility of the fusion algorithm. It found the teflon insert which was only in the C-scan image along with 3 spurious components.

7.6 Specimen CTS

Specimen CTS contains an area of cut fibers at 25% of its length, and a teflon insert at 75% of its length. Figure 7.5 shows the results for this specimen. The acoustic emission graph presents two peaks. The segmented X-ray image contains 2 objects of which only one corresponds to a defect (the cut plies), and the segmented C-scan image contains 5 objects—2 defects and 3 spurious components.

In this case, the cut plies are found first and accepted with $\alpha = 0.95$. Then the algorithm tries to map the remaining object in the X-ray image and the object in the middle in the C-scan image. This is not accepted since $\alpha = 0.64$. Even if the two objects have about the same orientation, they are not at the same position at all and cannot be confirmed by a peak in the acoustic emission graph. Then, the leftmost object in the segmented C-scan image and the second peak in the acoustic emission graph are mapped into a defect since $\beta = 0.02$. Once again, an accurate defect map of the specimen is obtained. Even though the segmentation results are not perfect, the fusion algorithm extracts the defects from among the spurious components.

7.7 Specimen THS

Specimen THS contains two teflon inserts at 25% and 75% of its length and a hole in the middle. Figure 7.6 shows the results. The acoustic emission graph contains 3 peaks corresponding to the two teflon inserts and the hole. The segmented X-ray image contains 2 objects, one being the hole and the other being spurious, and the

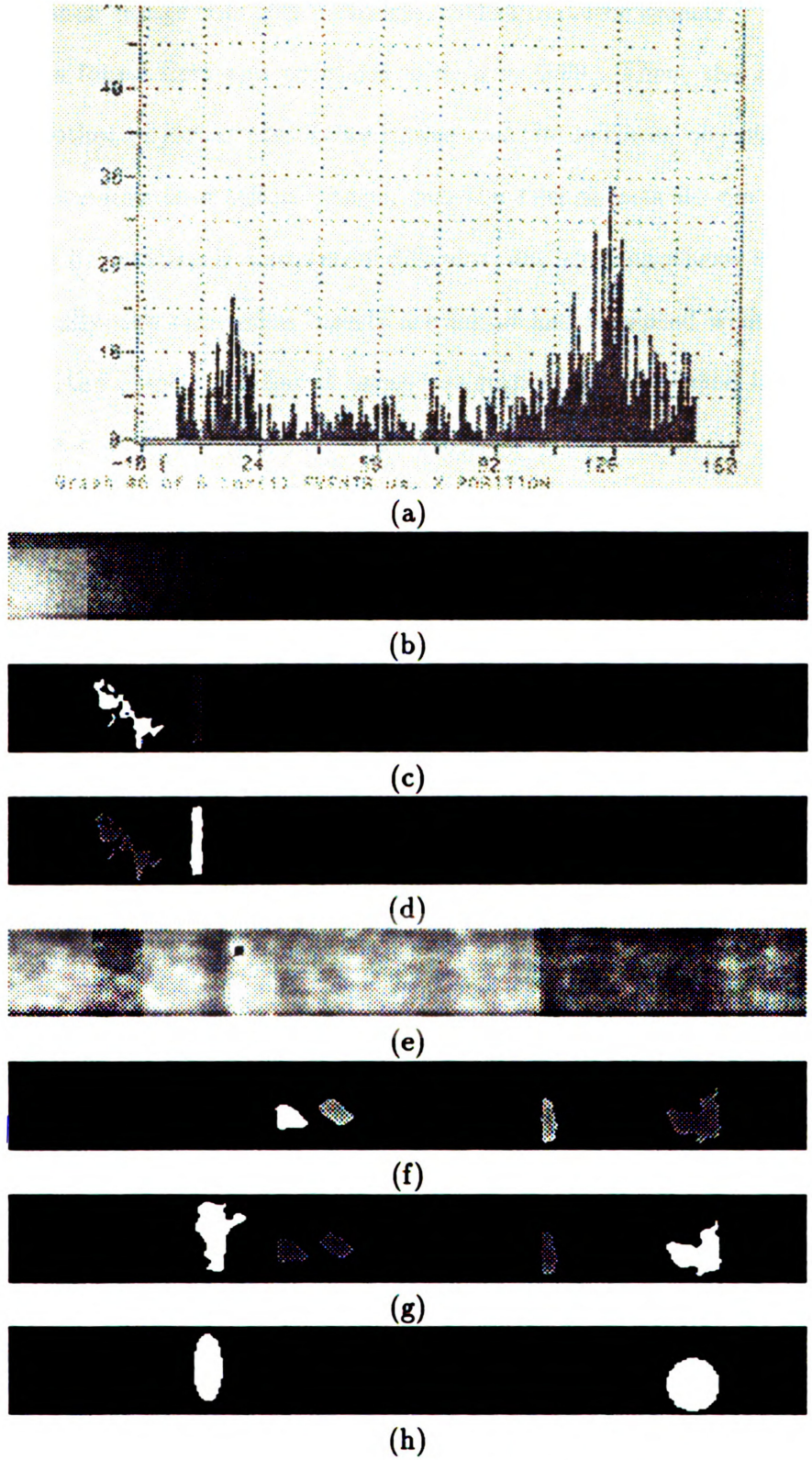

Figure 7.5: Defect map of specimen CTS. (a) Acoustic emission graph. (b) X-ray image. (c) Segmented X-ray image. (d) Extracted defects in the X-ray image. (e) C-scan image. (f) Segmented C-scan image. (g) Extracted defects in the C-scan image. (g) Defect map of the specimen.

segmented C-scan image contains 4 objects, including three defects.

The hole is found first and accepted with $\alpha = 0.99$. Then, the algorithm tries to match the other object in the X-ray image and the leftmost object in the C-scan image (corresponding to a teflon insert), but the two objects do not have much in common, their orientation is completely different, and the hypothesis is rejected with $\alpha = 0.71$. Finally, the two teflon inserts are found and accepted with $\beta = 0.00$ and $\beta = 0.03$. All the defects are found using two imperfect segmented images, and an accurate defect map of the specimen is obtained.

7.8 Specimen TS

Specimen TS contains 2 teflon inserts at 25% and 75% of its length. The segmentation and fusion results are shown in Figure 7.7. The acoustic emission graph presents 2 peaks. The segmentation of the X-ray image does not reveal anything, and no objects are found. The segmented C-scan image contains 8 objects.

For this specimen, the X-ray image is of no use. So, the algorithm has to find the defects by considering only the C-scan image and the acoustic emission graph. The two teflon inserts are found and accepted with $\beta = 0.00$ and $\beta = 0.16$. Thus, the fusion algorithm is very useful. It found the defects given a useless X-ray image which contained no defects, and a poor segmentation of the C-scan image containing 6 spurious components which did not correspond to any defects.

7.9 Summary

We have seen that the image segmentation method combined with the fusion algorithm can extract defects from the three pieces of information, and construct an

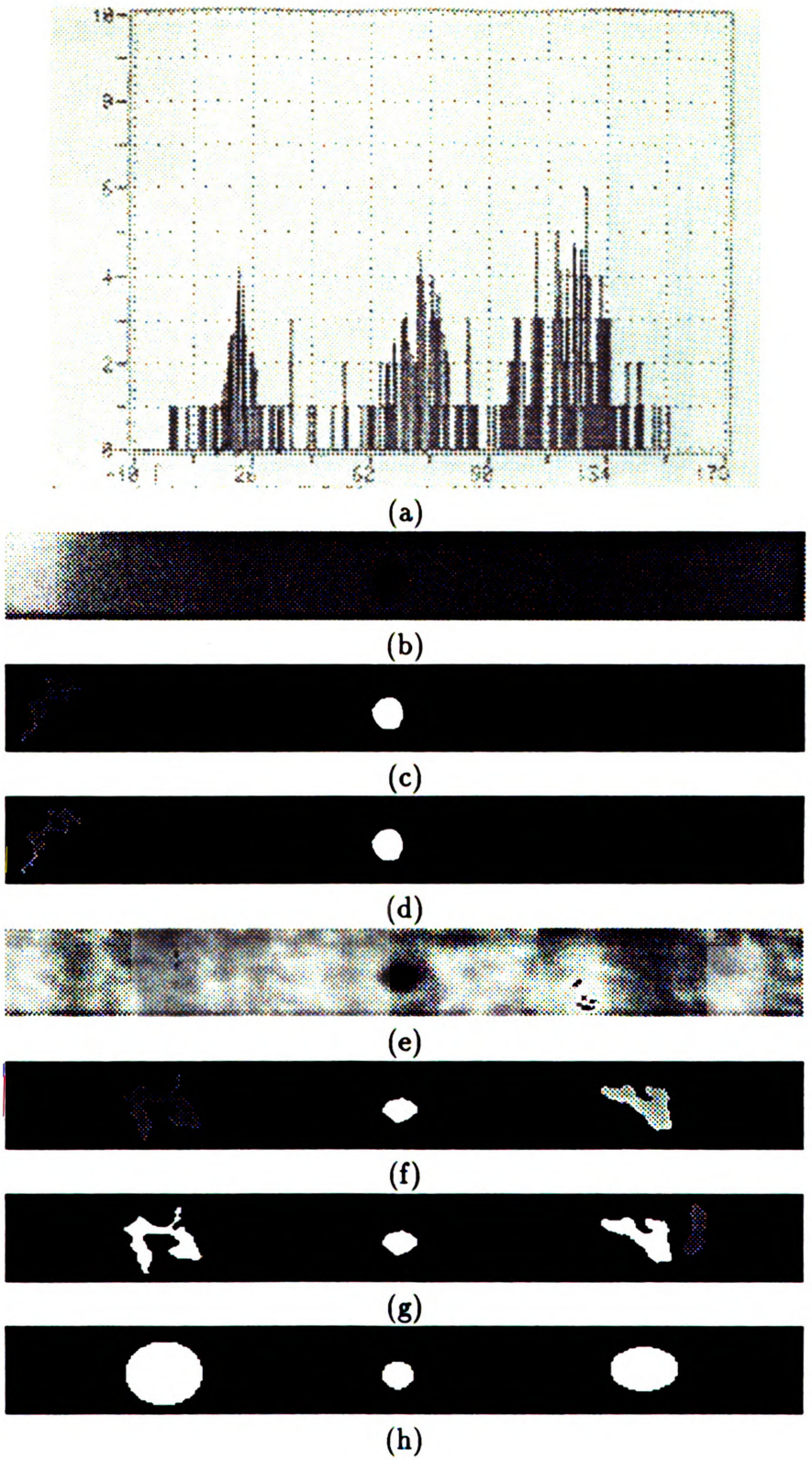

Figure 7.6: Defect map of specimen THS. (a) Acoustic emission graph. (b) X-ray image. (c) Segmented X-ray image. (d) Extracted defects in the X-ray image. (e) C-scan image. (f) Segmented C-scan image. (g) Extracted defects in the C-scan image. (g) Defect map of the specimen.

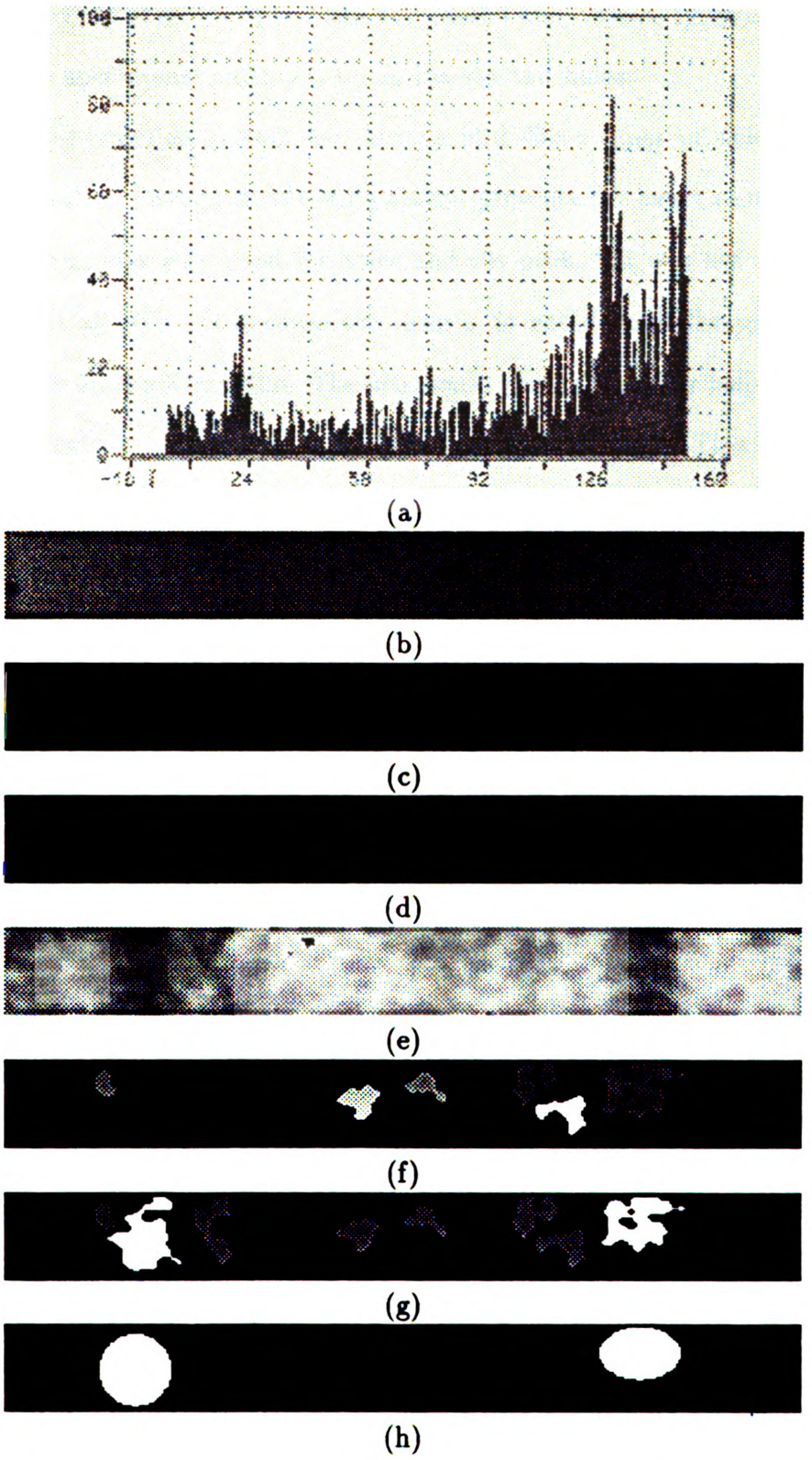

Figure 7.7: Defect map of specimen TS. (a) Acoustic emission graph. (b) X-ray image. (c) Segmented X-ray image. (d) Extracted defects in the X-ray image. (e) C-scan image. (f) Segmented C-scan image. (g) Extracted defects in the C-scan image. (g) Defect map of the specimen.

accurate defect map of all the specimens considered here. Three types of defects were included in the specimens: cut plies, teflon inserts and holes.

The acoustic emission system can always find these types of defects since the location distribution histogram of events always presents the exact number of peaks. The X-ray system was very good for holes and cut plies, but was not able to detect teflon inserts at all. This is because the inserts do not disturb the photons and so nothing appears on the X-ray film. The ultrasonic system was very helpful for finding the teflon inserts but was not very good in isolating the cut plies. This is because the teflon insert reflects the ultrasonic wave much better than the air in the cut plies.

Chapter 8

Conclusions

8.1 Conclusions and discussion

In this thesis, we have tried to solve the problem of nondestructive inspection of composite materials. We have seen that there are many available techniques for finding defects in composite materials. We have chosen to use three of them: X-radiography, ultrasonic C-scan, and acoustic emission. X-radiography and ultrasonic C-scan provided images that could be analyzed using image processing tools. Acoustic emission systems record "events" and display the location distribution histogram of events. Chapter 5 reported an image segmentation technique used to isolate objects from the background in the X-ray and C-scan images. The fusion process using the segmented X-ray and C-scan images and the acoustic emission graph was presented in Chapter 6. In these two chapters, some results were shown on specimens containing only one type of defect: cut plies. Chapter 7 studied the performance of the proposed fusion scheme on specimens containing three types of defects: cut plies, teflon inserts and holes.

We have seen that even if the acoustic emission technique always finds the defects,

it is not sufficient since it only gives the location of the defects along the length of the specimen. The X-ray image has high contrast most of the time, that is, the defects appear clearly in the image. But the large difference in illumination along the length of the image required a sophisticated image segmentation technique based on local neighborhood and edge detection. The Yanowitz and Bruckstein thresholding method used with the Canny edge detector solved the segmentation problem very well. Although the segmented X-ray image contained very few spurious connected components, and sometimes even presented an accurate map of the specimen, we have seen that this technique was not sufficient since X-radiography could not detect the teflon inserts due to poor distortion of the incoming photons' trajectory. The C-scan images are very noisy and the segmentation method often produces as many components corresponding to spurious components as to defects. Therefore, the C-scan technique is not sufficient since a lot of extra components are extracted during the segmentation process. We have also seen that, sometimes, ultrasonic C-scan could not detect cut plies due to imperfect refraction of the ultrasonic wave by the air inside the specimen.

Thus, none of the three NDI techniques studied here is sufficient to detect all the defects that had been artificially inserted into the specimens. X-radiography performs very well in detecting cut plies and holes, while ultrasonic C-scan is better for teflon inserts. The combination of the two segmented images and the acoustic emission graph by the fusion algorithm makes it possible to obtain an accurate defect map of the specimen in all the cases. The fusion algorithm has the advantage of being very simple; it matches connected components in the segmented X-ray and C-scan images based on geometric properties and verifies the location of the defects using the peaks in acoustic emission graph. The fusion algorithm can find the defects from imperfect X-radiography which does not reveal some of the defects, and an imperfect

segmentation of the C-scan image which reveals too many objects.

The NDI scheme that we have followed is not the one that the aerospace industry would apply since, for example, it is not possible to X-ray or C-scan an entire airplane wing. But we have shown that it is feasible to (i) subject the composite structure to a load and record the acoustic emission signals; and (ii) analyze the acoustic emission graph to detect the peaks that correspond to the defects. Then one can X-ray and C-scan and optionally even use additional techniques to obtain images of the portions of the structure which emitted more events than the others.

8.2 Future research

In this research we have only studied macroscopic defects such as delaminations (simulated by the cut plies), inserts, or holes. This is because neither the X-radiography machine nor the ultrasonic apparatus available to us was adequate to extract really small defects like cut fibers or matrix cracks. It would be interesting to see if the segmentation and fusion methods still work for microscopic defects by studying images of such defects and applying the segmentation and fusion algorithm to extract defects.

It would also be a good idea to try the same method on different materials. Our specimens were made of glass fibers and polyester resin. How about carbon fibers or epoxy resin? There is no reason why the method should not work or the defects should not be detected, but a topic of future research would be to try the method on different kinds of composite structures.

In our experiments we are able to construct a defect map of the specimen, i.e., for each defect, we know its location and its area. But, we do not know the nature of the defect, or whether it is a critical defect. Although we have seen that X-radiography

does not find teflon inserts, we cannot conclude that if the defect appears only in the C-scan image and in the acoustic emission graph, then it is a teflon insert. It is dangerous to draw such conclusions without more proof since something might have happened during the X-radiography that disabled the detection of another type of defect. Some authors [Lee90] suggest that there is a relationship between the amplitude of the event and the nature of the defect. It would be interesting to analyze other graphs produced by the acoustic emission system and draw conclusions regarding the nature of the defects from graphs such as the amplitude vs. position graph or the amplitude vs. time graph, and maybe the gray levels of the objects in the X-ray and C-scan images. Once the location, area, and nature of the defects are known, it might be possible to get information about the severity of the defects.

Appendix A

Curve fitting

A.1 Introduction

Given a set of observations, one might want to condense the data by fitting a parametric model to it. Modeling can also be used as a kind of constrained interpolation, where one wants to extend a few data points into a continuous function, but with some underlying idea of what that function would look like. This is typically the problem that we want to solve by fitting a mixture of two Gaussian densities to the histogram of the image in Section 5.3.1. Solutions to this problem are presented in most numerical analysis books and particularly in Chapter 14 of [PFTV88], but some brief explanations will be given in this Appendix.

Suppose that we are fitting a model with M adjustable parameters a_j, $j = 1, \ldots, M$ to N data points (x_i, y_i), $i = 1, \ldots, N$. The model then has the following mathematical expression:

$$y(x) = y(x; a_1, \ldots, a_M). \tag{A.1}$$

The usual way of solving this problem is to minimize the distance between the

data and the model; that is, to minimize over $a_1, \ldots, a_M$ the following quantity:

$$\sum_{i=1}^{N} [y_i - y(x_i; a_1, \ldots, a_M)]^2. \tag{A.2}$$

We can differentiate this expression with respect to each of the parameters and, at the minimum value, this derivative should be zero. We then obtain a system of M equations with M unknowns which can be solved using any method for solving a system of linear or nonlinear equations.

$$\sum_{i=1}^{N} (y_i - y(x_i)) \frac{\partial y(x_i; a_1, \ldots, a_M)}{\partial a_k}, \quad \forall k = 1, \ldots, M. \tag{A.3}$$

A.2 Fitting data to a straight line

As a simple example, we first consider fitting a straight line to a set of N data points. The expression of the straight line is:

$$y(x) = y(x; a, b) = a + bx. \tag{A.4}$$

Then, we want to minimize:

$$L(a, b) = \sum_{i=1}^{N} (y_i - a - bx_i)^2. \tag{A.5}$$

This is done by differentiating $L(a, b)$ with respect to a and b, setting these expressions equal to zero and solving for a and b.

$$\frac{\partial L(a, b)}{\partial a} = -2 \sum_{i=1}^{N} (y_i - a - bx_i) = 0, \tag{A.6}$$

$$\frac{\partial L(a,b)}{\partial b} = -2\sum_{i=1}^{N} x_i(y_i - a - bx_i) = 0. \tag{A.7}$$

This is a linear system of two equations and two unknowns which can easily be solved.

$$a = \frac{S_{xx}S_y - S_x S_{xy}}{NS_{xx} - S_{xx}^2}, \tag{A.8}$$

$$b = \frac{NS_{xy} - S_x S_y}{NS_{xx} - S_{xx}^2}, \tag{A.9}$$

where:

$$S_x = \sum_{i=1}^{N} x_i, \quad S_y = \sum_{i=1}^{N} y_i, \quad , S_{xx} = \sum_{i=1}^{N} x_i^2, \quad S_{xy} = \sum_{i=1}^{N} x_i y_i. \tag{A.10}$$

A.3 Nonlinear models

We now consider a fitting problem when the model depends nonlinearly on the set of M unknown parameters a_k, $k = 1, \ldots, M$. We use the same approach as before, i.e., we define a merit function and determine best-fitting parameters by minimizing the function. With nonlinear functions, however, the minimization must proceed iteratively. We assume that near the minimum value, the merit function can be approximated by the following quadratic form:

$$L(\mathbf{a}) \approx \gamma - \mathbf{d} \cdot \mathbf{a} + \frac{1}{2}\mathbf{a} \cdot \mathbf{D} \cdot \mathbf{a}. \tag{A.11}$$

where $\mathbf{d}$ is an M-vector, $\mathbf{D}$ is an $M \times M$ matrix, and $\mathbf{a}$ is the vector of parameters. If the approximation is a good one, we know how to update the current trial parameters $\mathbf{a}_{cur}$ to the desired parameters $\mathbf{a}_{min}$ in a single step, by:

$$\mathbf{a}_{min} = \mathbf{a}_{cur} + \mathbf{D}^{-1} \cdot [-\nabla L(\mathbf{a}_{cur})]. \tag{A.12}$$

On the other hand, if the approximation is poor, then we use the steepest descent method:

$$\mathbf{a}_{next} = \mathbf{a}_{cur} - \text{constant} \times \nabla L(\mathbf{a}_{cur}). \tag{A.13}$$

To use the formula in (A.13), we must be able to compute the gradient of the merit function at any set of parameters **a**. We also need the matrix **D**, which involves the second derivatives of the merit function.

The first derivatives of the merit function are:

$$\frac{\partial L(\mathbf{a})}{\partial a_k} = -2\sum_{i=1}^{N}(y_i - y(x_i;\mathbf{a}))\frac{\partial y(x_i;\mathbf{a})}{\partial a_k}, \quad \forall k = 1,\ldots,M. \tag{A.14}$$

Taking an additional partial derivative and considering only the first order terms gives:

$$\frac{\partial^2 L}{\partial a_k a_l} = 2\sum_{i=1}^{N}\frac{\partial y(x_i;\mathbf{a})}{\partial a_k}\frac{\partial y(x_i;\mathbf{a})}{\partial a_l}. \tag{A.15}$$

Equation (A.12) can be rewritten as:

$$\sum_{i=1}^{N}\alpha_{kl}\delta a_l = \beta_k \text{ with } \alpha_{kl} = \frac{1}{2}\frac{\partial^2 L}{\partial a_k a_l} \text{ and } \beta_k = \frac{1}{2}\frac{\partial L(\mathbf{a})}{\partial a_k}. \tag{A.16}$$

And Equation (A.13) translates to:

$$\delta a_l = \text{constant} \times \beta_l. \tag{A.17}$$

A.4 Levenberg-Marquardt method

Marquardt proposed an elegant method, related to an earlier suggestion of Levenberg, for shifting smoothly between the extremes of the inverse Hessian method (A.12) and the steepest descent method (A.13). The latter is used when we are far

from the minimum, switching smoothly to the former as the minimum is approached. Replace Equation (A.13) by

$$\delta a_l = \frac{1}{\lambda \alpha_{ll}} \beta_l. \tag{A.18}$$

Then,

$$\alpha'_{jj} = \alpha_{jj}(1 + \lambda) \text{ and } \alpha'_{jk} = \alpha_{jk} \text{ if } k \neq j, \tag{A.19}$$

and, the linear system of equations becomes:

$$\sum_{i=1}^{M} \alpha'_{kl} \delta a_l = \beta_k. \tag{A.20}$$

The model fitting algorithm based on the above scheme is as follows:

- Choose arbitrarily an initial value for **a**
- Compute $L(\mathbf{a})$
- Pick a modest value for λ, say $\lambda = 0.001$
- (†) Solve for $\delta\mathbf{a}$ in the linear system of equations (A.20) and evaluate $L(\mathbf{a}+\delta\mathbf{a})$
- If $L(\mathbf{a} + \delta\mathbf{a}) \geq L(\mathbf{a})$, then increase λ by a factor of 10 and go back to (†), do not update the value of **a**
- If $L(\mathbf{a}+\delta\mathbf{a}) < L(\mathbf{a})$, then decrease λ by a factor of 10, update the trial solution $\mathbf{a} \leftarrow \mathbf{a} + \delta\mathbf{a}$, and go back to (†)
- Stop when L decreases by a negligible amount, say less than 0.1

A.5 Fitting a mixture of Gaussian densities to the image histogram

When we want to fit a mixture of Gaussian densities to the histogram of an image, we have 256 data values (one for each gray level value), and the function $y(x)$ has the form:

$$y(x) = A_o \exp\left\{-\frac{(x-\mu_o)^2}{2\sigma_o^2}\right\} + A_b \exp\left\{-\frac{(x-\mu_b)^2}{2\sigma_b^2}\right\}, \tag{A.21}$$

where x is the gray value, $y(x)$ is the number of pixels with gray level x, μ_o (μ_b), σ_o^2 (σ_b^2) are the mean and the variance of the object (background) pixels, and A_o and A_b are the mixing parameters.

We thus have 6 unknown parameters: A_o, μ_o, σ_o, A_b, μ_b, σ_b. The merit function is:

$$L(\mathbf{a}) = \sum_{i=1}^{256} \left(y_i - A_o \exp\left\{-\frac{(x_i-\mu_o)^2}{2\sigma_o^2}\right\} + A_b \exp\left\{-\frac{(x_i-\mu_b)^2}{2\sigma_b^2}\right\} \right)^2. \tag{A.22}$$

We can easily compute the derivative of the merit function with respect to each of the parameters as follows.

$$\frac{\partial y(x;\mathbf{a})}{\partial A_o} = \exp\left\{-\frac{(x-\mu_o)^2}{2\sigma_o^2}\right\}, \tag{A.23}$$

$$\frac{\partial y(x;\mathbf{a})}{\partial A_b} = \exp\left\{-\frac{(x-\mu_b)^2}{2\sigma_b^2}\right\}, \tag{A.24}$$

$$\frac{\partial y(x;\mathbf{a})}{\partial \mu_o} = A_o \exp\left\{-\frac{(x-\mu_o)^2}{2\sigma_o^2}\right\} \left(\frac{x-\mu_o}{\sigma_o}\right), \tag{A.25}$$

$$\frac{\partial y(x;\mathbf{a})}{\partial \mu_b} = A_b \exp\left\{-\frac{(x-\mu_b)^2}{2\sigma_b^2}\right\} \left(\frac{x-\mu_b}{\sigma_b}\right), \tag{A.26}$$

$$\frac{\partial y(x;\mathbf{a})}{\partial \sigma_o} = A_o \exp\left\{-\frac{(x-\mu_o)^2}{2\sigma_o^2}\right\}\left(\frac{(x-\mu_o)^2}{\sigma_o^3}\right), \tag{A.27}$$

$$\frac{\partial y(x;\mathbf{a})}{\partial \sigma_b} = A_b \exp\left\{-\frac{(x-\mu_b)^2}{2\sigma_b^2}\right\}\left(\frac{(x-\mu_b)^2}{\sigma_b^3}\right). \tag{A.28}$$

These derivatives are used to compute the merit function and solve for **a**. An initial value for **a** is chosen by computing the mean and standard deviation of the histogram corresponding to the low gray levels (object) and the mean and standard deviation of the histogram corresponding to the high gray levels (background).

Bibliography

[AGM85] J. Awerbuch, M. R. Gorman, and M. Madhukar. Monitoring Acoustic Emission during Quasi-static Loading-Unloading Cycles of Filament-wound Graphite-Epoxy Laminate Coupons. *Materials Evaluation*, (43):754–765, May 1985.

[AMG84] J. Awerbuch, M. Madhukar, and M. R. Gorman. Monitoring Damage Accumulation in Filament-Wound Graphite/Epoxy Laminate Coupons During Fatigue Loading Through Acoustic Emission. *Journal of Reinforced Plastics and Composites*, 3:2–39, January 1984.

[BB82] D. H. Ballard and C. M. Brown. *Computer Vision.* Prentice-Hall, Englewood Cliffs, NJ, 1982.

[Bes86] J. Besag. On the Statistical Analysis of Dirty Pictures. *Journal of the Royal Statistical Society*, 48(3):259–302, 1986.

[BS89] D. E. Bray and R. K. Stanley. *Nondestructive Evaluation, A Tool for Design, Manufacturing, and Service.* McGraw-Hill, 1989.

[Can86] J. Canny. A Computational Approach to Edge Detection. *IEEE Transactions on Pattern Analysis and Machine Intelligence*, 8(6):679–698, November 1986.

[CK72] C. K. Chow and T. Kaneko. Automatic Boundary Detection of the Left Ventricle from Cineangiograms. *Computers and Biomedical Research*, 5:388–410, 1972.

[CY90] J. Clark and A. Yuille. *Data Fusion and Sensory Information Processing Systems.* Kluwer, Boston, MA, 1990.

[DJNC90] R. C. Dubes, A. K. Jain, S. G. Nadabar, and C. C. Chen. MRF Model-Based Algorithms for Image Segmentation. In *Proceedings of the 10th International Conference on Pattern Recognition*, pages 808–814, Atlantic City, New Jersey, June 1990.

[FM81] K. S. Fu and J. K. Mui. A Survey on Image Segmentation. *Pattern Recognition*, 13:3–16, 1981.

[HP74] S. L. Horowitz and T. Pavlidis. Picture Segmentation by a Directed Split-and-Merge Procedure. In *Proceedings of the 2nd International Conference on Pattern Recognition*, pages 424–433, August 1974.

[HS85] R. M. Haralick and L. G. Shapiro. Image Segmentation Techniques. *Computer Vision, Graphics and Image Processing*, 29:100–132, 1985.

[Hul81] D. Hull. *An Introduction to Composite Materials.* Cambridge University Press, 1981.

[LCS84] M. S. Landy, Y. Cohen, and G. Sperling. HIPS: A Unix-Based Image Processing System. *Computer Vision, Graphics, and Image Processing*, (25):331–347, 1984.

[Lee90] W. M. Lee. Damage Assessment in Graphite Fiber/Polymer Composites Using Acoustic Emission and Ultrasonic Techniques. In *Proceedings of the*

5th Technical Conference of the American Society for Composites, pages 955–967, June 1990.

[MA86] M. Madhukar and J. Awerbuch. Monitoring Damage Progression in Center-Notched Boron/Aluminum Laminates Through Acoustic Emission. *ASTM STP*, (893):337–367, 1986.

[Mil89] G. Miles. Cheers for Reinforced Plastics. *Lansing State Journal*, page 4B, may 5th 1989.

[MKCP87] X. Maldague, J. C. Krapez, P. Cielo, and D. Poussart. Processing of Thermal Images for the Detection and Enhancement of Subsurface Flaws in Composite Materials. In C.H. Chen, editor, *Signal Processing and Pattern Recognition in Nondestructive Evaluation of Materials*, pages 257–285. NATO ASI Series, Springer-Verlag, 1987. Series F.

[MM71] R. L. Mehan and J. V. Mullin. Analysis of Composite Failure Mechanism Using Acoustic Emissions. *Journal of Composite Materials*, 5:26–269, April 1971.

[NR79] Y. Nakagawa and A. Rosenfeld. Some Experiments in Variable Thresholding. *Pattern Recognition*, 11:191–204, 1979.

[PFTV88] W. H. Press, B. P. Flannery, S. A. Teukolsky, and W. T. Vetterling. *Numerical Recipes in C, The Art of Scientific Computing.* Cambridge University Press, 1988.

[PR78] D. P. Panda and A. Rosenfeld. Image Segmentation by Pixel Classification in (Gray Level, Edge Value) Space. *IEEE Transactions on Computers*, 27(9):875–879, September 1978.

[Pur83] D. Purslow. Fractographic Analysis of Failures in CFRP. In *Characterization, Analysis and Significance of Defects in Composite Materials, AGARD Conference Proceedings no 355*, pages 1–11. NATO, 1983.

[Rei80] K. L. Reifsnider. *Damage in Composite Materials.* ASTM STP 775, 1980.

[RK82] A. Rosenfeld and A. C. Kak. *Digital Picture Processing.* Academic Press, Inc., San Diego, CA, 1982.

[Ros78] A. Rosenfeld. Iterative Methods in Image Analysis. *Pattern Recognition*, 10:181–187, 1978.

[RR80] S. Ranade and A. Rosenfeld. Point Pattern Matching by Relaxation. *Pattern Recognition*, 12:269–275, 1980.

[SC83] D. E. W. Stone and B. Clarke. In service NDI of Composite Structures: An Assessment of Current Requirements and Capabilities. In *Characterization, Analysis and Significance of Defects in Composite Materials, AGARD Conference Proceedings no 355*, pages 230–237. NATO, 1983.

[Sen83] G. P. Sendeckyj. NDE Techniques for Composite Laminates. In *Characterization, Analysis and Significance of Defects in Composite Materials, AGARD Conference Proceedings no 355*, pages 12–33. NATO, 1983.

[SKB82] G. Stockman, S. Kopstein, and S. Benett. Matching Images to Models for Registration and Object Detection via Clustering. *IEEE Transactions on Pattern Analysis and Machine Intelligence*, 4(3):229–241, May 1982.

[SSW88] P. K. Sahoo, S. Soltani, and A. K. C. Wong. A Survey of Thresholding Techniques. *Computer Vision, Graphics, and Image Processing*, 41:233–260, 1988.

[TJ89] J. Ton and A. K. Jain. Registering Landsat Images by Point Matching. *IEEE Transactions on Geoscience and Remote Sensing*, 27(5):642–651, September 1989.

[WNR78] J. S. Weszka, R. N. Nagel, and A. Rosenfeld. A Threshold Selection Technique. *IEEE Transactions on Systems, Man, and Cybernetics*, 8:622–629, 1978.

[WSYR83] C. Wang, H. Sun, S. Yada, and A. Rosenfeld. Some Experiments in Relaxation Image Matching Using Corner Features. *Pattern Recognition*, 16:167–182, 1983.

[YB89] S. D. Yanowitz and A. M. Bruckstein. A New Method for Image Segmentation. *Computer Vision, Graphics and Image Processing*, 46:82–95, April 1989.